Relevance of Crumbs homolog 2 in the Glomerular filtration barrier

Dissertation

zur

Erlangung des Doktorgrades (Dr. rer. nat.)

der

Mathematisch-Naturwissenschaftlichen Fakultät

der

Rheinischen Friedrich-Wilhelms-Universität Bonn

vorgelegt von

Rohan Bhatia

aus

New Delhi, India

Bonn, August 2024

Angefertigt mit Genehmigung der Mathematisch-Naturwissenschaftlichen Fakultät der Rheinischen Friedrich-Wilhelms-Universität Bonn

Gutachter/Betreuer: Prof. Dr. Ulrich Kubitscheck[i]

Gutachter: Prof. Dr. Rudolf Merkel[ii]

i: Clausius-Institut für Physikalische und Theoretische Chemie, Mathematisch-Naturwissenschaftliche Fakultät, Rheinischen Friedrich-Wilhelms-Universität Bonn

ii: Institute of Biological Information Processing, Forschungszentrum Jülich GmbH and Clausius-Institut für Physikalische und Theoretische Chemie, Mathematisch-Naturwissenschaftliche Fakultät, Rheinischen Friedrich-Wilhelms-Universität Bonn

Tag der Promotion: 17th October, 2024

Erscheinungsjahr: 2024

CONTENTS

Abstract

Mammalian podocytes not only form the final layer within the glomerular filtration barrier (GFB) but also withstand enormous pressure that essentially drives renal ultrafiltration. Their effacement has been linked with and usually marks the onset for several glomerular diseases. As is evident from their role, expression of polarity determinants during the early stages of kidney development help determine podocyte morphogenesis. This eventually helps to regulate inter– and intra-cellular transport processes and establish essential cell-cell communications required for efficient barrier formation. The Crumbs complex including the name-giving single-pass transmembrane protein Crumbs (CRB) is an evolutionarily conserved polarity determinant that help establish apico-basal polarity within many epithelia.

In this study, I investigated the role of two mammalian CRB orthologues, namely CRB2 and CRB3A with greater emphasis on the localization and functioning mechanism of CRB2. Utilizing the newly introduced method of expansion microscopy, we were able to identify the localization of CRB2 within the slit diaphragm (SD) of murine glomerulus and compare it with other known SD markers. Our discovery of CRB2 forming homotypic clusters led us to further investigate the role of its extra-long extracellular domain (ECD) within immortalized human kidney podocytes. Employing a multitude of advanced microscopic tools I was then able to further elucidate the mode of action of CRB2s ECD. Results from fluorescence recovery after photobleaching (FRAP) experiments demonstrated a slower mobility for CRB2 at podocyte-podocyte contact sites when compared with CRB3A. Additionally, a peculiar mobility pattern was observed for the ECD-specific CRB2 mutants, with the mutant lacking the entire ECD being particularly immobile. Data obtained using traction force microscopy revealed that CRB2 interacts in *trans*. However, these interactions are dynamic with CRB2 basically acting as the podocytes' environment sensor as evident from our live-cell imaging data. Upon contact with other CRB2-expressing cells, there is a massive re-organization of focal adhesion (FA) sites and actin cytoskeleton which ultimately governs cellular mobility and adhesion. A similar cytoskeletal effect could also be observed with CRB3A but to a much lesser extent. The findings from this study, provide for a basic understanding for the role of CRB2s ECD within the early embryonic stages of kidney development. The results presented here could be used as a guide for further research into podocyte cytology and/or development of therapeutics governing podocyte related glomerular diseases.

1. Introduction

The human kidney is not only an essential component of the urinary system but also a marvel of biological engineering. This pair of bean-shaped organs (Figure 1a) helps orchestrate the filtration of metabolic waste from blood and serves a pivotal role in maintaining the electrolyte balance of the body [1]. Additionally, it also helps to maintain blood pressure [2] via promotion of erythrocyte development [3], aids in the production of several essential hormones [1] and indirectly contributes towards bone development by synthesizing the active form of Vitamin D [4,5]. Owing to its highly vascularized structure, the kidneys can filter blood volumes equivalent to ~20% of total cardiac output [6,7]. Fluid homeostasis and osmoregulation via urine formation following blood ultrafiltration therefore, remains its predominant function. During this process, water and low-molecular-weight substances such as urea are excreted whereas high-molecular-weight substances such as albumin and blood cells are retained [1].

Looking closely at its structure, it can be seen to primarily consist of three major regions called the renal cortex, renal medulla and the renal pelvis [8]. As shown in Figure 1b, the renal cortex builds the outer region whereas the renal medulla forms the inside within the functional space of the kidney. These two regions are ideally organized into eight to eighteen cone-shaped structures called the renal pyramids. The tip of each of these pyramids empties urine into individual minor calyces. Urine from multiple minor calyces then flows into a major calyx that ultimately drains into the renal pelvis for excretion. Within each renal pyramid, urine production occurs inside numerous nephrons (Figure 1c), also called the basic functional unit of the kidney. On average, each human kidney harbors approximately ~1-2.5 million nephrons that work in tandem [9].

Delving into the structure of the nephron, two functional units, namely, the filtration unit also called as the renal corpuscle and the tubular resorption compartment called the renal tubule can be segregated [1,8]. The renal corpuscle encloses a tuft of capillaries also known as the glomerulus within a cup-shaped Bowman’s capsule. As shown in Figure 1d (glomerulus zoom-in), each glomerulus further comprises of four major cell types, namely, the arteriole adjacent mesangial cells (MCs), inner tuft forming glomerular endothelial cells (GECs), the polarized perivascular podocytes and parietal epithelial cells (PECs). Afferent and efferent arterioles help carry blood to and from the Bowmans capsule. After filtration through the Bowmans capsule (Figure 1d), primary

urine ultimately drains out through a series of inter-connected tubules starting with the proximal tubule (PT), the loop of Henle (LOH), the distal convoluted tubule (DT) and finally the collecting duct (CD). During this tubular transport, reabsorption of essential nutrients such as glucose and other amino acids along with water takes place. Simultaneously, this primary urinary filtrate gets concentrated with waste products such as urea, creatinine and uric acid [8]. Filtered and concentrated fluid from multiple nephrons' DTs reaches the collecting duct that ultimately gets stored in the urinary bladder before getting excreted from the body. On average, after water reabsorption and concentration, an adult human excretes a daily total of ~1-1.5 L of urine. However, knowing that the volume of blood passing through both kidneys at any given time point represents ~20% of total cardiac output [6,7]; the glomerular filtration rate (GFR) could then be defined as the total amount of primary urine per time interval getting filtered. The average GFR for healthy adults, therefore, was found to vary with age. Typically, it ranges between either ~60 ml per min per 1.73 m^2 of body surface area for individuals >65 years of age to ~125 ml/min/1.73 m^2 for individuals <40 years of age [8,10–13]. These GFR volumes equate to a massive daily amount ~150-250 L of primary urine being filtered out from both kidneys. This in turn, therefore, highlights the importance of the nephrons' anatomically intricate sieve known as the glomerular filtration barrier (GFB) that enables the stable functioning of such a high-throughput and selective filtration process.

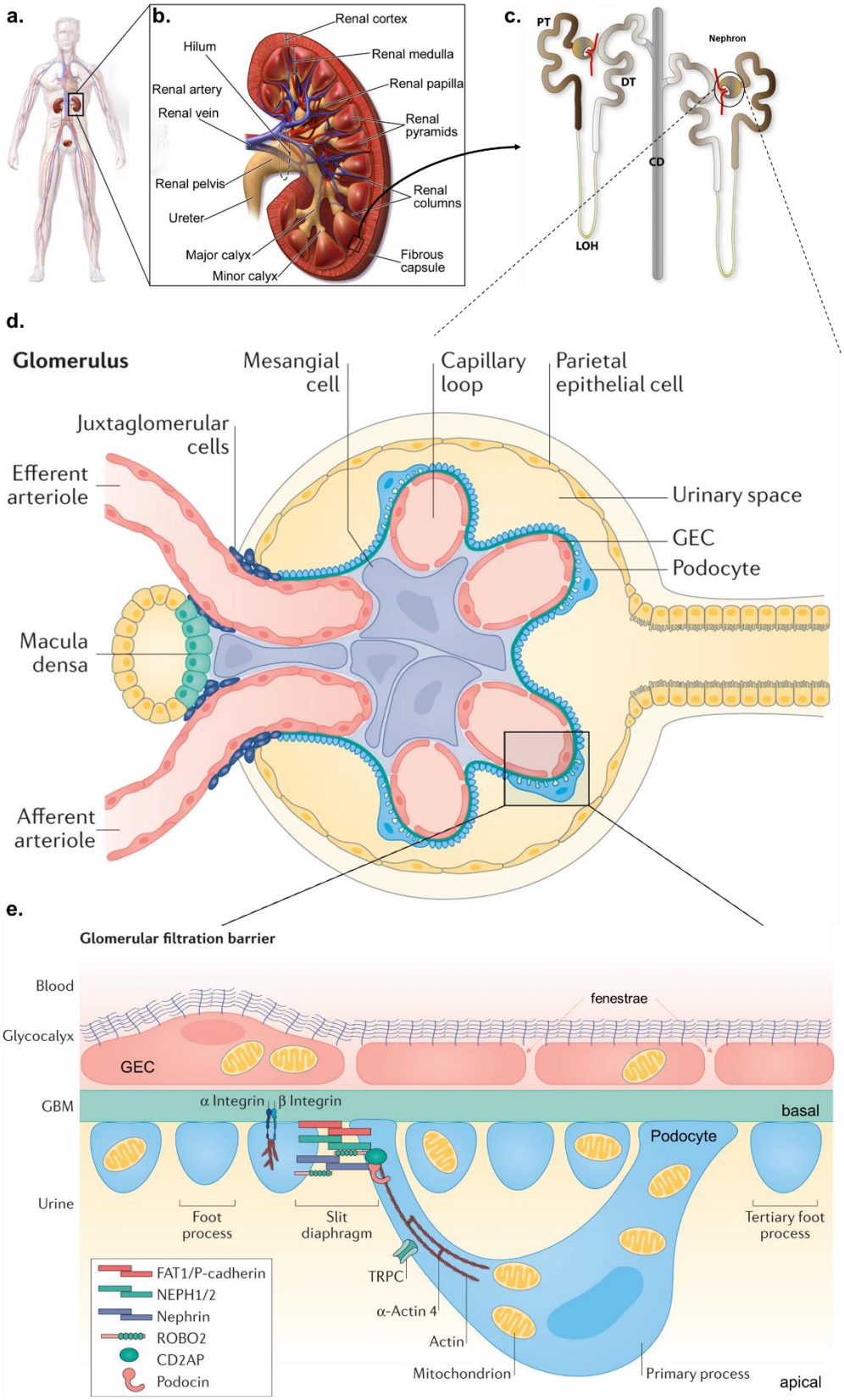

Figure 1: Human kidney anatomy.
(a) Graphic representation of the location of the kidneys within the human body. **(b)** Zoomed-in view of the human kidney showing the renal cortex, medulla and renal pelvis. **(c)** Zoomed-in view of the renal cortex and medulla showcasing the position of two nephrons draining into the CD. **(d)** Zoomed-in view of the glomerulus from one of the nephrons shown in **(c)**. **(e)** Zoomed-in view of the GFB within each glomeruli demonstrating the three distinct filtration layers. CD: collecting duct; DT: distal convoluted tubule; GBM: glomerular basement membrane; GEC: glomerular endothelial cells; GFB: Glomerular filtration barrier; LOH: loop of Henle; PT: proximal tubule; ROBO2: roundabout homologue 2 and TRPC: transient receptor potential-like channel. Modified from [1,14–17].

1.1. The glomerular filtration barrier

Located within the renal corpuscle of each individual nephron, the GFB forms a rigorous barrier that filters the majority of blood plasma proteins to retain essential nutrients and secrete protein-free urine [18]. As shown in Figure 1e, the endothelial GECs and the perivascular podocytes along with their secreted extracellular matrix (ECM) known as the glomerular basement membrane (GBM) form the three distinct filtration layers of the GFB [1,19–22].

Blood plasma filtration through the GFB occurs based upon molecular size as well as the electrical charge of individual components [23,24]. As a result, water and small solutes freely move across the GFB whereas high-molecular-weight substances and cells are retained. In addition to this, filtration through the GFB also relies upon the hydrostatic pressure within the glomerular tuft capillaries which is estimated to be approximately 45 millimeters of mercury (mmHg)/0.06 bar. Opposing osmotic pressure being exerted from plasma colloids and the hydrostatic pressure from fluids already present within the Bowman's capsule help to reduce the net filtration pressure down to approximately 15 mmHg/0.02 bar [10]. Therefore, along with its selective permeability, the GFB is also able to withstand immense pressure changes; features that can be attributed solely to its intricate structure.

1.1.1. Glomerular endothelium as the first barrier to renal ultrafiltration

During the early stages of development, reposition of migratory embryonic blood cells or angioblasts within the glomerular tuft capillaries is initiated from nascent podocytes by the secretion of the Vascular Endothelial Growth Factor A (VEGFA). Mature angioblasts express specific receptors, namely, VEGFR1 (Flt1), VEGFR2 (Flt1/Kdr) and neuropilin-1 [1,25] that get bound by VEGFA. Alternatively, a condition known as endotheliosis can be observed demonstrating a progressive loss in endothelium upon ablation of either *Vegfa* from podocytes and/or its receptors [26–28]. Any damage inflicted upon the glomerulus in this manner, inevitably results in proteinuria; a condition defined as the occurrence of increased protein content within urine. Chemo-attraction resulting from the secretion of VEGFA, therefore, enables the establishment of the glomerular endothelium. This makes the fenestrated blood capillaries branching from afferent arterioles as the first filtration layer within the highly specialized GFB with

the migratory angioblasts finally maturing into GECs (Figure 1e). Within these capillaries, ~20% of the underlying surface area comprises of 60-100 nm wide pores/fenestrae that allow for rapid fluid exchange [29]. A fibrous matrix of negatively charged glycoproteins called the glycocalyx additionally coats the inner side of GECs to impart charge selectivity [30,31]. The net negative charge along with plasma component adsorption within the dense glycocalyx eventually forms a surface layer thicker than 200 nm. This layer further helps to narrow the fenestrae making this filtration layer even more restrictive [32].

1.1.2. Glomerular basement membrane

Post-endothelial settlement, secretion of ~147 distinct ECM proteins from GECs and podocytes [33], help establish individual basement membranes for these cell types that collectively combines to form the second filtration layer known as the glomerular basement membrane [34,35]. It is composed mainly from collagens (types I, IV, VI and XVIII subunits), laminins (α5, β2 and γ 1), nidogen-1 and heparin sulfate proteoglycans (HSPGs) such as agrin and perlecan. As revealed by scanning electron microscopy (Figure 2a), the GBM forms an ~4-10 nm thick highly organized fibrous intermediate filtering mesh [36,37]. Heterogeneous pores averaging 10 nm in diameter additionally span across the structure of the GBM. The GBMs placement in-between podocytes and GECs fixes them in-place via cell-ECM adhesion receptors such as integrin-β1 [38] while allowing inter-cellular communications through secreted signaling factors [1].

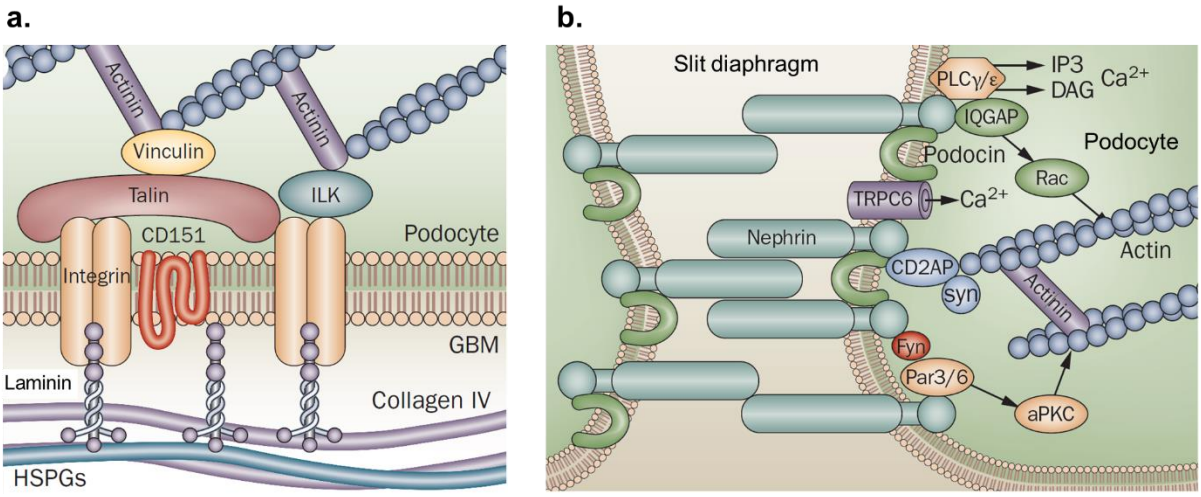

Figure 2: Interplay of interactions between the three distinct layers of the GFB.
(a) Interactions between basal GBM and apical Podocytes forming the perivascular layers of the filtration barrier. Proteins that help cement the podocytes upon the GBM such as integrin, actinin, ILK, vinculin, talin, and the tetraspanin CD151 are shown. These proteins represent only a small subset of identified molecules. **(b)** Tertiary FPs from opposing podocytes forming the slit diaphragm. Important slit diaphragm proteins such as nephrin, podocin, actinin, CD2AP and TRPC6 along with their interactions with the actin cytoskeleton are shown. These proteins represent only a small subset of identified molecules found within the SD. Actinin: α-actinin-4; aPKC: atypical protein kinase C; integrin: α3β1 integrin; CD2AP: CD2-adaptor protein; DAG: diacylglycerol; GBM: glomerular basement membrane; HSPGs: heparan sulfate proteoglycans; ILK: integrin-linked kinase; IP3: inositol 1,4,5-triphosphate; Par 3: Partitioning defective 3; Par6: Partitioning defective 6; PLC: phospholipase C; syn: synaptopodin; and TRPC6: transient receptor potential-like channel 6. Modified from [17].

1.1.3. Perivascular podocytes as the final renal gate-barrier

Ultimately, the third and final filtration layer comprises of polarized epithelial cells known as podocytes appropriately named after their unique cyto-architecture. During early development, these cells express distinct markers that help define apico-basal polarity essential for establishing tight boundaries across cell surfaces. From the onset of kidney development until its maturity, these cells constantly evolve anatomically. Beginning from a columnar and finally maturing into an elaborately stretched epithelial morphology they eventually form larger primary and finer tertiary membrane projections also known as foot processes or pedicels (FPs) that firmly wrap around the glomerular capillaries [39]. The larger primary/major FPs are formed from microtubules and other intermediate filaments whereas actin forms the tertiary FPs with focal adhesion (FA) proteins such as vinculin mediating their anchorage to the GBM [40].

Tertiary FPs from neighboring podocytes wrap around the capillaries in a structurally porous interdigitating pattern forming ~30-50 nm wide small slits known as the slit diaphragm (SD [41–43]; Figure 1e and Figure 2b). SD serves as the final discharge port for primary urine and sub-70 kDa molecules [44,45]. Multiple protein complexes forming a combination of homotypic and/or heterotypic interactions either in *cis* or *trans* configurations span within the intercellular SD junction to not only help bridge the gap

but also to impart functionality. The first amongst these to be identified was the transmembrane protein nephrin [46,47] found to form homotypic *trans* interactions; meaning two nephrin molecules expressed within the FPs from opposing podocytes, were found to interact through their ECDs [48,49]. In addition to this, nephrin was also found to form heterotypic *cis* interactions via its cytoplasmic binding partner called CD2-adaptor protein (CD2AP) with another integral component of the SD called podocin as demonstrated in Figure 2b [50]. Both, nephrin and podocin have been identified as key regulators maintaining the structural integrity of the SD [50,51]. Mutational inactivation of the genes responsible for the expression of these proteins have been linked to congenital nephropathy resulting from SD collapse as a consequence of FP effacement [52,51]. Apart from nephrin and podocin, large adhesion receptors such as FAT1 [53] can also be found within the SD forming homotypic *trans* interactions whereas smaller receptors like Neph1 form heterotypic *cis* connections with nephrin and FAT1 as shown in Figure 1e [54,55]. Being primarily an intercellular junction, the SD additionally also contains components commonly found within adherens and tight junctions such as Zonula Occludens-1 (ZO-1; [56]).

The SD, therefore, acts as the final portal for primary urine ultrafiltration. Since podocyte morphology predominantly dictates SD formation, this highlights the importance of cell polarization signaling within the early stages of kidney development. The interplay between polarity determinants and different SD proteins has been heavily investigated. Nephrin and Neph1, for instance, have been shown to interact with the partitioning defective 3 (Par3/human homologue of the *Drosophila melanogaster* protein Bazooka)- partitioning defective 6 (Par6)-atypical protein kinase C (aPKC) complex [57] as shown in Figure 2b. Genetic mutants within this complex have been linked with abnormal SD formation due to effaced FPs causing proteinuria [58–60]. Another important polarity complex, known as the Crumbs (CRB) complex has been shown to work alongside the Par3-Par6-aPKC complex [61] that influences podocyte mobility for apical sorting. Formation of the SD, thus, marks the boundary between the basal versus apical regions of the GFB, which in turn provide it with the much needed elastic robustness.

1.2. Glomerular diseases

Chronic kidney disease (CKD) is a progressive condition that poses a significant public health problem affecting nearly 10% of the global population, which translates to ~800 million individuals [62]. Its prevalence amongst the aged population, women and/or individuals suffering from diabetes mellitus and hypertension makes it one of the leading causes of mortality globally. The mutual dependence of CKD with cardiovascular diseases and the irreversible renal damage that inevitably leads to kidney failure underscores the need for its early detection alongside development of prevention methods for better treatment strategies [63].

In most cases, kidney disorders are more often than not accompanied by proteinuria originating essentially from a damaged glomerular filter. As can be seen from Table 1, its evident from the GFBs structure that aberrations within one or multiple layers of the GFB arising from genetic mutations within the functional components of the barrier are probable causes for the apparent loss in filter integrity [10,64]. From a clinical standpoint, two distinct types of glomerular diseases can be recognized, namely, Nephrotic or Nephritic syndrome based upon their underlying pathologies.

Nephrotic syndrome is defined not only by the presence of heavy proteinuria but also by the onset of additional conditions such as increased serum albumin and peripheral edema. Predominantly caused by either focal segmental glomerulosclerosis or membranous nephropathy, disease histology can be characteristically described with the presence of lesions within the glomerular tuft. This is additionally accompanied by a disruption of podocyte-podocyte or podocyte-GBM interactions leading to a leaky GFB [65–67]. Nephritic syndrome, on the other hand, leads to hypertension along with the presence of blood in the urinary filtrate, a condition known as hematuria; in addition to proteinuria. The disease can alternatively also manifest into acute fluid retention in some cases. This syndrome is indicative of acute glomerulonephritis with a variety of factors such as circulating platelets, GBM, resident GECs and MCs being responsible for its etiology [68,65].

Glomerular disease progression strongly indicates that either alterations within or ablation of the GFBs unique apico-basal cellular orientation, are the root causes of irreversible renal damage inevitably resulting in total kidney failure [64,69]. Despite extensive research on the GFB, the molecular mechanisms underlying the establishment and maintenance of apico-basal polarity, remain inadequately

understood. This provides compelling reasons to further investigate polarity determinants governing cellular placement within the GFB to better understand neonatal events leading up to the establishment of proper renal functioning.

Table 1: Proteins linked to mesangial, GBM and podocyte-associated glomerular diseases.
Actinin: α-actinin-4; CD2AP: CD2-adaptor protein; GBM: glomerular basement membrane; LMX1B: LIM homeobox transcription factor box 1 beta; and TRPC6: transient receptor potential-like channel 6. Modified from [17].

Disease	Protein	Function and mechanism
Mesangium-associated defects		
IgA nephropathy	Unknown	Enhances immunogenicity of poorly galactosylated IgA1 O-glycoform
GBM-associated genetic defects		
X-linked Alport syndrome	α5 collagen type IV	Major GBM component
Thin basement membrane diseases	α3 or α4 collagen type IV	Major GBM component
Pierson syndrome	Laminin β2 chain	Interacts with integrin α3β1; links GBM to actin cytoskeleton
Nail–patella syndrome	LMX1B	Regulates Nephrin, Podocin, CD2AP and α3/α4 collagen type IV
Podocyte-associated genetic defects		
Congenital nephrotic syndrome of the Finnish type	Nephrin	Anchors SD to the cytoskeleton
Congenital nephrotic syndrome type 2	Podocin	Scaffold protein-links plasma membrane to cytoskeleton
Familial nephrotic syndrome type 3	Phospholipase Cε1	Involved in cell junction signaling and glomerular development
Nephrotic syndrome	CD2AP	Adapter protein that anchors the SD to the actin cytoskeleton
	α-Actinin-4	Actin filament cross-linking protein
	TRPC6	Receptor-activated nonselective calcium-permeable cation channel with mechanosensation

1.3. The Crumbs complex

The Crumbs (CRB) protein complex is one of the key determinants of apico-basal polarity that assists with cell-cell junction formation particularly within epithelial cells. It's a highly conserved protein complex composed from four core proteins, namely, the name giving single-pass transmembrane protein Crumbs and its three intra-cellular adapter proteins named as PALS1 or membrane protein palmitoylated 5/MPP5,

PALS1-associated tight junction homologue (PATJ) and LIN7c [70,71]. The CRBs protein was first identified in *Drosophila melanogaster* embryos using deletion mutants, wherein a drastic loss in organization could be observed within ectodermally derived primary epithelial tissues [72,73]. The protein, thus, derived its name from the morphological appearance of the heavily damaged epidermis having cells that exude ‘crumbs’ of cuticle. Following its discovery, CRBs and their orthologues have been associated with multiple important cellular functions.

Within *Drosophila*, the interplay of interactions between CRB-Stardust (Sdt; PALS1 in mammals)-Patj along with the PAR6-aPKC complex helps to establish the adherens junctions between cells. Simultaneously, complementing negative feedback from the Scribble (Scrib)-Discs large (DLG)-lethal giant larvae (Lgl) and Yurt-Coracle complexes regulate the maintenance of apico-basal polarity [74,75]. In addition to polarity determination, CRBs proteins have also been shown to regulate cell proliferation by stimulating the Hippo [75–79] and Notch [80,81] signaling pathways. Structurally, *Drosophila melanogaster* CRB (*Dm* CRB) contains a small intracellular tail harboring two conserved domains, namely, the PSD-95/Discs-large/ZO-1 (PDZ)-binding motif (PBM) encoded by the “ERLI” amino acids (aa) and the 4.1/Ezrin/Radixin/Moesin (FERM)-binding motif (FBM). Its long ECD, however, contains multiple epidermal growth factor (EGF)-like repeats interspersed with three Laminin globular (G)-like domains (Lam G) [71]. Following its discovery in *Drosophila*, numerous CRB orthologues have additionally been identified in a range of organisms, including humans, mice and zebrafish (Figure 3). But, its role as a polarity determinant in epithelial cells seems to be evolutionarily conserved across phyla [82,72].

In contrast to *Drosophila*, humans express three CRBs paralogues, namely, Crumbs homolog 1 (CRB1), Crumbs homolog 2 (CRB2), and Crumbs homolog 3 (CRB3) with CRB3 further having two splice variants CRB3A and CRB3B (Figure 3a). Cell type-specific expression of the different CRB paralogues within different tissues during embryogenesis highlights the importance of this unique polarity determinant. CRB1 is predominantly found within the human retina and brain with specific mutations associated with multiple ocular dystrophies ranging from autosomal recessive retinitis pigmentosa (RP) to congenital blindness with Lebers congenital amaurosis (LCA; [61,83–85]) CRB1 expression has been detected in the postnatal stages of the murine eye especially within the developing iris, the ventral part of the neural tube and the hypothalamic regions with persistent expression until maturity [86]. Expression of

CRB1 has been extensively linked to the maintenance of adherens junctions with mutations highlighting morphologies similar to *Dm* CRB [87].

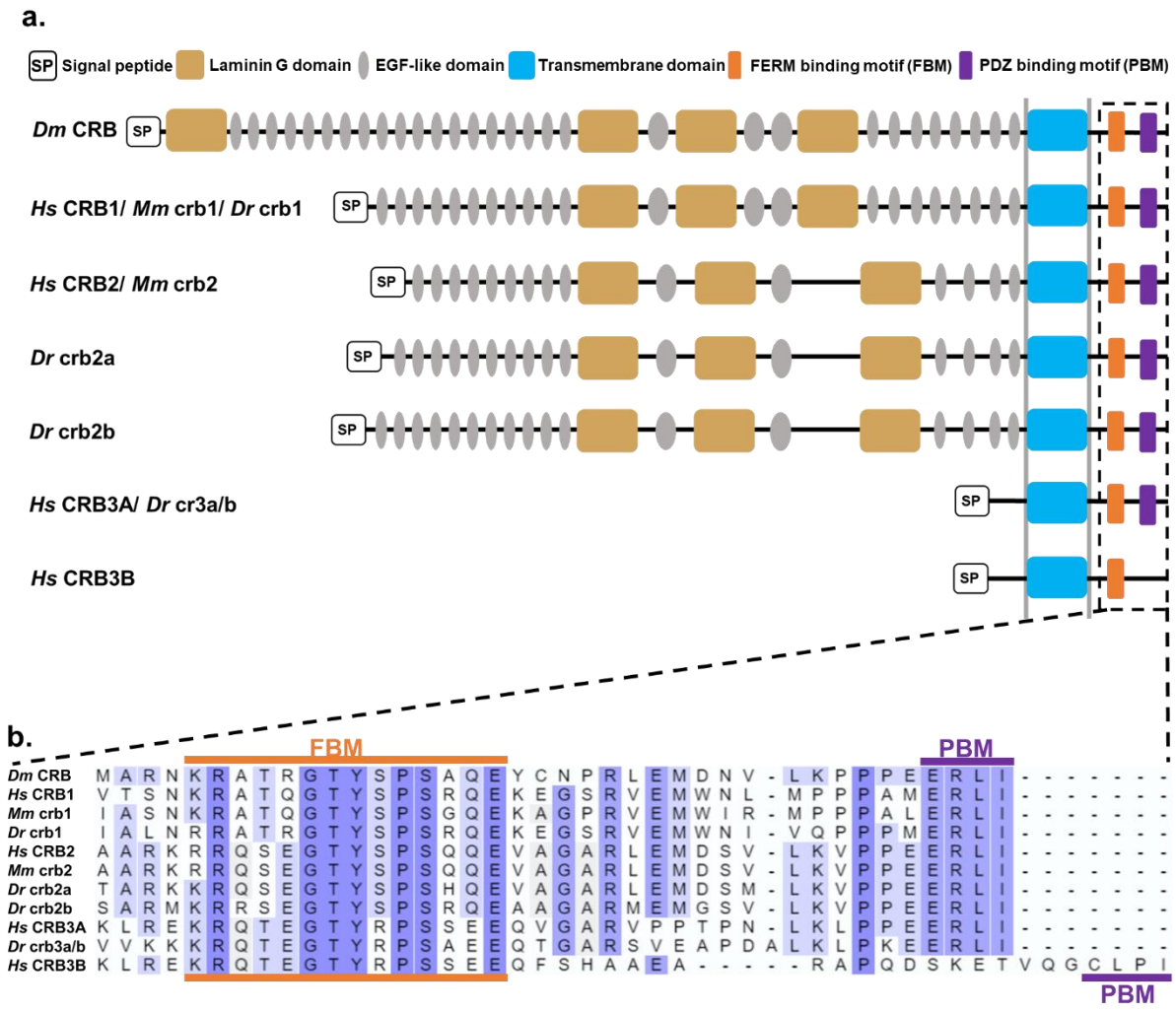

Figure 3: Differences between Crumbs ortho- and paralogues.
(a) Graphic representation of the different CRB homologues found within fruit fly (*Dm*), humans (*Hs*), murine (*Mm*) and zebrafish (*Dr*). Modified from [82]. **(b)** Multiple sequence alignment generated from UniProt for different CRB homologues shown in **(a)** highlighting the amino acid sequences for the conserved intracellular domains FBM and PBM. Conserved amino acids are highlighted (lavender) with lighter tones indicating reduced conservation across species. *Dm*: *Drosophila melanogaster*; FBM: FERM-binding motif; *Hs*: *Homo sapiens*; *Mm*: *Mus musculus*; PBM: PDZ-binding motif and *Dr*: *Danio rerio*.

On the other hand, expression of mammalian CRB2 has been predominantly identified during early embryogenesis [88,89], fetal retinal epithelia [90], brain [91], and kidney [92–96] with lower expression within the heart, placenta and lungs [90]. Along with CRB1, CRB2 was found to be crucial for retinal development and maintenance [97–99]. Finally, CRB3 isoforms are ubiquitously expressed in almost all epithelial tissues [93,100] with prominent prevalence in the kidney [101,102]. While murine kidney immunostainings have demonstrated CRB3 enrichment within the glomeruli and tubules, CRB2 seems to be enriched solely within the glomerulus. Recent research

also suggests a collective function for CRB2 and CRB3 since their combined expression was able to rescue nephrocyte-specific *Dm* CRB knockouts [93]. While the conserved intracellular domain (ICD) of CRB2 and CRB3 proteins has been extensively investigated, the role of CRB2s extracellular domain (ECD) remains poorly understood. Given the crucial role of CRB2 in kidney development, elucidating the functions of its ECD could provide significant insights into glomerular diseases.

1.3.1. CRB2 and disease-associated CRB2 mutations

Structurally, human CRB2 is a 1285 aa protein closely resembling *Dm* CRB due to its large ECD that contains 15 EGF-like repeats interspersed with three Lam G-domains [103]. Similar to other CRBs proteins, its ICD harbors the two conserved domains which govern its interactions with other protein complexes to induce signaling [71,75,61].

Comparing the mutational studies performed with CRB2 across phyla, highlights its cell- and tissue-specific roles. For instance, complete CRB2 knockout (KO) studies in mice have been embryonically lethal with anomalies identified at the gastrulation stage [88]. Other investigations done in zebrafish demonstrated a loss of podocyte FPs combined with SD degeneration [94]. Additionally, nephrin mislocalization within these mutants further hints towards CRB2s influence upon the localization of essential SD proteins.

Biallelic pathogenic human CRB2 gene mutations have also been associated with the development of CRB2-related syndrome. This has been articulated as a rare clinical disorder manifesting into a phenotypic triad. Common variations of this triad include symptoms such as enlargement of brain ventricles or ventriculomegaly, congenital nephrotic syndrome of the Finnish type, persistent proteinuria, steroid-resistant nephrotic syndrome (SRNS) and elevated levels of maternal serum- and amniotic-alpha-fetoproteins (AFP; [61,95,104–106]). The occurrence of severe symptoms associated with CRB2 gene mutations further emphasize its importance. Strikingly, majority of CRB2-related renal disorders have been linked with point mutations that fall within its large ECD as shown in Figure 4 [61]. However, the functions of this domain remain largely elusive till date.

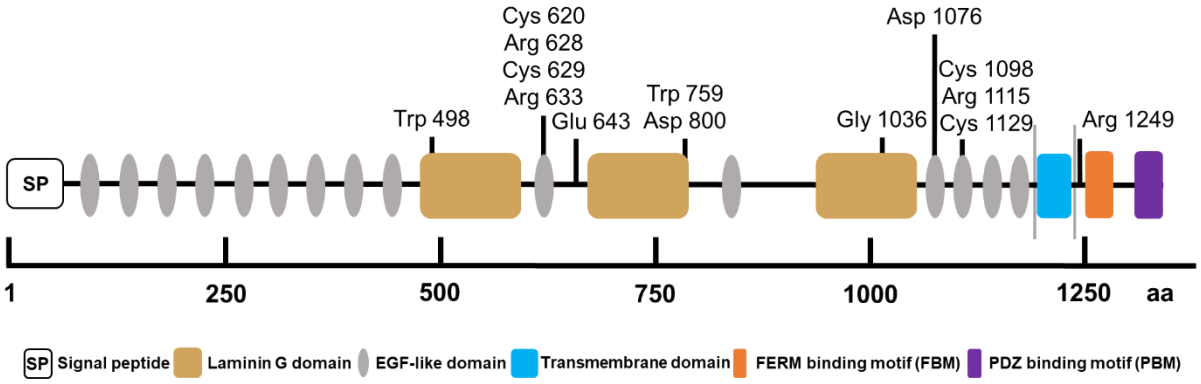

Figure 4: Structure of Crumbs homolog 2 with disease-associated point-mutations.
aa: amino acids. Modified from [61].

1.4. Motivation and Goals

Kidney development requires a complex interplay of multiple proteins during embryogenesis wherein time-dependent expression of the apico-basal determinant CRBs protein has been demonstrated to be extremely crucial [92]. The role of the evolutionarily conserved ICD of CRBs proteins has been extensively investigated across phyla [101,107,75]. However, the role of the ECD remains poorly understood. The current study aimed to investigate the nanoscale localization and the cellular working mechanism of an essential apico-basal marker CRB2. Since the discovery of CRBs in *Drosophilla* [72] it has been shown to be crucial within early developmental stages with KO mutants exhibiting embryonic lethality. We build upon the hypothesis that the long ECD of CRB2 might be involved in a multitude of protein-protein interactions. The interaction partners could, therefore, mediate signal transductions leading to an asymmetric distribution of CRB2. This asymmetric distribution might in turn form the basis for CRBs-related essential cellular functions such as cell polarity determination.

Structurally complex proteins such as CRB2, make it extremely difficult to synthesize the protein *in-vitro*. Instead, the more recently introduced *in-silico* structure prediction tools namely, AlphaFold2 [108] and RoseTTaFold [109] help serve as viable alternatives to estimate a proteins native conformation. In recent times, these tools have even become the gold-standard for studying native protein conformational states.

One of the primary goals for this thesis was to identify the precise 3-D localization of CRB2 within kidney glomeruli. As opposed to what has already been shown earlier [92], we aimed to visualize the localization of CRB2 within the SD with nanometer-

scale accuracy. Comparing its location against other well-known SD markers such as nephrin and podocin [96], would also help us attain a deeper understanding of SD architecture with respect to podocyte morphology.

Subsequently, moving from a tissue-to-cellular level, this thesis aims to address questions relating to the role of CRB2s ECD on protein mobility, functional conformation and its downstream intracellular interaction partners. Stable expression using viral transduction of fluorescently tagged CRBs isoforms and ECD/ICD-specific deletion mutants within human immortalized podocytes [110] help provide an *in-vitro* system that can closely mimic SD morphology. Exploiting this set-up with a combination of different well-known microscopic techniques allows for a comprehensive profiling of cultured cells expressing either wild type (WT) or mutant versions of CRBs' isoforms.

Utilizing the eGFP labelled CRBs constructs, we examine the membrane mobility of CRB2 and CRB3A within regions between neighboring cells and also free membrane regions. The primary comparison between the two isoforms would help establish essential structure-function relationships. Following which, the comparison of the effect of specific ECD/ICD mutants on membrane mobility will help to further elucidate the effect of either the ECD and/or its interactions mediated by the conserved ICDs, FBM or PBM.

Elucidating the mechanism with which CRB2 is able to regulate the cortical actomyosin-cytoskeleton would help clarify essential developmental processes occurring within the kidney such as establishment of the apico-basal polarity. Finally, this thesis will try to clarify the exact protein conformation of interacting CRB2-CRB2 molecules occurring within podocyte foot processes of the SD.

2. Methods

2.1. Mice handling and tissue preparation

All experimental procedures pertaining to mice were conducted by Dr. Annika Möller-Kerutt in the workgroup of Professor Thomas Weide (Institute of Molecular Nephrology, Münster). Experimental methods involving animals were approved and conducted in accordance to the guidelines provided by the German regional authorities (Az.: 84–02.04.2014 A405; LANUV). Animal housing was kept pathogen-free with free access to tap water and normal animal chow. Mice were perfused with 4%PFA in PBS before the kidneys were harvested. Removed kidneys were either prepared for sectioning using a vibratome or for glomeruli extraction.

2.1.1. Kidney tissue preparation

The extracted kidney tissues were prepared by Dr. Annika Möller-Kerutt in the workgroup of Professor Thomas Weide (Institute of Molecular Nephrology, Münster). Kidney tissue was immersed with 10% sucrose for cryo-sectioning. Each kidney was first halved longitudinally and subsequently incubated again with 4% PFA in PBS for 1-2 hours at room temperature (RT). Fixed sample was then cut using a vibratome into 100-µm thick slices and then subjected to immunostaining.

2.1.2. Glomeruli extraction

Glomeruli from murine kidney were provided by Dr. Annika Möller-Kerutt from the workgroup of Professor Thomas Weide (Institute of Molecular Nephrology, Münster). Kidneys were cut into tiny pieces using a scalpel with 3 ml HBSS. Cut pieces were then subjected to treatment with collagenase II (1mg/ml) in HBSS at 37°C for 30 minutes. After incubation, the sample was moved onto a 100-µm nylon tissue sieve and washed using 30 ml HBSS. Subsequently, the suspension was passed through another sieve of 70-µm pore size and washed with 15 ml PBS. Finally, the suspension was passed through a sieve of 40-µm pore size. Retained glomeruli could then be transferred using a pipette into a 15 ml reaction tube. The flow-through also contained tubules and was separated from the glomeruli by centrifuging for 10 minutes at 2000 rpm. Finally, the supernatant was discarded and the glomeruli pellet was resolved in

PBS containing 0.5% Triton X-100. Glomeruli were always pipetted using a 1 ml Eppendorf® tip that was cut to avoid glomerular shearing. The tubes and tips used were always pre-coated with PBS containing 0.5% Triton X-100 so as to avoid glomerular sticking.

2.2. DNA cloning

Cloning inserts were generated by Dr. Annika Möller-Kerutt and Rebecca Rixen from the workgroup of Professor Thomas Weide (Institute of Molecular Nephrology, Münster). Synthetic codon-optimized or human CRB2-WT (aa 1-1285) encoding cDNA inserts with GFP- or HaloTag within the 13th EGF-like repeat in the ECD (inserted after Aspartate at 1095) were introduced into pENTR plasmids. Using site-directed mutagenesis, these plasmids were mutated to generate CRB2 deletion mutants such as CRB2-ΔEGF10 (missing aa 582-663), CRB2-ΔLG1-2 (missing aa 447-804), CRB2-ΔLG1-3 (missing aa 431-1047), CRB2-ΔExtra (missing aa 108-1094) and CRB2-ΔIntra (missing aa 1260-1285). Similarly, the expression cassette was generated encoding cDNA inserts for an eGFP-tagged version for CRB3A-WT or for a truncated form lacking the ICD (CRB3A-Basic) as described earlier [101]. The pENTR plasmids were shuttled into pINDUCER21_Puro or pQCXIP_Puro plasmids using LR Clonase according to the manufacturer's instructions as described earlier to generate inducible or constitutive constructs, respectively [111,112].

Finally, an additional control cassette was generated using pQCXIP_mCherry_ Gateway (GW)_Puro (provided by Ms. Sabine Wirths) as the base plasmid. A PCR amplified mCherry product having a stop codon and attB attachment sites for incorporation into the gateway cassette was produced. Using LR clonase reaction, as per the manufacturers' instructions, the destination plasmid was generated as the pQCXIP_mCherry_GW_mCherry_Puro (referred to as mCherryx2) construct. All details about constructs and primers are summarized in Section 3.1 within Table 2 and Table 3.

2.3. Cell culture

2.3.1. Cultivation of cell lines

Human Embryonic kidney (HEK GP2 293) and immortalized AB8/13 human podocytes were the two renal cell lines cultured during the course of this thesis. Cell were cultured on 10 cm culture flasks at 5 % CO_2 and 33 °C (AB8) or 37 °C (HEK GP2 293) in cell specific culture medium [110,113]. AB8/13 cells were cultured in RPMI1640 medium supplemented with 10 % fetal bovine serum (FBS), penicillin/streptomycin, supplement mixture and Amphotericin B whereas HEK GP2 293 cells were cultured in DMEM media supplemented with 10 % FCS, penicillin/streptomycin, sodium pyruvate and L-glutamine (Table 8). Cells were passaged every 2-3 days depending upon flask confluency. For passaging, cells were treated with 1 ml of 10x Trypsin-EDTA for 5 min. at 33 °C (AB8) or for 3 min. at 37 °C (HEK GP2 293). Cells were re-suspended with 10 ml of fresh medium and a fraction of the cell suspension was transferred into a new flask.

2.3.2. Transient transfection for viral production

All transfections using the doxycycline-inducible (pINDUCER21) plasmids for lentiviral particle production were performed by Dr. Annika Möller-Kerutt and Rebecca Rixen from the workgroup of Professor Thomas Weide (Institute of Molecular Nephrology, Münster).

Transfections using the constitutive (pQCXIP) plasmids for retroviral particle production were done on the packaging cell line HEK GP2 293 using jetPRIME® as per the manufacturer's instructions. Prior to transfection (72 h.), 3 x 10^5 HEK GP2 293 cells/60 mm plate were seeded in 3 ml of growth medium. The cells should be 80-90% confluent at the time of transfection. For transfection, 2 µg of target DNA and 2 µg of the envelope plasmid (pVSV-G®) are diluted with 200 µL jetPRIME buffer. The transfection sample is mixed by vortexing. Next the jetPRIME® reagent is vortexed for 5 sec. and quickly spun down before use. 8 µL of the jetPRIME® reagent are added for a 200 µL reaction volume, vortexed for 1 sec., spun down briefly and incubated for 10 min at RT. Finally. 200 µL of the transfection sample is added dropwise onto the cells in serum containing medium, and distributed evenly by gently rocking the plates back and forth and from side to side. Cells are incubated at 37 °C with 5% CO_2 and

transfection medium is replaced by normal cell growth medium 4 h. after transfection. Cells are further incubate at 37 °C and 5% CO_2 for 48 h. Discarded medium is considered and treated as Safety-level 2 (S2)-waste. Retroviral supernatant harvested after 48 h. was directly used for transduction of target cells.

2.3.3. Generation of stable cell lines using viral transduction

All transductions done on AB8/13 podocytes using the produced lentiviral particles were performed by Dr. Annika Möller-Kerutt and Rebecca Rixen from the workgroup of Professor Thomas Weide (Institute of Molecular Nephrology, Münster).

All transductions done on AB8/13 podocytes using the produced retroviral particles were done as follows. Prior to transduction, 0.8 x 10^6 AB8/13 podocytes are seeded with their complete growth medium 12-18 h. before transduction in a 60 mm plate along with 0.25 x 10^6 cells in a six-well plate for titer determination. On the next day, cell growth medium of the 60 mm plate was replaced with 1 ml fresh viral supernatant and 2 ml fresh growth medium. Additionally a serial dilution of the fresh viral supernatant (1ml volume, 10^0, 10^{-1}, 10^{-2}, 10^{-3} and 10^{-4}) was prepared in the six-well plate with 1 ml fresh diluted viral supernatant and 2 ml fresh growth medium. Both plates are incubated at 33 °C and 5% CO_2 for 24 h. Finally, virus-containing transduction medium was discarded and the cells are washed cells 3x with PBS. 3ml of fresh growth medium was added to the cells and further incubated 33 °C and 5% CO_2 for 24-48 h to allow for the gene product to accumulate. Cells are now considered as Safety-level 1 again. Post-incubation cells were selected using 2µg/ml Puromycin at least for 7 days or until plaques are determined with fresh selection medium added after 48 h. After 7 days or when plaques were determined, selected cells are splitted into an Ibidi-plate (3.5 cm^2, 0.6 x 10^6 cells) for determination of protein expression via live-cell imaging and into another flask for long-term cultivation and cryo-storage.

2.3.4. Mycoplasma testing

All generated and received cell lines were tested externally by Eurofins Genomics for mycoplasma contamination. Freshly thawed cells were maintained in culture for at least 2 weeks prior to testing. 80-90% confluent culture flasks with at least 3 day old media was collected. 500 µL of this cell culture media were transferred into a new 1.5

ml tube. The tube was boiled for 10 min. at 95 °C, briefly centrifuged at 17,000 x g for 30 s. 100-200 µL of the final supernatant was transferred into a new 1.5 ml tube was sent for testing.

2.3.5. Freezing and thawing cells

For freezing, cells were grown to ~90% confluency. They were detached using Trypsin-EDTA as mentioned earlier. Cells were re-suspended in the desired concentration using growth medium. Cell suspension was transferred into a sterile centrifuge tube and centrifuged at 1400 rpm for 10 mins with slow deceleration. Supernatant was removed carefully without disturbing the cell pellet and cells were re-suspended in 5 ml freezing medium. Cell suspension with freezing media was transferred into 1 ml cryo-tubes stored in the cryo freezing container and kept at -80 °C for 24h. Cell tubes were later transferred into liquid N_2 for long-term storage.

For thawing frozen cells, first culture media was warmed up to the desired temperature. A new flask was prepared and cell tubes were taken out of liquid N_2 and thawed in warm water-bath for 1-2 min. After disinfection, the cell suspension was pipetted into the new flask, supplemented with growth media and cultivated as desired. 24 h after thawing, the growth media was replaced so as to remove traces of DMSO.

2.4. Sample Immunostainings

2.4.1. Murine Kidney slices for expansion microscopy

100-µm vibratome cut kidney slices were blocked with 3% BSA and 0.1% Triton X-100 in PBS for 12 h. at 4°C. Nephrin, CRB2 and/or podocin primary antibody dilutions (Table 11) with blocking buffer were prepared and the slices were subsequently incubated for 24 h. at 4°C with rotational shaking. The CRB2 primary antibody was a gift from Dr. Jan Wijnholds [114,115]. Post-incubation, the slices were washed three times with blocking buffer for 15 mins. each at RT. Tissue slices were finally incubated with secondary antibody dilutions in blocking buffer overnight (O/N) at 4°C on rotational shaking (Table 12). DAPI staining was performed after 3x15 mins. washing with PBS.

2.4.2. Murine glomeruli for expansion microscopy

Extracted glomeruli were always pipetted using a 1 ml Eppendorf® tip that was cut to avoid glomerular shearing. The tubes and tips used were always pre-coated with PBST buffer (Table 5) so as to avoid glomerular sticking. Unstained glomeruli were first centrifuged at 8000xg for 10 mins and the supernatant was discarded. The glomeruli were re-suspended in PBST. A small dilution of glomeruli were then transferred into a new 1.5 ml Eppendorf® tube which became the working stock. The rest of the glomeruli were re-suspended in PBST and stored at 4°C until needed. The glomeruli within the working stock tube were incubated with DAPI in PBS at 4°C for 2 h. DAPI stained glomeruli were centrifuged again at 8000xg for 10 mins and the supernatant was discarded and re-suspended in 1x PBS. 18mm round coverslips were pre-coated using poly-Lysine for 15 mins. Coated coverslips were transferred into an Ibidi® plate. A small dilution of glomeruli were transferred from the working stock onto the coated coverslip and incubated for 10 mins. Excess liquid was subsequently removed and the glomeruli were further subjected to antibody staining.

Primary goat anti-mouse nephrin antibody dilution was prepared in blocking buffer (Table 5). The coated coverslips were incubated with the primary antibody at 4°C for 48 h. with rotational shaking. Excess liquid was removed and the coverslips were washed three times with 1X PBS at 4°C for 15 mins with rotational shaking. Secondary donkey anti-goat Alexa488 coupled antibody dilution was prepared in blocking buffer. The coated coverslips were incubated with the secondary antibody at 4°C for 48 h. with rotational shaking. Excess liquid was removed and the coverslips were washed three times with 1X PBS at 4°C for 15 mins with rotational shaking. Finally, the glomeruli were re-stained for DAPI at 4°C for 2 h. with rotational shaking. Excess liquid was removed and the coverslips were washed three times with 1X PBS at 4°C for 15 mins with rotational shaking.

2.4.3. AB8/13 human immortalized podocytes for live-cell microscopy

Living AB8/13 podocytes expressing CRB2-WT-Halo and CRB2-WT-eGFP were seeded simultaneously into an Ibidi® plates for live-cell microscopy at the desired cellular density of ~40% confluency. HaloTag staining with JaneliaFluor 646® was performed as per the manufacturers' instructions. First, co-cultured cells were washed

three times with PBS pre-warmed to 33°C. JaneliaFluor 646® was diluted with pre-warmed growth medium from a 200 µM stock solution made with DMSO down to a final concentration of 4 µM. Cells were subsequently incubated with the diluted dye-medium mixture for 1 hour at 33°C with 5% CO_2. Finally, cells were washed three times with pre-warmed normal growth media for 10 mins. each before transferring the plate to the microscope.

2.4.4. AB8/13 human immortalized podocytes for spatial distribution analysis, expansion microscopy and vinculin-actin immunostainings

Living AB8/13 podocytes expressing the desired construct and cultured either on coverslips (expansion microscopy) or Ibidi® plates (spatial distribution analysis) were first washed three times with PBS pre-warmed to 37°C. Cells were subsequently fixed with 4% PFA in PEM buffer (Table 5) also pre-warmed to 37°C. Fixation was performed in the incubator at 33°C with 5% CO_2 for 10 minutes after which the cells were washed three times with 1X PBS at RT. The cells could then either be imaged directly as in the case for spatial distribution analysis or maximally be stored for 1 week at 4°C before being immunostained for expansion microscopy or vinculin-actin staining.

For expansion microscopy, co-cultured podocytes expressing CRB2-WT-eGFP and CRB2-WT-Halo fixed as described above were first immunostained using the GFP-Booster nanobody. Nanobody dilution was prepared in blocking buffer (Table 5). The coated coverslips were incubated with the blocking buffer for 15 mins. at 4°C with rotational shaking and then incubated with the primary antibody at 4°C for 2 h. also with rotational shaking. Excess liquid was removed and the coverslips were washed three times with blocking buffer at 4°C for 5 mins with rotational shaking. The coverslips were then washed two times with 1X PBS at 4°C for 5 mins with rotational shaking to get rid of Triton X-100. The coverslips were then washed two times with AB8/13 growth medium at 4°C for 5 mins with rotational shaking. HaloTag staining with JaneliaFluor 549® was performed as per the manufacturers' instructions. JaneliaFluor 549® was diluted with ice-cold growth medium from a 200 µM stock solution made with DMSO down to a final concentration of 4 µM. Cells were subsequently incubated with the diluted dye-medium mixture for 1 hour at 4°C with rotational shaking. Finally, cells were washed three times with ice-cold normal growth media for 10 mins. each and DAPI stained for 5 minutes at 4°C with rotational shaking. Before proceeding with processing

the sample for expansion microscopy, the cells were washed three times with 1X PBS at 4°C with rotational shaking and finally stored in 1X PBS.

For vinculin-actin immunostainings, podocytes either non-transduced or expressing one of the two CRBs isoforms, CRB2-WT-eGFP or CRB3A-WT-eGFP were seeded into Ibidi® plates. The cells were fixed as described above. Post-fixation, the plates were subjected to blocking buffer (PBS containing 3% BSA and 0.5% Triton X-100) for 15 mins. at 4°C with rotational shaking. Plates were then incubated with primary anti-vinculin antibody diluted in blocking buffer O/N at 4°C with rotational shaking. Cells were washed three times with blocking buffer for 15 mins. each at 4°C with rotational shaking. After washing, cells were incubated with goat-anti mouse Atto550 conjugated secondary antibody diluted in blocking buffer for 1 hr. at 4°C with rotational shaking. Plates were washed three times with blocking buffer for 15 mins. each at 4°C with rotational shaking. Finally, actin staining was performed with Phalloidin-Atto 647N also diluted in blocking buffer and incubated for 1 hr. at 4°C with rotational shaking. Before nuclear staining, plates were washed three times with 1X PBS for 5 mins. each at 4°C with rotational shaking. Nuclear staining was performed with DAPI diluted in 1X PBS for 5 mins. each at 4°C with rotational shaking. Before imaging, plates were washed three times with 1X PBS at 4°C and finally kept in PBS.

2.5. Expansion microscopy protocol

2.5.1. Murine kidney slices

Immunostained 100-µm vibratome cut kidney slices were treated with freshly prepared 1 mM MA-NHS in 1X PBS for 2 hours at RT. The slices were washed afterward with 1X PBS three times. Before embedding the tissue slices in an acrylamide gel, they were incubated in monomer solution (Table 6) for 1 hour at 4°C. Gelation chamber was built using #1.5H coverslips as described [116]. Slices were incubated with gellation solution (Table 7) and another coverslip was placed on top of the tissue to close the chamber. A humidified environment was created by placing a wet paper towel in a box and the gelling chamber was placed within this box and incubated at 37°C for 2 hours. Post-gelling, the glass around the tissue was removed and excess gel was cut. Gelled tissue slides were digested with freshly prepared digestion buffer with 8 u/ml Proteinase K (Table 5) O/N at 37°C. Once digested, the samples were incubated in

UltraPure water with three to four water exchanges every 30 mins. Nuclear re-staining was performed using DAPI for 30 mins.

2.5.2. Murine glomeruli

Immunostained glomeruli on a coverslip placed inside an Ibidi® plate were incubated with freshly prepared 2 mM MA-NHS in 1X PBS for 1.5 hours at RT. The coverslips were then washed three times with 1X PBS at 4°C for 15 mins. each. Coverslips were then incubated with monomer solution (Table 6) at 4°C for at least 45 mins. Monomer solution was aspirated. Gelling solution (Table 7) was applied on a piece of parafilm sticking on a microscope slide and the coverslip was inverted such that the glomeruli would be embedded inside the solution. Volume of gelling solution defined the height of the gel and gel height was maintained at least 2x the height of the sample (average glomerular height was estimated to be ~70-100 µm [117]). A humidified environment was created by placing a wet paper towel in a box and the microscope slide with the inverted coverslip on parafilm was placed within this box and incubated at 4°C for at least 2 hours. Post-gelling the embedded cassette was removed from the humid chamber, the parafilm was removed and the coverslip with the gel was immersed in digestion buffer (Table 5) with 8 u/ml Proteinase K at 37°C for 3.45 hours with rotational shaking. The gels were then washed three times with 1X PBS at 4°C for 30 mins. each and then incubated in collagenase buffer (1× HBSS supplemented with 0.7 mM $CaCl_2$) with 5 mg/ml collagenase at 37°C for 3.45 hours [118]. Finally, the sample was washed three times with 1X PBS at 4°C for 30 mins. each, re-stained using DAPI at 4°C for 30 mins. and immersed in UltraPure water O/N at 4°C. After O/N incubation, water was exchanged three to four water times with incubation steps of 30 mins. each at 4°C before imaging.

2.5.3. AB8/13 human immortalized podocytes

Fixed and stained AB8/13 podocyte co-culture coverslips expressing CRB2-eGFP-WT and CRB2-Halo-WT were incubated with freshly prepared 2 mM MA-NHS in 1X PBS for 1.5 hours at RT. The coverslips were then washed three times with 1X PBS at 4°C for 10 mins. each. Coverslips were then incubated with monomer solution (Table 6) at 4°C for at least 45 mins. Monomer solution was aspirated. Gelling solution (Table 7)

was applied on a piece of parafilm sticking on a microscope slide and the coverslip was inverted such that the cells would be embedded inside the solution. Volume of gelling solution defined the height of the gel and gel height was maintained at least 2x the height of the sample. A humidified environment was created by placing a wet paper towel in a box and the microscope slide with the inverted coverslip on parafilm was placed within this box and incubated at 4°C for at least 2 hours. Post-gelling the embedded cassette was removed from the humid chamber, the parafilm was removed and the coverslip with the gel was immersed in digestion buffer (Table 5) with 8 u/ml Proteinase K at 37°C for 4.5 hours with rotational shaking. The gels were then washed three times with 1X PBS at 4°C for 30 mins. each. Finally, the sample was re-stained using DAPI at 4°C for 30 mins. and immersed in UltraPure water O/N at 4°C. After O/N incubation, water was exchanged three to four water times with incubation steps of 30 mins. each at 4°C before imaging.

2.6. Microscopic acquisition

Unless otherwise stated, all images acquired during the course of this thesis were done using the Zeiss LSM 880 coupled with an Airyscan detector.

2.6.1. Expansion microscopy

In order to image expanded gels, Ibidi® plates were incubated with poly-D-Lysine for at least 5 mins. at RT. Excess liquid was removed and the plates were dried by N_2 purging. A piece of the expanded gel containing the sample could then be positioned within the plate. The gel pieces were then immersed with RT UltraPure water and imaged using the 40x water immersion (WI) objective NA 1.1 on the Zeiss LSM 880 using the Airyscan detector set to super-resolution (SR) mode. For each sample type, z-stack images were acquired for the expanded gels. Additionally, z-stack images of the immunostained samples were also taken using the same objective prior to gel embedding. The nuclear staining images using DAPI taken before and after the expansion microscopy protocol served to estimate the average expansion factor obtained from each experimental run.

2.6.2. FRAP measurements

AB8/13 podocytes expressing different inducible CRBs-GFP constructs were seeded in Ibidi® plates such that the plates achieved 70% confluency on the day of measurement. Two days before the measurement, cells were cultured in media supplemented with 200 nM doxycycline with medium change every 24 hours to achieve optimal expression. Based on the localization of the signal, two distinct regions of interest (ROI) were chosen, namely, within overlapping cell membrane duplets (OM; Figure 5 a) or within the free plasma membrane (PM; Figure 5c). Three plates from three different days were chosen to take measurements from each cell type. A minimum of 30 measurements were recorded from at least 15 different cells from every plate. The plate triplicates, therefore, provided for at least 90 FRAP measurements from every cell type. All the measurements were performed at 33°C and 5% CO_2 with the Zeiss LSM 880 using the 40x WI objective, NA 1.2 with a completely opened pinhole (601 µm). All measurements were performed on the gallium arsenide phosphamide-photomultiplier tube (GaAsP-PMT) detector. The detector gain and laser power was adjusted based on signal saturation.

For each FRAP curve, a constant frame acquisition speed was estimated based on previous measurements done with cells constitutively expressing CRB3A-WT [101]. In order to eliminate fluctuations within the recovery curve introduced from the proteins' turnover cycle, a general rule of thumb was obeyed that required the acquisition speed to be <5% of half-time of protein recovery. Deducing from previous works [101,119,120], acquisition speed was thus always kept constant at 130ms (<5% of 3s). An additional 20 ms gap was introduced to fulfil the 150 ms (5%of 3s) frame acquisition speed. Initial assessment of CRB2-WT, however, revealed a bi-phasic recovery that reached its plateau almost 2 minutes after bleaching. In order to accommodate for this variation, the FRAP curves were recorded under two different time resolutions. This was done by creating two different acquisition blocks with the Experiment Designer feature in Zen Black (Zeiss®). The acquisition gap interval was, therefore, switched from the initial 150 ms/frame (6.6 Hz.) for the first 30 seconds to 1s/frame (1 Hz.) for 1.5 minutes. Finally, the bleaching parameters were maintained so that a bleach time of 75 ms (=50% of frame acquisition speed) was achieved using the 405, 458, 488 and 514 nm lasers giving a final bleaching depth of at least ~75%.

Initial testing with doxycycline concentrations provided that typically protein expression initiated after 12 hours of induction. Hence, FRAP measurements from each plate were strictly completed within 6 hours. For each measurement, three circular spots (Ø 2 µm) were positioned representing the bleached, bleach correction and background correction regions. Sample acquisition spots for bleaching and background correction were carefully positioned to avoid inclusion of intracellular eGFP enriched vesicles. Each FRAP was manually assessed after acquisition was completed and measurements with vesicular intrusions or cell movements were discarded.

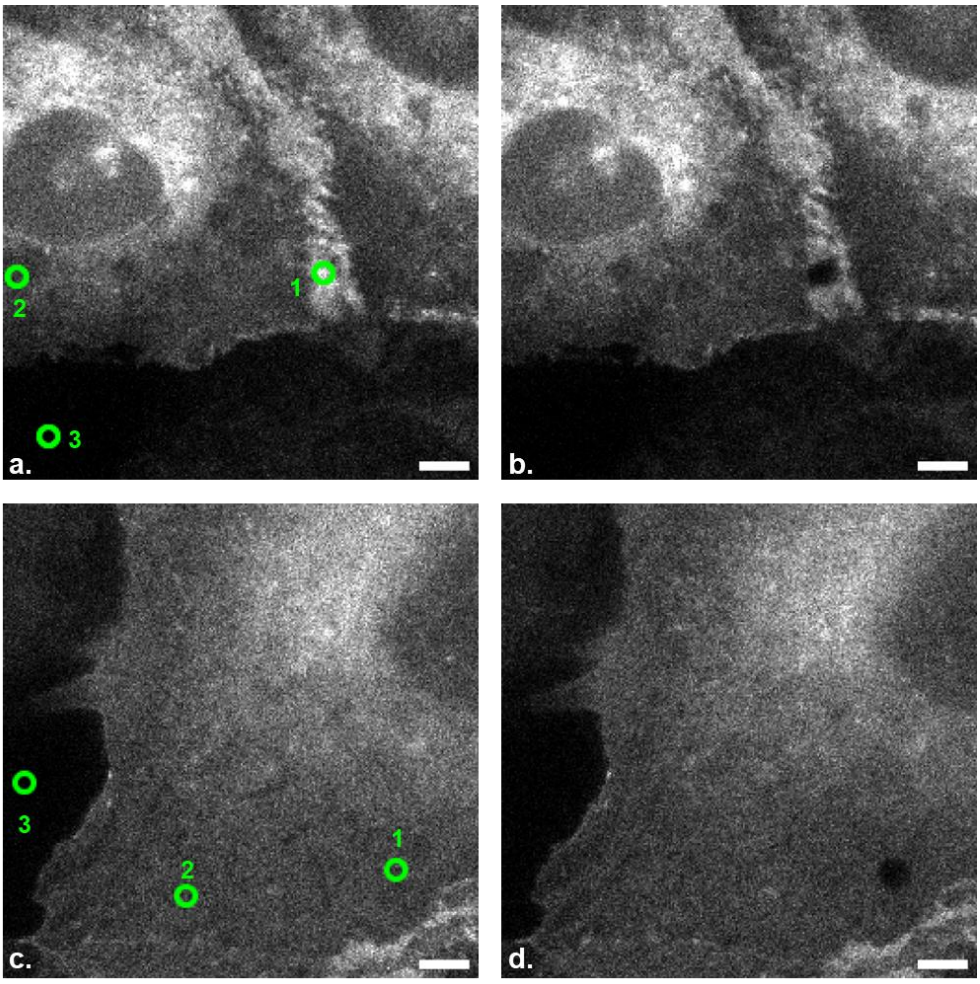

Figure 5: Distinct regions chosen for FRAP measurements.
(a, b) Image showing representative FRAP measurement performed within two overlapping cellular membranes (OM). **(c, d)** Image showing representative FRAP measurement performed within free plasma membrane (PM). **(a, c)** Pre-bleach image showing bleached (1), bleach correction (2) and background correction (3) ROIs. **(b, d)** First image frame acquired instantly after bleaching. All measurements were performed with a 40X water immersion objective; NA 1.2 on Zeiss LSM 880. Scale bar: 5 µm.

2.6.3. Spatial distribution acquisition

Approximately 20,000 AB8/13 podocytes constitutively expressing either GFP fusions of CRB2-WT, CRB3A-WT or CRB3A-Basic were mixed with 20,000 AB8/13 podocytes expressing mCherryx2 to achieve a confluency of ~20% in an Ibidi® plate. Six plates were prepared for each co-culture combination. Three plates from each combination were fixed with 4% v/v PFA in PEM and the nuclei were counterstained with DAPI after one day of cultivation. This plate was labelled as Day 1. The cells within the other plates for each combination were then cultured for seven days with medium change every two days. At the end of the week, these plates were also fixed with 4% v/v PFA in PEM and the nuclei were counterstained with DAPI. This plate was labelled as Day 7. For both Day 1 and Day 7 plates, the entire plates' observation area (Ø 21 mm) was imaged using a 10x air objective, NA 0.8 on the Zeiss LSM 880. In total, 400 tiles covering ~23x23 mm with a 20% overlap and averaging two times were acquired from each co-cultured plate. The resulting tile scan image was then stitched using the native LSM software (Zen Black, Zeiss®). Subsequent image analysis was performed using FiJi [121].

2.6.4. Live cell measurements

Approximately 80,000 eGFP tagged CRB2-WT and CRB3A-Basic cells were co-cultured with 80,000 mCherryx2 tagged AB8 podocytes to attain a confluency of ~60-70%. A total of 25 tiles spanning ~1.5x1.5 mm with a 20% overlap along with averaging twice were acquired using the 40x WI objective, NA 1.2 on the Zeiss LSM 880 every 15 mins for 15 hours. The final tile scan image was then stitched using the stitching function in Zen Black (Zeiss®).

Subsequently, 40,000 CRB2-WT-eGFP cells were co-cultured with 40,000 CRB2-WT-Halo cells. After staining with the HaloTag dye as mentioned in Section 2.4.3, a total of 25 tiles spanning ~1.5x1.5 mm with a 20% overlap along with averaging twice were acquired using the 40x WI objective, NA 1.2 on the Zeiss LSM 880 every 15 mins for 15 hours. The final tile scan image was then stitched using the stitching function in Zen Black (Zeiss®).

2.6.5. Z-stack acquisitions for protein localization within AB8/13 podocytes

In order to more accurately analyze protein accumulation, five Z-stacks were acquired as 16-bit images for each cell type, namely, mCherryx2, CRB3A-Basic, CRB3A-WT, CRB2-WT, CRB2-ΔIntra, CRB2-ΔPBM, CRB2-ΔFBM and CRB2-ΔExtra. Each Z-stack was acquired using the 40x WI objective, NA 1.2 on a Zeiss LSM 800 with the Airyscan detector set to SR mode.

2.6.6. AB8/13 podocytes immunostained for actin and vinculin

AB8/13 immunostained podocytes were measured. Only two cells exhibiting overlapping cellular membranes were considered as a duplet. Cell duplets from three different plates were measured and a total of no less than 10 measurements were recorded per plate. All images consisted of four channels representing either DAPI (405 nm), eGFP (488 nm), vinculin (561 nm) or phalloidin/actin (633 nm) stainings. All channels were acquired using the 63x oil immersion (OI) objective, NA 1.4 on a Zeiss LSM 880 with four time averaging and Digital gain set to 1.0. The channels were acquired using the GaAsP-PMT detector. The pinhole for each channel was set to 1 Airy unit (AU), which was kept constant for each measurement; DAPI (43 µm), eGFP (51 µm), vinculin (57 µm) and phalloidin/actin (66 µm). The master gain for each channel; DAPI (650), eGFP (650), vinculin (650) and phalloidin/actin (600) was adjusted based on signal saturation and kept constant for all measurements. The laser power for each channel; DAPI (1.5%), eGFP (2%), vinculin (2%) and phalloidin/actin (2%) was kept constant for all measurements. Acquisition filters for each channel; DAPI (410-485 nm), eGFP (493-580 nm), vinculin (566-630 nm) and phalloidin/actin (638-754 nm) were fixed so as to avoid signal bleed-through and kept constant for all measurements. Please note the pixel dwell time varies for each image acquired due to different zoom settings and ranged between 2-4µs.

2.7. Data analysis

Images acquired using the Zeiss LSM 880 coupled with the Airyscan detector were processed first on the native LSM software (Zen Black, Zeiss®). Images acquired using the Airyscan detector were processed using Zen Black (Zeiss®) before being exported for further processing. Unless stated otherwise, images analysis was performed basically using the software's FiJi [121] and OriginPro, Version 2021b (OriginLab Corporation®, Northampton, MA, USA).

2.7.1. FRAP measurements

After acquisition, each FRAP measurement was manually assessed and erroneous measurements were discarded. All measurements were recorded using two blocks using the Experiment Design feature in Zen Black (Zeiss®). The blocks allowed us to record with two different acquisition speeds. After acquisition, the TimeConcatenation feature was used to generate the final FRAP measurement. The concatenated FRAP measurement data was then exported as a time lapse videos and also as a table of intensity values measured within three spots, namely, bleached (1), bleach correction (2) and background correction (3) as shown in Figure 5. Using OriginPro, a macro was generated that implemented the formula highlighted in Equation 1:

$$I(t)_{recovery} = \frac{I_1(t) - I_3(t)}{I_1(\text{pre-bleach}) - I_3(t)} \; x \; \frac{I_2(\text{pre-bleach}) - I_3(t)}{I_2(t) - I_3(t)}$$

Equation 1

where, $I(t)_{recovery}$ stands for measured recovery at time point t, $I_1(t)$ represents the intensity at given time point t within the bleached region, I_1(pre-bleach) stands for the intensity measured within the bleached spot at time point 0, $I_2(t)$ represents the intensity at given time point t within the bleach correction region, I_2(pre-bleach) stands for the average intensity measured within the bleach correction region at time point 0 and $I_3(t)$ represents the intensity measured within the background correction spot at given time point t. Finally, the macro normalizes the intensity values and removes the first five time points which represented the intensity in the bleached region before bleaching and replots the normalized intensity values against time to generate a FRAP

recovery curve. Each single FRAP curve were then fitted to a bi-exponential curve fit (Equation 2) and the respective recovery time constants Tau 1 (T1), Tau 2 (T2) and the mobile fractions were tabulated for each cell line.

$$\boldsymbol{f(t) = A_1 \cdot (1 - e^{-t/\tau_1}) + A_2 \cdot (1 - e^{-t/\tau_2})}$$

Equation 2

where, the amplitude for each of the two fractions was denoted as A_1 and A_2 respectively. A_1 indicates the mobile fraction and time constants T1 and T2 were interpreted as diffusion speeds. Individual box plots were generated to compare differences within the time constant T1 and maximum recovery obtained for each protein. A two-way analysis of variance (ANOVA) was used to test for statistically significance. Comparison amongst the average time constant obtained for each cell line was done using the “Tukey Test” with α=0.05, α=0.01 and α=0.001. All statistical calculations were performed using OriginPro 2021b (Origin lab).

2.7.2. Spatial distribution analysis

The three-channel stitched Day 7 images obtained from Zen Black were imported into FiJi and split into their constituent channels. From each co-culture image, the eGFP channel, representing the different CRBs proteins was utilized to generate a binary image mask based on manual signal thresholding. The image was subsequently eroded and dilated three times so as to smoothen the sharp edges within the binary mask. FiJis particle analyzer feature was utilized to identify any cell clusters bigger than 10 μm^2. The perimeter for each of the identified clusters was recorded for all CRBs cell types. The size of the largest cluster identified in CRB3A-Basic served as the threshold for random clusters. Only clusters larger than the threshold found within CRB2-WT and CRB3A-WT were kept while smaller clusters were removed. Finally, the data was normalized using the exact cell count that could be identified from the DAPI channel. The created binary mask was overlaid with the image from the DAPI channel and using the particle analyzer feature, the cell density within each cluster could be estimated. The number of cells in clusters versus all cells counted within the plate were drawn as a box plot. To compare the growth pattern a "Two-sample t-Test"

was used for pairwise statistical significance testing between CRB2-WT, CRB3A-WT and CRB3A-Basic.

2.7.3. Live cell measurements

The two-channel stitched images obtained from Zen Black for CRB2-WT-eGFP co-cultured with mCherryx2 and CRB3A-Basic-eGFP co-cultured with mCherryx2 were then imported into FiJi. The Fire look-up-table (LUT) was applied to the eGFP channel whereas the mCherryx2 channel was greyscaled. The time lapses were subsequently manually checked frame-by-frame and cellular regions showing cell type specific behavior identified. Specific time points of interest from these regions were then cropped and merged into a montage.

Similarly, two-channel live-cell stitched images obtained from Zen Black for CRB2-WT-eGFP co-cultured with CRB2-WT-Halo were re-opened using FiJi. The time lapses were subsequently manually checked frame-by-frame. Specific time points of interest from regions of interest were cropped and merged into a montage.

2.7.4. Z-stack acquisitions for protein localization within AB8/13 podocytes

The 16-bit z-stack single cell images were imported into FiJi after Airyscan processing. For each z-stack, a maximum intensity projection was generated. Subsequently, a circular ROI of 2 µm diameter was either positioned within the overlapping membrane or free plasma membrane regions. The ROIs were used to measure the mean intensity values within these specified regions. A total of three different positions within the projected image were measured for each of the two regions specified above and the measurement was repeated for each z stack image. Therefore, we generated a total of 15 mean intensity values for each region. Finally, we calculated the ratio between the averages of three mean intensities generated from the overlapping region ROIs: the average of the three mean intensities generated from the free plasma membrane region ROIs. This calculation was repeated for each z stack image giving us 5 ratio values/replicates for each cell type. The data from all cell lines was plotted using a box plot and normalized using the mCherryx2 cell line as baseline.

2.7.5. Actin and FA immunostainings

The 16-bit z-stack cell duplet images were imported into FiJi. Line plots were drawn to compare the localization of vinculin versus actin against the eGFP signal which was representative of either CRB2-WT or CRB3A-WT. Additionally, a computer program was created by our collaboration partners in the Institute of Biological Information Processing in Jülich headed by Prof. Dr. Rudolf Merkel. The program measured for parameters such as number, area covered and total size of cell-cell contact.

3. Materials

3.1. Primers and Plasmids

Table 2: List of cloning and sequencing primers.

Target	Direction	Sequence (5'-3')
Cloning primers		
hCRB2-WT	forward	CACCGGGCGCGCCATGGCGCTGGCCAGGCCTGGGAC
hCRB2-WT	reverse	TTAATTAACTAGATGAGTCTCTCCTCCGGTGG
hCRB2-ΔIntra	forward	CTGGCAGCCCGAAAGTGACGCCAGTCTGAGGGC
hCRB2-ΔIntra	reverse	GCCCTCAGACTGGCGTCACTTTCGGGCTGCCAG
hCRB2-ΔExtra	forward	CCTGGCAGCCAGAAAGTGAAGGCAGTCCGAGG
hCRB2-ΔExtra	reverse	CCTCGGACTGCCTTCACTTTCTGGCTGCCAGG
hCRB2 attB1		GGGGACAAGTTTGTACAAAAAAGCAGGCTCCGGGCGCGCCATGGCTCTTGCTAGACCTG
hCRB2 attB2		GGGGACCACTTTGTACAAGAAAGCTGGGTCCTTAATTAACTAGATCAGCCGTTCCTC
mCherry-attB1		GGGGACAAGTTTGTACAAAAAAGCAGGCTCCGTGAGCAAGGGCGAGGAGGATAAC
mCherry-Stop-attB2		GGGGACCACTTTGTACAAGAAAGCTGGGTCTCACTTGTACAGCTCGTCCATGCCGC
Halo SalI	forward	AAGTCGACGGCGGAGGCAGCTCCGAAATCGGTACTGGC
Halo SalI	reverse	AAGTCGACGCCGCCACCGGAAATCTCCAGAGTAG
Sequencing primers		
hCRB2-1	forward	CTGGCACAGAGTGTCAGGCCAC
hCRB2-2	forward	CAGCAGACCATGTCACCACG
hCRB2-2'	reverse	CGTGGTGACATGGTCTGCTG
hCRB2-3	forward	GTGGCGTGGAAGTTGACGAG
hCRB2-4	forward	GCATCTGGCCACACTGGAAC
hCRB2-5	forward	CAGACTGCTGGCCGCTGATTC

Table 2: Continued.		
Sequencing primers		
Target	**Direction**	**Sequence (5'-3')**
hCRB2-6	forward	AGTTGCTGATGGCGCTTGGC
hCRB2-F	forward	TGCTTGTGCCTGTGGACCTG
mCherryx2	forward	GAGCTGTACAAGTCCGGACTC
mCherryx2'	reverse	CTGGGTCTCACTTGTACAGC

3.2. Cell lines and Bacterial strains

Table 3: Table of cell lines produced and bacterial strains used.

Cell line	Description	Origin
AB8/13-WT	Immortalized human podocyte cell line	Prof. Dr. Moin Saleem, University of Bristol, UK Saleem et al. 2002
HEK293T	Immortalized human embryonic kidney cell line	Thermo Scientfic Inc., Waltham, MA, USA
AB8/13 immortalized human podocytes-constitutive expression plasmids		
hCRB2-WT-eGFP	CRB2-WT-eGFP	AG Molekulare Nephrologie Münster Dr. Annika Möller-Kerutt
hCRB3A-WT-eGFP	CRB3A-WT-eGFP	AG Molekulare Nephrologie Münster Dr. Annika Möller-Kerutt
hCRB3A-Basic-eGFP	CRB3A-WT-eGFP mutant, missing aa 335-366	AG Molekulare Nephrologie Münster Dr. Annika Möller-Kerutt
mCherryx2	Double mCherry fusion construct	AG Kubitscheck Sabine Wirths and Rohan Bhatia
AB8/13 immortalized human podocytes-inducible expression plasmids		
hCRB2-WT-eGFP	CRB2-WT-eGFP	AG Molekulare Nephrologie Münster Dr. Annika Möller-Kerutt

Table 3: Continued.		
AB8/13 immortalized human podocytes with Inducible expression		
Cell line	**Description**	**Origin**
hCRB3A-WT-eGFP	CRB3A-WT-eGFP	AG Molekulare Nephrologie Münster Dr. Annika Möller-Kerutt
hCRB3A-Basic-eGFP	CRB3A-WT-eGFP mutant, missing aa 335-366	AG Molekulare Nephrologie Münster Dr. Annika Möller-Kerutt
hCRB2-ΔLG1-2	CRB2 deletion variant, missing aa 447-804	AG Molekulare Nephrologie Münster Rebecca Rixen
hCRB2-ΔEGF10	CRB2 deletion variant, missing aa 582-663	AG Molekulare Nephrologie Münster Rebecca Rixen
hCRB2-ΔLG1-3	CRB2 deletion variant, missing aa 431-1047	AG Molekulare Nephrologie Münster Rebecca Rixen
hCRB2-ΔExtra	CRB2 deletion variant, missing aa 108-1094	AG Molekulare Nephrologie Münster Rebecca Rixen
hCRB2-ΔPBM	CRB2 deletion variant, missing aa 1281-1285	AG Molekulare Nephrologie Münster Dr. Annika Möller-Kerutt
hCRB2-ΔFBM	CRB2 deletion variant, missing aa 1250-1263	AG Molekulare Nephrologie Münster Dr. Annika Möller-Kerutt
hCRB2-ΔIntra	CRB2 deletion variant, missing aa 1260-1285	AG Molekulare Nephrologie Münster Rebecca Rixen
Bacterial strains		
dam$^-$/*dcm*$^-$ Competent *E. coli*		New England Biolabs; C2925H
NEB 5-alpha Competent *E. coli* (High Efficiency)		New England Biolabs; C2987H

3.3. Chemicals, Buffers, Gel stocks and Cell culture components

Table 4: List of chemicals.

Name	Manufacturer; Catalog no.
1 kb Plus DNA Ladder	New England Biolabs; N3200S
4-Hydroxy-Tempo	Sigma-Aldrich; 176141
Acrylamide solution 40%	Sigma-Aldrich; A4058
Agar-Agar	Carl Roth GmbH; 2266.3
Agarose Broad Range	Carl Roth GmbH; T846.2
Agarose Low Melt	Carl Roth GmbH; 6351.5
Ammoniumpersulphate (APS)	Sigma-Aldrich; A3678
Amphotericin B solution	Sigma-Aldrich; A2942
Bovine Serum Albumin (BSA)	Sigma-Aldrich; A7906
Copper(II)-Sulfate Pentahydrate	Thermo Fisher Scientific; C/8560/53
DAPI Solution (1mg/ml)	Thermo Fisher Scientific; 62248
Dismozon Pur	VWR; N11860
Dulbecco's Modified Eagle medium (DMEM), high glucose, no glutamine, no phenol	Thermo Fisher Scientific; 31053044
Dimethyl-sulphoxide (DMSO) Hybri-Max	Sigma-Aldrich; D2650
Doxycycline hydrochloride	Sigma-Aldrich; D3447
EthylenediamineTetra Acetic acid (EDTA)	Carl Roth GmbH; 8040.2
EDTA-di-Sodium-di-Hydrate	Carl Roth GmbH; 8043.3
Ethanol, 100%	Sigma-Aldrich; 32205
Ethanol, 70%	Carl Roth GmbH; T913.3
Fetal Bovine Serum (FBS) SUPERIOR stabile	Bio&SELL GmbH; FBS. S 0615
Guanidine-HCl	Applichem; A1499
Hanks' balanced salt solution (HBSS) with Calcium, Magnesium, Sodium bicarbonate and Phenol red	VWR; L0606-500
Hepes-Buffer (1M)	Sigma-Aldrich; H0887
Immersion medium Immersol W 2010, 20 ml	Zeiss; 444969-0000-000
Immersol™ 518 F	Zeiss; 444960-0000-000
Insulin-Transferrin-Sodium selenite	Roche/Sigma; 11074547001

Table 4: Continued.	
Name	**Manufacturer; Catalog no.**
jetPRIME® DNA- and siRNA-transfection reagent	VWR; 101000015
Carbon Dioxide N35 Cylinder L50	Air Liquide; P1724L50R0A001
LB (Luria/Miller)-Medium	Carl Roth GmbH; X968.1
L-Glutamine 200mM	Sigma-Aldrich; G7513-100ML
Methacrylic acid N-Hydroxy succimide ester (MA-NHS)	Sigma-Aldrich; 730300
MEM Non-Essential Amino Acids Solution (100X)	Gibco (Thermo Scientific); 11140035
N, N'-Methylenebisacrylamide 2%	Sigma-Aldrich; M1533
Paraformaldehyde 32%	Electron Microscopy Sciences; 15714-S
PBS buffer (1X, Dulbecco's)	VWR; A0964.9050
Penicillin/Streptomycin (100x)	Sigma-Aldrich; P4333
PIPES	Sigma-Aldrich; P6757
Poly-L-Lysine solution-0.1 % (w/v)	Sigma-Aldrich; P8920
Puromycin dihydrochloride hydrate	Thermo Fisher Scientific / Life Tech/ AlfaAesar; J61278.MB
Resuspension solution (DNA Mini Prep)	Thermo scientific;
RPMI-1640 Medium (with L-glutamine and sodium bicarbonate)	Sigma-Aldrich; R8758
SOC medium	New England Biolabs; B9020S
Sodium acrylate, 98%	BLDpharm Germany; BD151354 98% (Titration)
Sodium chloride	Carl Roth GmbH; 3957.2
Sodium Pyruvate 100mM	Sigma-Aldrich; S8636
Sterillium® classic pure, Flasche, 1 L (03/2026)	VWR; 115-4028
Technical nitrogen gas cylinder L50	Air Liquide; I4001L50R2A001
N,N,N′,N′-Tetramethylethylenediamine (TEMED)	Sigma-Aldrich; T7024
TRIS	Carl Roth GmbH; 4855.2
Triton X-100	Sigma-Aldrich, X100
Trypsin-EDTA Solution 10X	Thermo Scientific/ Gibco; 15400054
Water (sterile-filtered, BioReagent, suitable for cell culture)	Sigma-Aldrich; W3500

Table 5: List of buffers along with their respective compositions.

Buffer name	Components
Phosphate buffered saline (PBS)	9.55 g/L in UltraPure water
PEM buffer	0.1M PIPES
	1mM EDTA
	1mM MgCl2
	Final pH 7
Blocking buffer for immunofluorescence	1x PBS
	3% BSA
	0.5% Triton X-100
PBST buffer	1x PBS
	0.5% Triton X-100
Digestion buffer for expansion microscopy (Stored as 4.8 ml aliquots in -20°C.) [116] *: Given for final concentration with Proteinase K and water. For 8 u/ml final concentration: 50 µL Prot. K (800U/ml)+ 150 µL UltraPure water to get a final volume of 5ml.	0.3 g or 0.39 g of Tris or Tris HCl (Final conc. 50 mM*)
	0.02 g of 0.5 M EDTA (Final conc. 1 mM*)
	250 µL Triton X-100 (Final conc. 0.5 v/v*)
	3.82 g of 8M guanidine HCl (Final conc. 0.8 M*)
	Proteinase K (Stock: 800 u/ml): Added freshly depending upon conc. needed
	48 ml UltraPure water
	Final pH 8.0

Table 6: Table listing the composition of the monomer solution for Pro-ExM.
Stored as 15 x 600 µL aliquots in -20°C. *: If the Sodium acrylate stock has a yellow tint, then it is of low purity and this could affect the final outcome. [116]

Chemical stocks	Amount (ml) Total: 9.4 ml	Storage (°C)	Final conc.
19 g/50 ml Sodium acrylate*	2.25	-20	8.6 g/100 ml
25 g/50 ml Acrylamide	0.5	4	2.5 g/100 ml
1 g/50 ml N, N'-Methylenebisacrylamide	0.75	4	0.15 g/100 ml
14.6 g/50 ml Sodium chloride	4	4	11.7 g/100 ml
10X PBS	1	4	1X
UltraPure water	0.9	RT	

Table 7: Table listing the formulation of the gelling solution for Pro-Exm.
Monomer solution needs to be thawed at least 30 mins. before usage on ice. APS was always added towards the end. [116]

Amount (µL)	Chemical stocks	Function	Storage (°C)	Final conc.
282	Monomer solution		-20	
6	0.5% 4-hydroxy-TEMPO	Inhibitor	-20	0.01 % (w/v)
6	100% TEMED	Accelerator	-20	2% (v/v)
6	10% APS	Initiator	-20	0.2 % (w/v)

Table 8: Cell culture media composition.

Media	Components
LB media	25g/L in UltraPure water
LB Agar with/ without antibiotics	LB media
	15 g/L Agar-Agar
	Ampicillin sodium salt (Amp): Final concentration 100 mg/ml
	Kanamycin sulphate (Kan): Final concentration 50 mg/Ml
AB8/13 cells	500 mL RPMI 1640
	50ml FBS
	5 ml penicillin/streptomycin
	12.5% (v/v) non-essential amino acids
	12.5% (v/v) insulin transferrin sodium selenite (10 mg/mL)
	12.5% (v/v) sodium pyruvate (100 mM)
	62.5% (v/v) HEPES (1M)
	0.8% (v/v) Amphotericin B (250µg/ml)
HEK293T cells	500 ml DMEM
	50 ml FBS
	5 ml penicillin/streptomycin
	L-glutamine
Freezing media	90% FBS
	10% DMSO

3.4. Antibiotics and Enzymes

Table 9: List of antibiotics used for LB/LB agar.

Name	Manufacturer; Catalog no.
Ampicillin (Amp) sodium salt	Carl Roth GmbH; K029.1
Kanamycin sulphate (Kan)	Carl Roth GmbH; T832.2

Table 10: List of enzymes used along with their function.

Name	Function	Manufacturer; Catalog no.
BP Clonase II (Gateway Enzyme mix)	Gateway cloning	Life Technologies; 11789-020
Collagenase from *Clostridium histolyticum*	Expansion microscopy	Sigma-Aldrich; C7926
FastAP Alkaline Phosphatase		Thermo Fisher Scientific; EF0654
LR Clonase II (Gateway Enzyme mix)	Gateway cloning	Life Technologies; 11791-020
Phusion Hot StartII DNA polymerase	Polymerase chain reaction (PCR)	ThermoScientific; F549S
Proteinase K	Cloning	Life Technologies
Proteinase K	Expansion microscopy	New England Biolabs; P8107S
SalI	Restriction enzyme	Thermo Fisher Scientific; ER0641
SalI (Fast Digest)	Restriction enzyme	Thermo Fisher Scientific; FD0644
T4 DNA Ligase	Cloning	Thermo Fisher Scientific; EL0011

3.5. Antibodies and dyes

Table 11: List of primary antibodies along with their respective dilutions.

Target	Species	Manufacturer	Catalog no.	Dilution / Concentration
CRB2 (mouse)	Rabbit	Dr. Jan Wijnholds group		1:500
Nephrin	Guinea pig	Progen	GP-N2	1:500
Nephrin	Goat	R&D	AF3159	10 µg/ml
Podocin	Rabbit	Sigma	P0372	1:200
GFP-Booster	Alpaca	Chromotek	Gb2AF488-50	1:100
Vinculin	Mouse	Sigma Aldrich	V9131-100UL	1:500

Table 12: List of secondary antibodies and dyes along with their respective dilutions.

Target	Species	Manufacturer	Catalog no.	Dilution / Concentration
Anti-rabbit IgG Alexa488	Goat	Life technologies	A11034	1:1000
Anti-rabbit IgG Alexa594	Goat	Life technologies	A11012	1:500
Anti-rabbit IgG Alexa647	Goat	Life technologies	A21244	1:500
Anti-guinea pig IgG Alexa488	Goat	Life technologies	A11073	1:500
Anti-guinea pig IgG Alexa594	Goat	Life technologies	A11076	1:500
Anti-guinea pig IgG Alexa647	Goat	Life technologies	A21450	1:500
Anti-goat IgG Alexa488	Donkey	ThermoScientific	A11055	1:200
Anti-mouse IgG Atto550	Goat	Sigma Aldrich	43394	1:500
HaloTag ® JaneliaFluor 549		Promega	GA1110	4µM
HaloTag ® JaneliaFluor 646		Promega	GA1120	4µM
DAPI		ThermoScientific	62248	1:2000
Phalloidin-Atto647N		Sigma Aldrich	65906-10NMOL	1:500

3.6. Commercial kits

Table 13: List of commercial kits used.

Name	Manufacturer; Catalog no.
NucleoSpin Gel and PCR Clean-up (50)	Macherey-Nagel; 740609.50
GeneJET Plasmid Miniprep Kit (250x)	Thermo Fisher Scientific; #K0503
NucleoBond Xtra Midi (50)	Macherey-Nagel; 740410.50

3.7. Instruments and Softwares

Table 14: List of instruments used.

Instrument	Manufacturer
35-mm-µ-Ibidi plates	Ibidi, Gräfelfing, Germany
-80°C freezer	Panasonic Healthcare Holdings Co., Ltd. (now PHCbi)
Allegra™ X-22R Centrifuge	Beckmann Coulter, USA
Analytic scales	VWR International GmbH, Darmstadt, Germany
Avanti™ J-30I Centrifuge	Beckmann Coulter, USA
Axiovert 200 microscope cell culture	Zeiss, Oberkochen, Germany
Cell culture flasks (25 and 75 cm^2)	VWR International GmbH, Darmstadt, Germany
Cryo Freezing container	Nalgene/ Thermo Scientific, Schwerte, Germany
Electronic Pippette Pipetus	Hirschmann Laborgeräte, Eberstadt, Germany
Electrophoresis chamber	Bio-Rad Laboratories GmbH, München, Germany
ELGA Ultra Analytic Water Purification System	Purelab, USA
Gel dock Ingenius	SynGene International Limited, UK
Hermle Z 233 MK-2 Centrifuge	Beckmann Coulter, USA
Ibidi Heating System with humidity, Universal Fit	Ibidi, Gräfelfing, Germany
Ice machine AF 80	Scotsman, USA
Incubator (33°C-cell culture)	Binder, Tuttlingen, Germany
Incubator (37°C-cell culture)	Binder, Tuttlingen, Germany
Incubator Ecotron (Bacteria)	Infors HT,Bottmingen, Switzerland
Incubator Incucell (Bacteria)	Gemini, Netherlands
Laboklav Autoclave	SHP Steriltechnik, Germany
LD C-Apochromat 40x/1.1 water immersion objective	Zeiss, Oberkochen, Germany
LD C-Apochromat 40x/1.2 water immersion objective	Zeiss, Oberkochen, Germany
LD LCI Plan-Apochromat 25x/0.8 water/glycerol/oil immersion objective	Zeiss, Oberkochen, Germany
Magnetic stirrer RH basic 2	IKA, Staufen, Germany
NanoDrop 2000C	Thermo Scientific, Schwerte, Germany
PCR Thermocycler-Primus 25 advanced	VWR International GmbH, Darmstadt, Germany
pH 1000L pH meter	VWR International GmbH, Darmstadt, Germany
Pipettes	Eppendorf AG, Hamburg, Germany
Plan-Apochromat 10x/0.45 air objective	Zeiss, Oberkochen, Germany
Plan-Apochromat 63x/1.4 Oil immersion Objektive	Zeiss, Oberkochen, Germany
Sterile laminar flow bench KS12	Heraus, Hanau, Germany
ThermoMixer C	Eppendorf AG, Hamburg, Germany
Vortex Genius 3	IKA, Staufen, Germany
Water bath- Precision GP 10	Thermo Fisher Scientific
Zeiss LSM 880 confocal microscope with Airyscan	Carl Zeiss, Oberkochen, Germany

Table 15: List of sotwares used.

Software name	Application	Manufacturer
FiJi	Image analysis and editing	Wayne Rasband, USA [121]
OriginPro 2021b	Statistical analysis and graphing software	OriginLab Corporation, Northampton, MA, USA.
VectorNTI	Generation and editing plasmid maps, restriction enzyme sites and creation of ligation and gateway cloning products.	Thermo Fisher Scientific
ZEN Black	Microscopic acquisition software	Zeiss, Oberkochen, Germany
ZEN Blue	Microscopic images editing software	Zeiss, Oberkochen, Germany
Huygens Professional 24.04	Software for image deconvolution and 3-D image analysis.	Scientific Volume Imaging, The Netherlands
GeneSnap	Software for imaging Agarose gels.	SynGene International Limited
NanoDrop 2000/2000C	Software for determining DNA concentration.	Thermo Fisher Scientific

4. Results

This work highlights the *in silico* and advanced microscopic methods employed in order to comprehensively investigate the molecular functioning of the protein CRB2. The results obtained from these approaches will be presented in this chapter.

4.1. *In silico* protein structure prediction

As a starting point, we began to look at structural properties of CRB2 and compared it with its other isoform CRB3A. CRB2 is a central single-pass type I transmembrane protein comprising of three sub-isoforms produced from alternative splicing. Isoform 1 conforms to the longest/canonical sequence for this protein as curated by UniProt. The protein is composed of 1285 residues having a molecular mass of ~134 kDa. Its ECD consists of 15 EGF-like domains present in two separated repeat clusters near the N- and C-terminal positions along with three interspersed Lam G domains. The highly conserved ICD harnesses the FERM and PDZ binding motifs. On the other hand, isoform 2, most likely represents the secreted variant of this protein that lacks the transmembrane and ICD domains [103], while, isoform 3 represents a shortened variant composed of only 953 residues with a molecular mass of ~100 kDa.

In contrast to CRB2, CRB3 is a shorter transmembrane protein comprising of only two sub-isoforms. Isoform 1 also known as CRB3A, conforms to the canonical sequence for this protein as curated by UniProt. It represents a protein composed of only 120 residues having a molecular mass of ~13 kDa. The protein lacks any characteristic domain outside the cell but harnesses the highly conserved FERM and PDZ binding motifs on the inside. Similar to isoform 1, isoform 2 presents a slice variant known as CRB3B composed of only 123 residues having a molecular mass of ~13 kDa. CRB3B has a different C-terminal PBM with the “CLPI” aa mutant as opposed to the conserved “ERLI” aa sequence seen otherwise. For the purposes of this study, only the canonical sequences for both CRB2 and CRB3 were selected for comparison and for cell line generation.

4.1.1. Theoretical size estimations for CRB2 and CRB3A

So far, CRB2 has never been crystalized for X-Ray structural analysis. The individual components that make up the protein are well-characterized, however, their 3-D orientation and the final structural conformation are still unknown. Therefore, predicting the molecular arrangement for the different domains requires the use of computational protein modeling approaches. In a first attempt, the average radius of the molecule was estimated. The estimation was based on the premise that the individual protein domains sit like beads-on-a-string. Therefore, the average protein density can be estimated using the molecular weight of the domain from which the domain radius can then be derived [122]. Using this approach, one gets a theoretical radius measurement for the ECD of CRB2 as 21.3 nm. Comparing it with the other kidney specific isoform, CRB3A, we get an almost negligible value.

4.1.2. Protein structure prediction via 3-D computer modelling

In our subsequent approaches, attempts were made to achieve a more precise size estimation. Recent advances in computational modelling algorithms as demonstrated during the biannual Critical Assessment of Structure Prediction (CASP) protein-folding challenge allowed for deep learning neural networks that could accurately predict protein structures in 3-D. Deriving from this, we used the industry gold-standard that is AlphaFold2 (DeepMind [108]). Using the online version available via UniProt, it was possible to retrieve the predicted structures for the entire protein sequence (Figure 6). Comparing CRB2 and CRB3A, it can be seen that the algorithm was able to accurately predict the structure for different domains present within the protein that are the EGF-like and Lam G domains. However, the overall folding accuracy seemed to be hampered especially in the case of CRB2 (Figure 6a). The region between the membrane proximal EGF-like domains and the third Lam G domain has a per-residue confidence score (pLDDT; range from low to high confidence: 0-100) of 60. The score for the region linking the transmembrane domain with the 15th EGF-like domain was ~ <50. Similar results were obtained for CRB3A (Figure 6b), wherein the ECD had a pLDDT score of 60 and the score for the region connecting the transmembrane helix to the ECDs was below 50. The most concerning issue, however, was the inability of the algorithm to distinctively separate the intra- and extra-cellular regions of the protein.

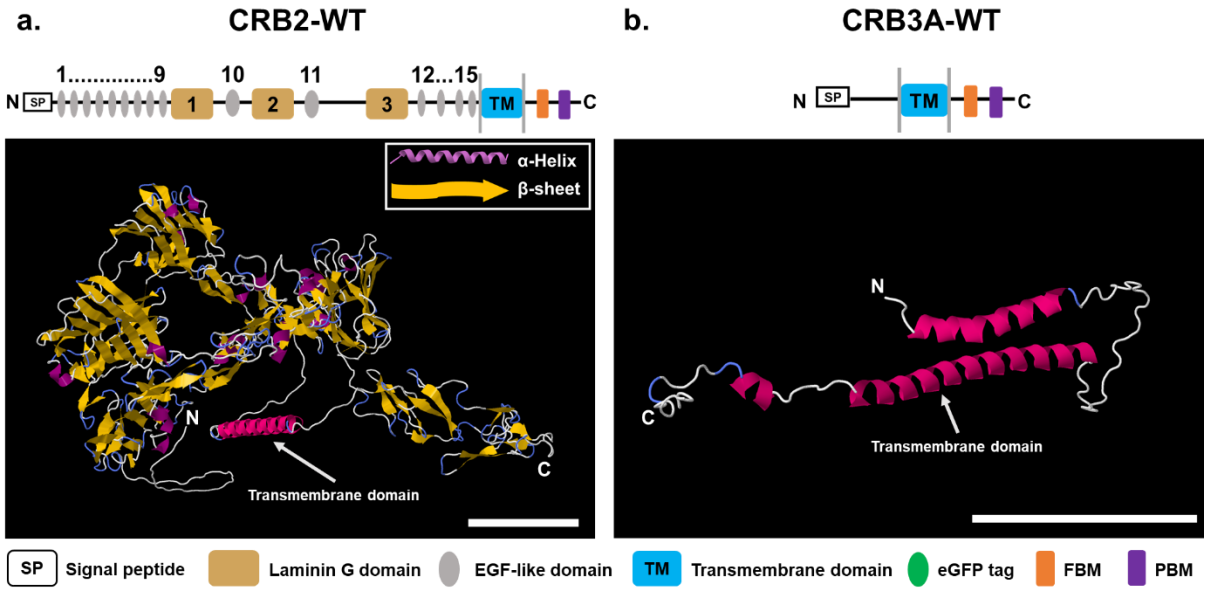

Figure 6: *In silico* Crumbs isoform structure predictions from AlphaFold 2.
(a) Human CRB2-WT; UniProt ID: Q5IJ48. **(b)** Human CRB3A-WT; UniProt ID: Q1A5L0. N: N-terminal of protein; C: C-terminal of protein. Scale bars: 5 nm.

We hypothesized, that the presence of the signal peptide within the sequence might be the cause for these erroneous results. Therefore, the exact signal peptide (SP) cleavage position was estimated using Signal-P, Version 5.0 [123]. CRB2s aa sequences lacking the SP sequence were then re-fed to a downloaded version of AlphaFold 2. However, removal of the SP did not seem to improve the predicted results obtained for CRB2 (Figure 7) and the algorithm was still unable to clearly differentiate between the intra- and extra-cellular regions of the protein.

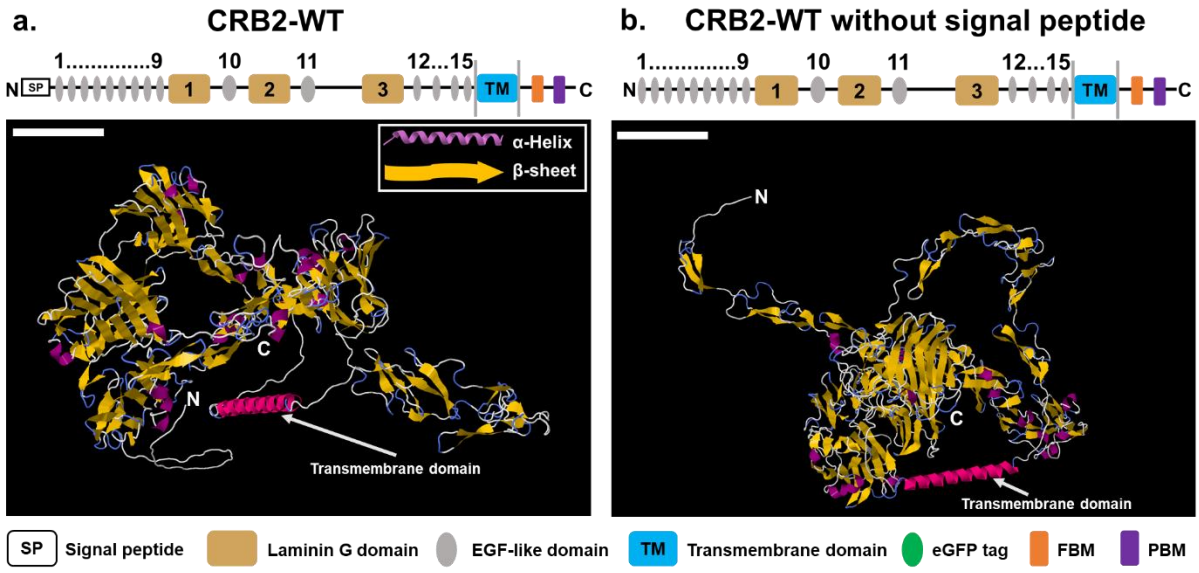

Figure 7: CRB2 structure with and without signal peptide from AlphaFold 2.
(a) Human CRB2-WT; UniProt ID: Q5IJ48. **(b)** Human CRB2-WT missing the initial 31 amino acids that correspond to the signal peptide as predicted by SignalP version 5.0; UniProt ID: Q5IJ48. N: N-terminal of protein; C: C-terminal of protein. Scale bars: 5 nm.

Developing on the existing network architecture of AlphaFold2, a new and improved structure prediction algorithm was introduced, named RoseTTaFold [109]. Switching to the RoseTTaFold molecular modeling software, five possible structures for each protein sequence (Figure 8 and Figure 9) were obtained. For each of the predicted structures, we also receive a tabulated error estimation at every amino acid position along with an overall confidence score. Therefore, in order to optimally represent this data, the five predicted models for every protein sequence were aligned with respect to one another by aligning the best pair of chains between the different structures using Chimera X [124]. Additionally, for every amino acid position the average error estimated from the five models was plotted. The standard deviation within the five error estimations were plotted as error bars to the average error estimated value (Figure 8 and Figure 9). Thus, the final graph created shows an averaged error along with deviations within the errors expected from the five estimations at each amino acid position. This way we can directly visualize how precise the algorithm was at its prediction within different regions of the protein as opposed to just relying on the average confidence score.

As can be seen in the case of the WT isoforms CRB2 and CRB3A from Figure 8, the algorithm always generated an elongated structure with a clear segregation of the ECD from the ICD. For both isoforms, the evolutionarily conserved two intra-cellular C-

terminal PDZ/FERM-binding motifs can be found connected to the transmembrane helix domain with an error estimate of 20 Å (Figure 8 a, b). However, for the ECD especially for CRB2 (Figure 8a), we additionally can visualize the N-terminal EGF-repeats followed by three Lam G domains ending with the membrane-proximal C-terminal EGFs. Simply by overlaying the predicted structures we were better able to distinguish the flexible versus static domains. The N- and C-terminal repeats demonstrate higher variations with error estimates ranging between 5-15Å. Owing to this variation, the N-terminal repeats showcased the most flexibility (Figure 8a; yellow arrow) with the central Lam G domains (gold arrows) acting as a possible hinge like region. The hinge-like region was found to be having a relatively decent prediction since the error estimated was less than 5Å. Depending on the bending angle between the Lam G and N-terminal EGFs, the ECD of CRB2 was then estimated to be somewhere between 40.1 nm to 50.4 nm.

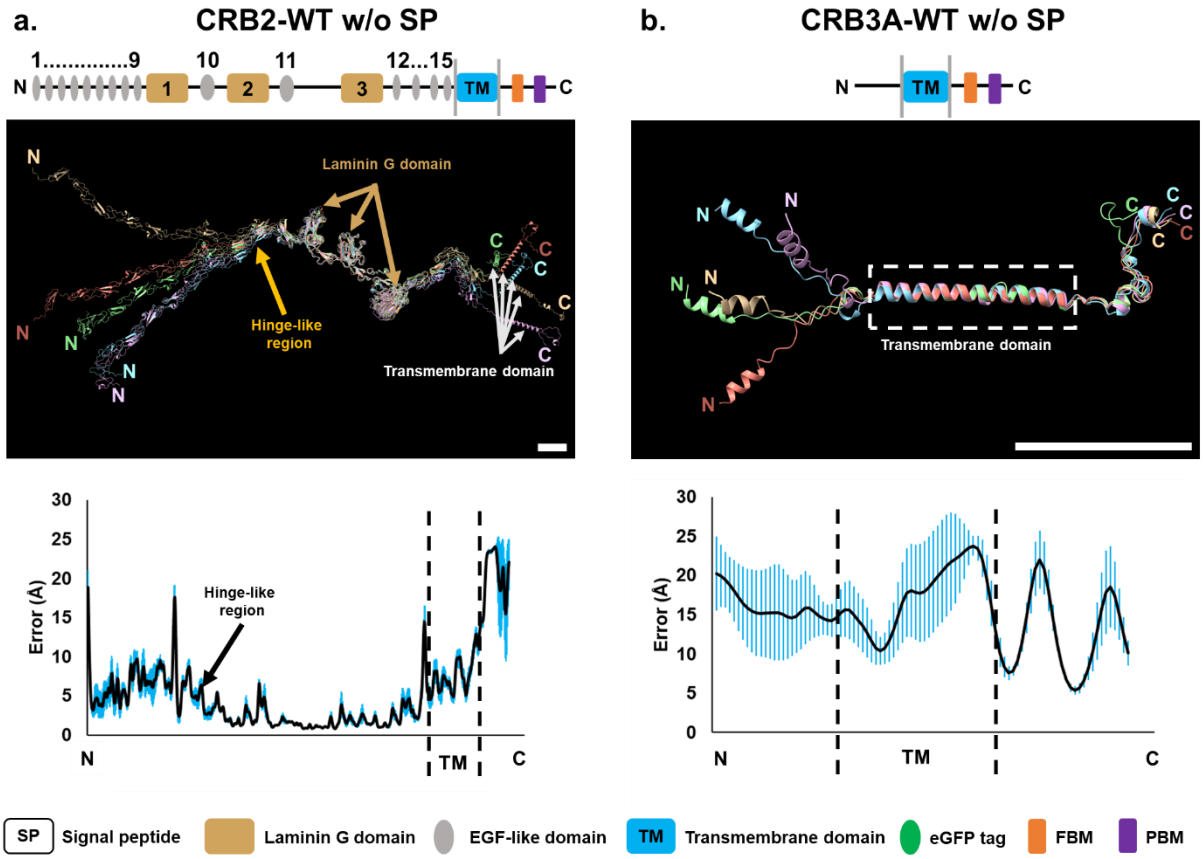

Figure 8: *In silico* Crumbs isoform structure predictions from RoseTTaFold.
(a) Multi-colored overlay of the five predicted structures for human CRB2-WT Isoform 1 missing the initial 31 amino acids that correspond to the signal peptide as predicted by SignalP version 5.0; UniProt ID: Q5IJ48. **(b)** Multi-colored overlay of the five predicted structures for human CRB3A-WT missing the initial 26 amino acids that correspond to the signal peptide as predicted by SignalP version 5.0; UniProt ID: Q9BUF7. Plot of mean error value in Å corresponding to the individual amino acid positions along with its standard deviation obtained from the five predicted structures. N: N-terminal of protein; C: C-terminal of protein. Scale bars: 5 nm.

Finally, utilizing the same algorithm, we then further provided protein sequences for two mutants that were additionally generated for the purposes of this study. First was a control cell line mutant which lacks both the intra-cellular and extra-cellular regions and only harbors an eGFP-tag on its ECD (CRB3A-Basic-eGFP; Figure 9a). The alignment for the models predicted for this mutant were not perfect since one of the models seems to predict a mirrored morphology when overlaid with the other structures. However, the error estimates for all of the 5 predicted models don't show a large deviation. Second was a CRB2-specific dysfunctional mutant (CRB2-ΔExtra-eGFP; Figure 9b) which lacks the entire ECD of CRB2 except for the first and last three membrane-proximal EGFs but has a fully intact ICD. This mutant was tagged at the 13th EGF-domain on the ECD. The prediction for the ECD seems to be highly accurate with error estimates in the range of below 10 Å and the ICD follows the same trend as observed with the WT isoforms (Figure 9b).

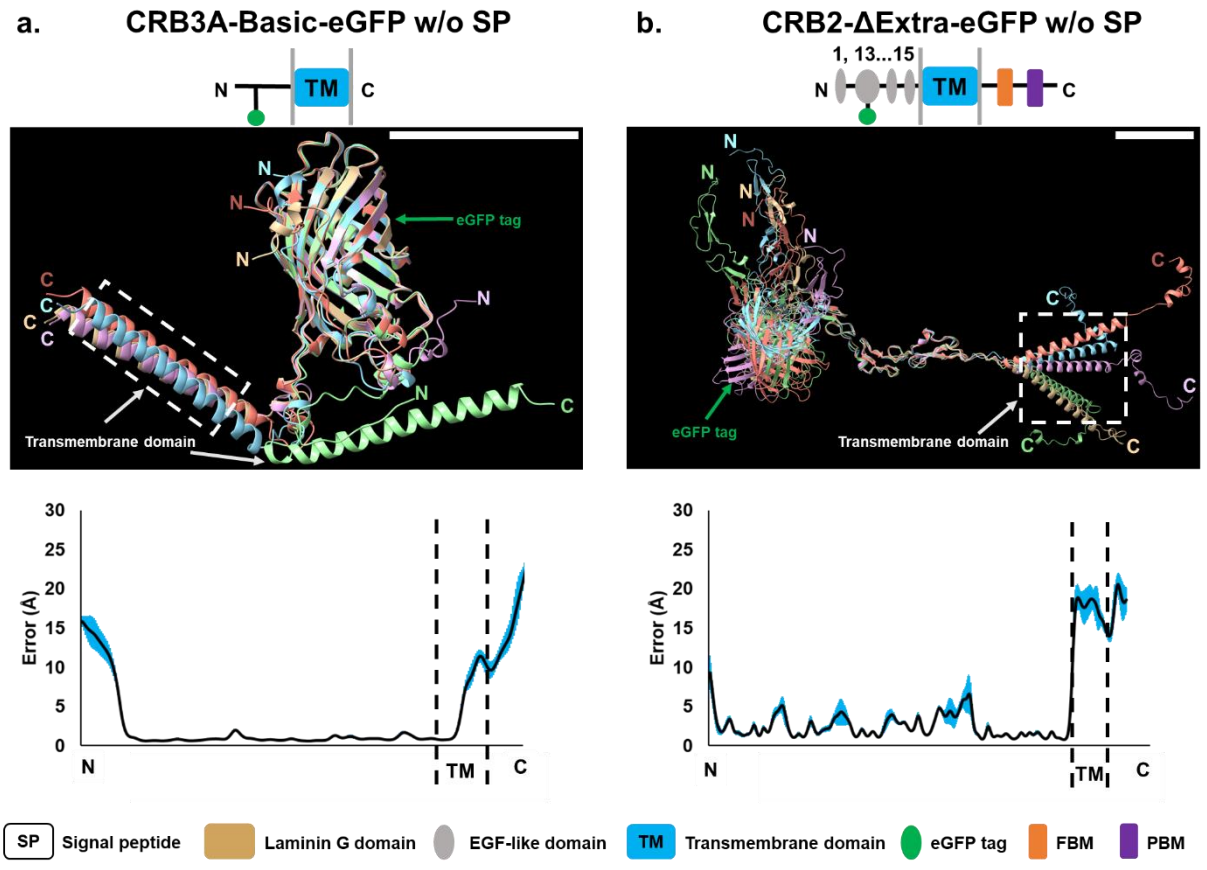

Figure 9: *In silico* Crumbs mutants' structure predictions from RoseTTaFold.
(a) Multi-colored overlay of the five predicted structures for synthetic CRB3A-Basic-eGFP construct. Modified from human CRB3A-WT; missing the initial 26 amino acids that correspond to the signal peptide as predicted by SignalP version 5.0 and the intracellular domains; UniProt ID: Q9BUF7. **(b)** Multi-colored overlay of the five predicted structures for synthetic CRB2-ΔExtra-eGFP construct. Modified from human CRB2-WT; missing the initial 31 amino acids that correspond to the signal peptide as predicted by SignalP version 5.0 and EGF domains 2-12 and all Lam G domains; UniProt ID: Q5IJ48. Plot of mean error value in Å corresponding to the individual amino acid positions along with its standard deviation obtained from the five predicted structures. N: N-terminal of protein; C: C-terminal of protein. Scale bars: 5 nm.

4.2. CRB2 localization within murine kidney glomeruli

CRB2 and CRB3A are the most predominant isoforms expressed in the human and mouse kidney [88,125–127]. Mice lacking CRB2 only within the podocytes seemed to survive but exhibited increased levels of glomerular injury accompanied with foot process effacement and proteinuria. Our mouse kidney co-stainings of CRB2 along with known slit-diaphragm proteins like nephrin and podocin exhibited distinct protein overlaps within the glomerular podocytes [96]. However, the precise localization of CRB2 within the slit diaphragm still seemed to be unresolved.

In order to comparably visualize the intra-glomerular localization of the proteins within the slit diaphragm, a recently introduced high-resolution approach known as expansion microscopy was utilized [116,118]. In the case for kidney slices, it has been shown previously that an isotropic expansion is only possible by including an additional collagenase homogenization step after the generic homogenization treatment using Proteinase K [118]. The typical loop morphology of the slit diaphragm was lost post-expansion when the protocol was performed without this additional collagenase treatment for murine kidney slices [128]. However, it was found later that even if we extract single glomeruli from murine kidney, the glomeruli would not expand homogenously without the additional collagenase homogenization. Figure 10 shows such an example with an almost 3.5 times expanded single glomerulus highlighting the localization of nephrin within the slit diaphragm along with nuclear counter-staining.

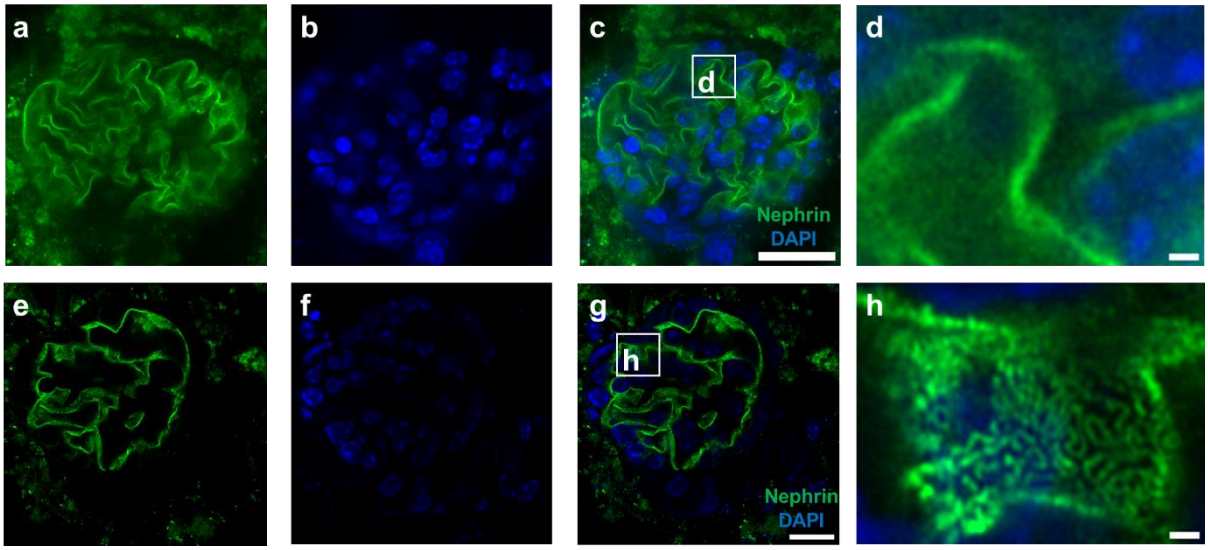

Figure 10: Expanded single WT-mouse glomerulus.
Glomerulus was immuno-stained for nephrin using goat anti-mouse primary and AlexaFluor-488 conjugated donkey anti-goat secondary antibodies. Pro-ExM approach was performed as described using Proteinase K and Collagenase digestion [118]. **(a-d)** Pre- and **(e-h)** Post-expansion samples were imaged using a 40X water immersion objective; NA 1.1 on Zeiss LSM 880 with Airyscan detector. Expansion factor was estimated to be ~3.5x using DAPI. Scale bars: (c, g) 20 µm; (d, h) 1 µm.

Finally, we compared the relative localization of nephrin and podocin with that of CRB2 and nephrin (data courtesy: Annika Möller-Kerutt; [96]). Looking at Figure 11a, we first compare the 3-D distribution between nephrin and podocin. Line plots were drawn starting from the nuclear side so as to identify protein intensity distribution. As expected, podocin seems to be located more close to the podocyte nuclei as compared to nephrin. This distribution also gets highlighted from the line profiles as shown in Figure 11 (b, c; arrows). Podocin clearly localizes more intracellularly as compared with the transmembrane protein nephrin and serves as its binding partner [129,50].

On the other hand, Figure 11 (e, f) shows us the relative distribution of CRB2 in relation to that of nephrin. It is clearly evident that CRB2 distributes very differently than podocin when comparing intensity line plots that were drawn starting from the nucleus. Instead of forming shifted intensity peaks as seen with nephrin and podocin, we see an almost co-localizing intensity distribution for CRB2 and nephrin. This suggests that the two transmembrane proteins localize equidistantly from the nucleus as shown in Figure 11 (e, f; arrows). Their spatial distribution indicates their localization into neighboring bundles on the extracellular surface of podocytes forming interactions with their respective counterparts from the adjoining cell membranes. Therefore, it becomes clear that when two podocytes' membranes inter-digitate to form the slit diaphragm, nephrin and CRB2 are being expressed adjacent to each other forming homotypic nephrin-nephrin and possibly CRB2-CRB2 interactions.

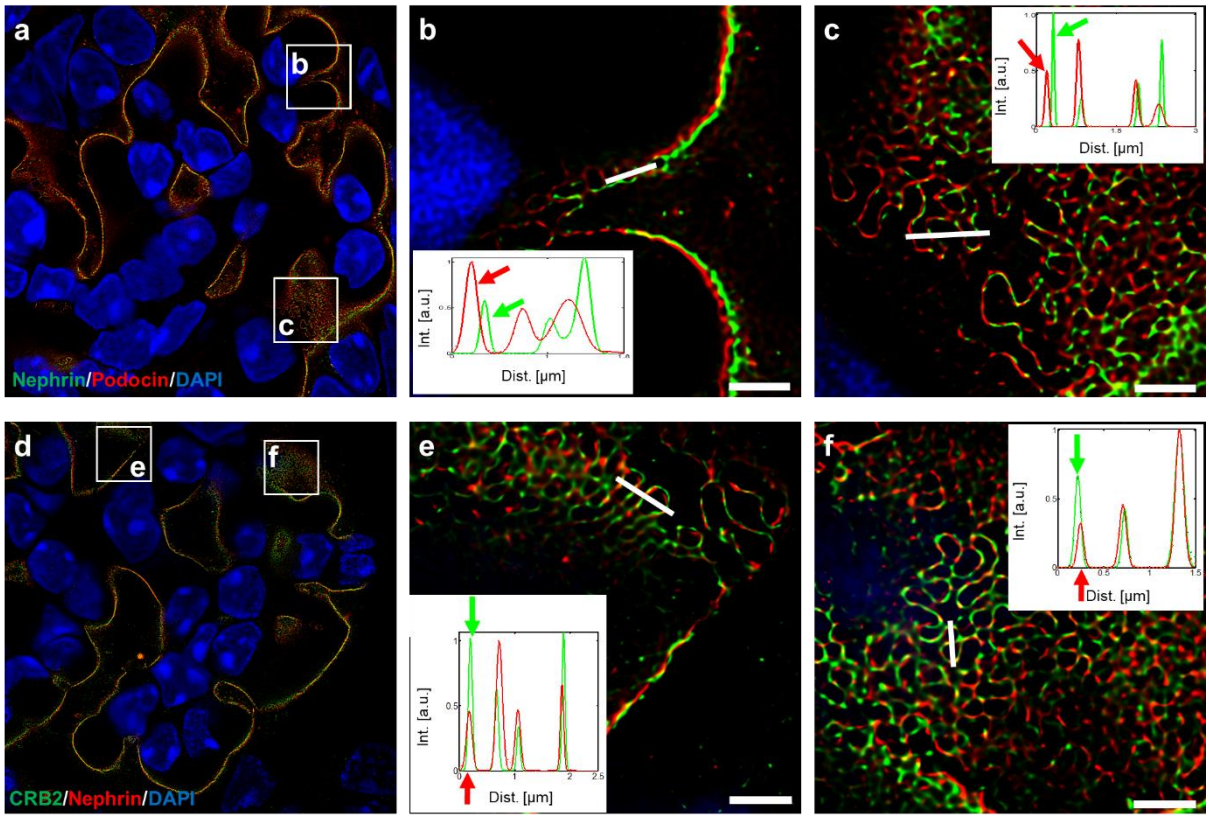

Figure 11: Expanded 100µm WT-mouse kidney slices.
(a-c) Kidney slices immuno-stained for nephrin using rabbit anti-mouse primary and AlexaFluor-488 conjugated goat anti-rabbit secondary antibody. Podocin was stained using rabbit anti-mouse primary and AlexaFluor 647 conjugated goat anti-rabbit antibodies. **(d-f)** Kidney slices immuno-stained for CRB2 using an in-house rabbit anti-mouse primary and AlexaFluor-488 conjugated goat anti-rabbit secondary antibody. Nephrin was stained using guinea pig anti-mouse primary and AlexaFluor 647 conjugated goat anti-guinea pig secondary antibodies. **(a, d)** Representative overview of the immuno-stained WT-mouse kidney slice **(b, c)** Zoomed-in views from **(a)** with line profiles to compare nephrin-podocin co-localization; and **(e, f)** Zoomed-in views from **(d)** with line profiles to compare CRB2-Nephrin co-localization. Scale bars: 2 µm. [96]

4.3. Sub-cellular localization of different CRBs variants

Building upon the knowledge gained from protein localization experiments within murine kidney, the next step was to understand how CRBs isoforms behave at the cellular level. For this purpose, conditionally immortalized human AB8/13 podocyte cell lines stably expressing GFP-tagged CRB2, CRB3A and its mutated versions were created [110]. Briefly, these cells were conditionally immortalized via a stable retroviral transduction of the Simian virus SV40 large T gene antigen making them highly temperature sensitive. This means that only cultivation at the “permissive” temperature of 33°C allows for cellular proliferation. Switching the cells to “non-permissive” temperatures of 37°C leads to cell cycle arrest followed by morphological changes and transcriptional upregulation of proteins characteristic of differentiated *in vivo* podocytes. Transcriptomic analysis of cells grown at permissive temperatures revealed almost negligible levels of endogenous CRB2 expression. Endogenous CRB3A, on the

other hand continues to be marginally expressed within these podocytes [96]. However, CRB3A was undetectable at the proteomic level. These cells, therefore, have the potential to mimic the different stages of podocyte maturation during embryogenesis and act as a valuable tool to study slit diaphragm protein dynamics *in vitro* [110,130,131].

In order to enable an in-depth analysis of the CRBs isoforms at the cellular level, GFP tagged-protein fusion constructs were synthesized to transduce immortalized podocytes using either lentiviral/doxycycline-dependent or retroviral/constitutive vectors. Two control cell lines were additionally prepared that constitutively expressed either a fusion protein harboring two copies of the red fluorescent protein mCherry named, mCherryx2 or a prenylation motif, CAAX; linked with the blue fluorescent protein named, BFP_CAAX. The mCherryx2 cells represents a cell line expressing unbound free floating fluorescent protein whereas the BFP_CAAX cells express fluorescent proteins that only get localized within overlapping regions of two contacting cells. Utilizing these cell lines, we could quantitatively compare the localization of either WT or mutant versions of CRBs proteins within different cellular compartments. Intensity distribution within cells expressing these constructs were acquired under homogenous acquisition parameters as 16-bit Z-stack images (Figure 12-Figure 16). Maximum intensity projections (MIPs) generated from each Z stack for the different cell lines were then subsequently analyzed.

For each cell line MIP, a line profile was drawn such that the ends of the line spanned through the middle of the cell with the ends crossing overlapping cell membranes (Figure 12-Figure 15). These line plots help to validate the distribution of protein localization across the cell. Additionally, three circular 2 µm ROIs were positioned within the overlapping (OM) and free plasma membrane (PM) regions of the cell in order to assess protein localization within different cellular compartments. The ratio between the mean intensity values obtained from the OM and PM ROIs were, thus drawn as box plots (Figure 16).

We first compared the two control cell lines, namely, mCherryx2 and BFP_CAAX. Since the mCherryx2 cell line only harbors two copies of the fluorescent tag without any protein specificity, the signal intensity as expected could be seen as spread unevenly throughout the cell (Figure 12a). The orthogonal YZ-projection along with the line plot also highlight this random distribution. Additionally, in certain cells we could

also identify protein clumps occurring either near the endoplasmic reticulum (ER) or within random cell locations. Due to this unspecific protein distribution, the intensity box plots from different cell types shown in Figure 16 were therefore, normalized using this cell line.

In contrast to the mCherryx2 cells, the BFP_CAAX cells (Figure 12b), show very clearly a distinct localization of the signal within cell-cell contacts. Using a line plot, we can see signal peaks that are representative of positions where one cell membrane comes into contact with another cell membrane marked by the dotted lines within the plot. The line plot additionally shows certain regions highlighting signal accumulation within membrane vesicles that are marked by yellow arrowheads. Upon comparing protein localization within different regions for the two control cell lines, the box plots demonstrate an almost two-fold increase in signal accumulation within the overlapping regions for the BFP_CAAX cells (Figure 16). Following this, results obtained for CRBs isoforms and/or its mutants are shown in the following sub-sections.

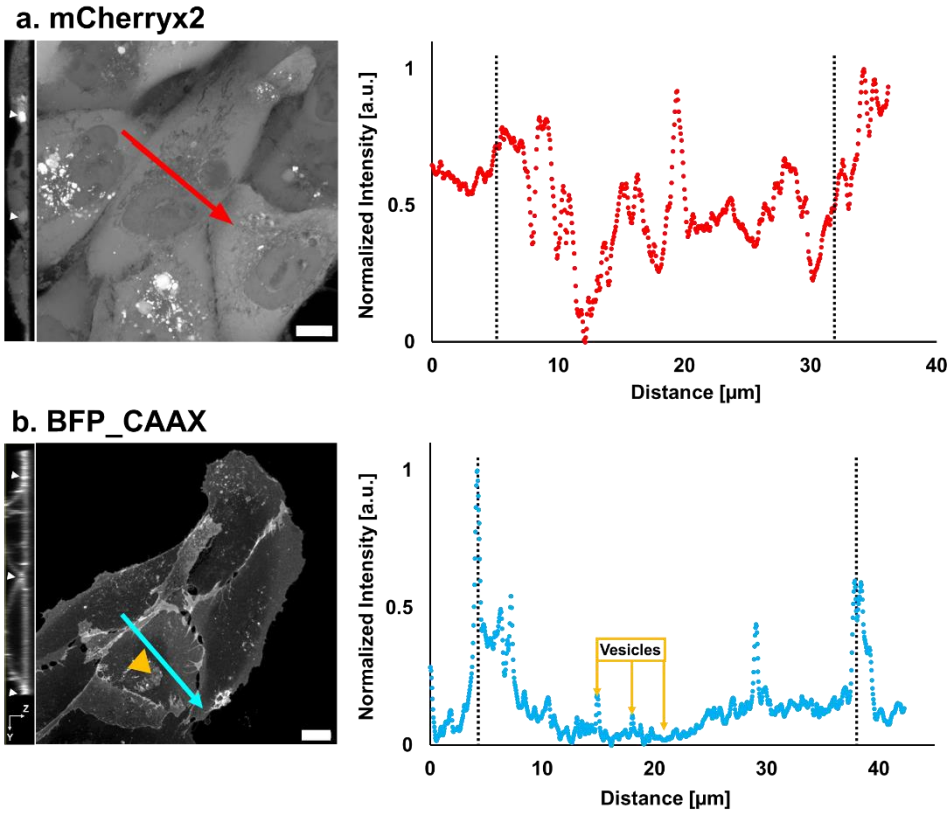

Figure 12: Sub-cellular protein localization within control cell lines.
(a) mCherryx2; and **(b)** BFP_CAAX cell lines. **Left:** Representative Z-stack maximum intensity projection along with a line profile. The YZ-orthogonal view was generated from the center of the shown line profile. White arrowheads: Protein accumulation sites; Red arrowheads: ER stress; Yellow arrowheads: Vesicles; and Orange arrowheads: Finger-like pattern. **Right:** Distance versus normalized intensity plot shown for the drawn line profile. Dotted lines represent cellular edges where two cells membranes overlap. All images were acquired with a 40X water immersion objective; NA 1.2 on Zeiss LSM 880 with Airyscan detector. Scale bar: 10 µm.

4.3.1. Comparing CRB2 vs. CRB3A vs. CRB3A-Basic

Subsequently, similar to the BFP_CAAX cell line, cells expressing either CRB2, CRB3A or CRB3A-Basic were evaluated and compared. Looking at the line plot in Figure 13a, we observed an uneven signal distribution within the CRB3A-Basic cells. Although, there was clearly a high amount of signal accumulation in the overlapping membranes. Smaller protein rich lipid vesicles spread unevenly throughout the cell; marked by yellow arrowheads within the MIPs and line plots, could also be easily identified. As highlighted, these vesicles could be seen not just within the cell but were also present within overlapping cell membranes. On the other hand, Figure 13b shows CRB3A forming massive protein aggregates around the ER and within the cell. Protein aggregates around the ER were indicative of ER stress and were marked by red arrowheads within the MIPs and line plots.

In contrast to CRB3A and CRB3A-Basic, CRB2 expressing cells (Figure 13 c, d) showed a very distinct protein distribution pattern. There were also cells that exhibited protein clusters near the ER, however, the signal could mostly be localized within the cell-cell membrane overlaps. This effect could also be observed from the OM: PM signal intensity ratio (Figure 16). CRB2-WT expressing cells showed the highest signal intensity ratio. Interestingly, drawing a line profile across these membrane overlaps, demarcates distinct regions within the overlaps that contain protein clusters of higher expression versus regions of lower expression resembling an almost “finger-like” pattern (Figure 13c; arrowheads). These regions were shown as orange arrowheads within the MIPs and line plots. From the YZ orthogonal projections, it can be clearly seen, that the protein aggregates within the membrane overlaps were not distributed homogenously. The asymmetric distribution of CRB2 as protein aggregates in overlapping membranes substantiates our hypothesis that the proteins’ random distribution might somehow be linked with its mechanism of action at the molecular level.

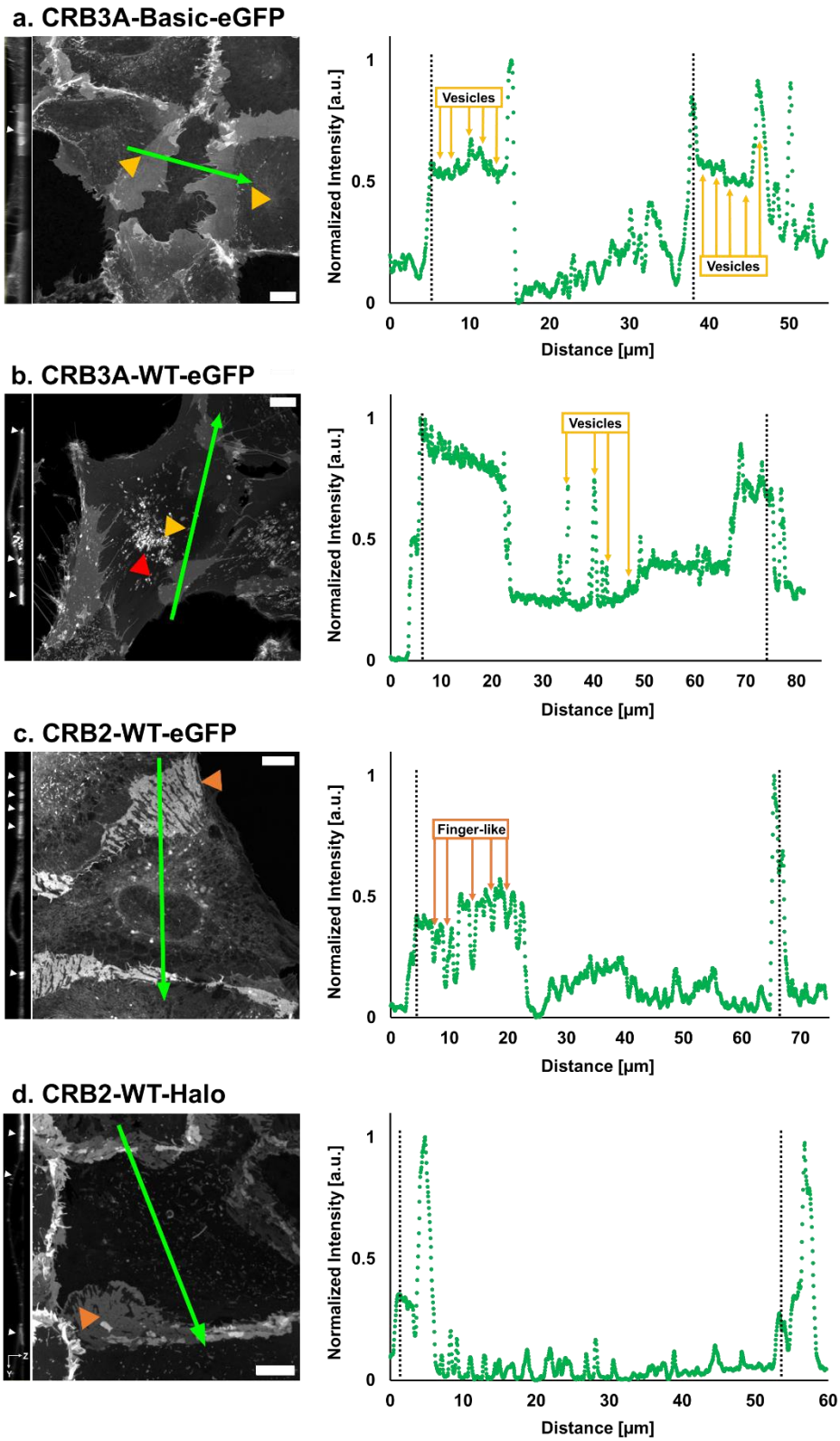

Figure 13: Sub-cellular protein localization within CRBs isoforms.

(a) CRB3A-Basic-eGFP, **(b)** CRB3A-WT-eGFP, **(c)** CRB2-WT-eGFP; and **(d)** CRB2-WT-Halo cell lines. **Left:** Maximum intensity projection of a representative Z-stack along with a line profile. The YZ-orthogonal view was generated from the center of the shown line profile. White arrowheads: Protein accumulation sites; Red arrowheads: ER stress; Yellow arrowheads: Protein enriched intracellular vesicles; and Orange arrowheads: Finger-like interdigitation pattern. **Right:** Distance versus normalized intensity plot shown for the drawn line profile. Dotted lines represent cellular edges where two cells membranes overlap. All images were acquired with a 40X water immersion objective; NA 1.2 on Zeiss LSM 880 with Airyscan detector. Scale bar: 10 µm.

4.3.2. CRB2 deletion mutants

Subsequently, to further investigate our hypothesis and to elucidate CRB2s' functioning mechanism, specific regions within the protein were deleted. These deletion mutants were constructed as GFP-tagged fusion constructs and expressed stably within AB8/13 podocytes to visualize their cellular distribution. Broadly categorized, these mutations were either within the extra- or intra-cellular domains of CRB2.

4.3.2.1. CRB2 ICD mutants

Firstly, the entire intra-cellular region harboring the two cytoskeleton interacting domains was removed by placing a pre-mature stop codon after the transmembrane segment via site-directed mutagenesis (CRB2-ΔIntra, Figure 14d). As can be clearly seen, the eGFP signal for CRB2-ΔIntra was purely localized within the cytoplasmic milieu as confirmed from the line profiles and the box plots (Figure 14 and Figure 16).

Since the CRB2-ΔIntra mutant was unable to co-localize the protein within cell-cell contact junctions, therefore, in a second approach, cells lacking either the PDZ or FERM binding motifs were generated; named, CRB2-ΔPBM and CRB2-ΔFBM, respectively. Surprisingly, as can be seen from Figure 14 (b, c); both these mutants were able to successfully transport the protein towards cell-cell contacts and also displayed a morphology similar to that of CRB2-WT. Within the cellular contacts, just as was the case for the WT, clear regions of protein accumulation could be identified (Figure 16).

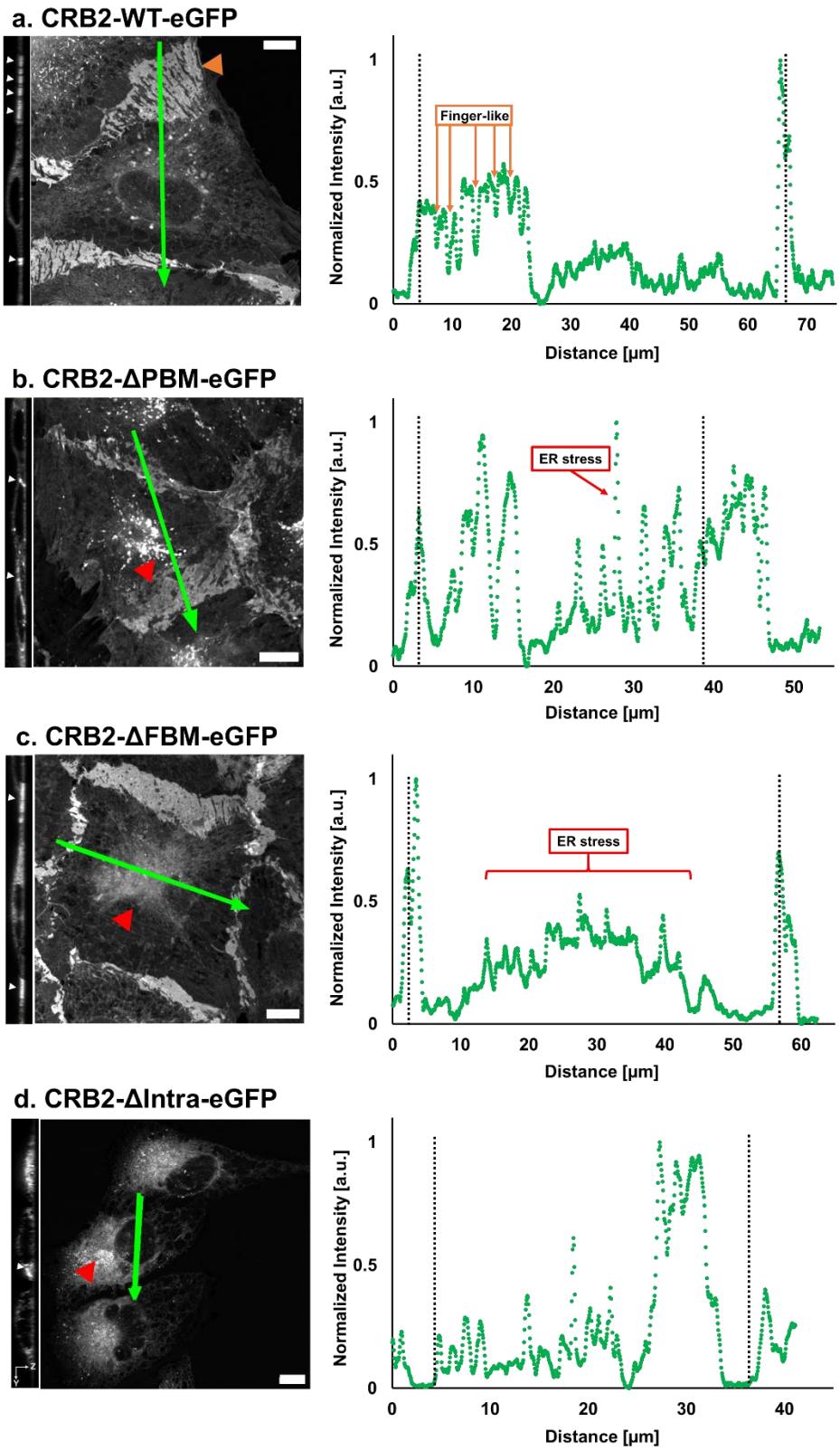

Figure 14: Sub-cellular protein localization within CRB2 ICD mutants.

(a) CRB2-WT-eGFP, **(b)** CRB2-ΔPBM-eGFP, **(c)** CRB2-ΔFBM-eGFP; and **(d)** CRB2-ΔIntra-eGFP cell lines. **Left:** Maximum intensity projection of a representative Z-stack along with a line profile. The YZ-orthogonal view was generated from the center of the shown line profile. White arrowheads: Protein accumulation sites; Red arrowheads: ER stress; Yellow arrowheads: Protein enriched intracellular vesicles; and Orange arrowheads: Finger-like interdigitation pattern. **Right:** Distance versus normalized intensity plot shown for the drawn line profile. Dotted lines represent cellular edges where two cells membranes overlap. All images were acquired with a 40X water immersion objective; NA 1.2 on Zeiss LSM 880 with Airyscan detector. Scale bar: 10 µm.

4.3.2.2. CRB2 ECD mutants

Finally, we generated cell lines that expressed variants of the CRB2 protein lacking either the entire ECD (except for the signal peptide, first and last three membrane-proximal EGF-like domains; named CRB2-ΔExtra) or certain specific regions within the ECD. For the latter, disease-associated point mutation harboring regions from the ECD were chosen as deletion targets [95]. More specifically, three extracellular mutant cell types either missing the 10^{th} EGF-like domain; named CRB2-ΔEGF10, the first two Lam G domains; named CRB2-ΔLG1+2 or all the Lam G domains; named CRB2-ΔLG1-3 were created.

In the case of CRB2-ΔExtra as shown in Figure 15b, we see that much like its WT this mutant still reaches the cellular edges with certain regions within membrane overlaps exhibiting increased eGFP aggregation. We also observed a high amount of eGFP enriched vesicles within the cytoplasmic space and this can be seen clearly as distinct sharp intensity peaks within the line plots. In contrast to this, all the other disease-associated ECD mutant cell lines (results not shown) were unable to co-localize the protein within cell-cell contacts and exhibited a morphology similar to that of the intracellular mutant cell line CRB2-ΔIntra (Figure 14d).

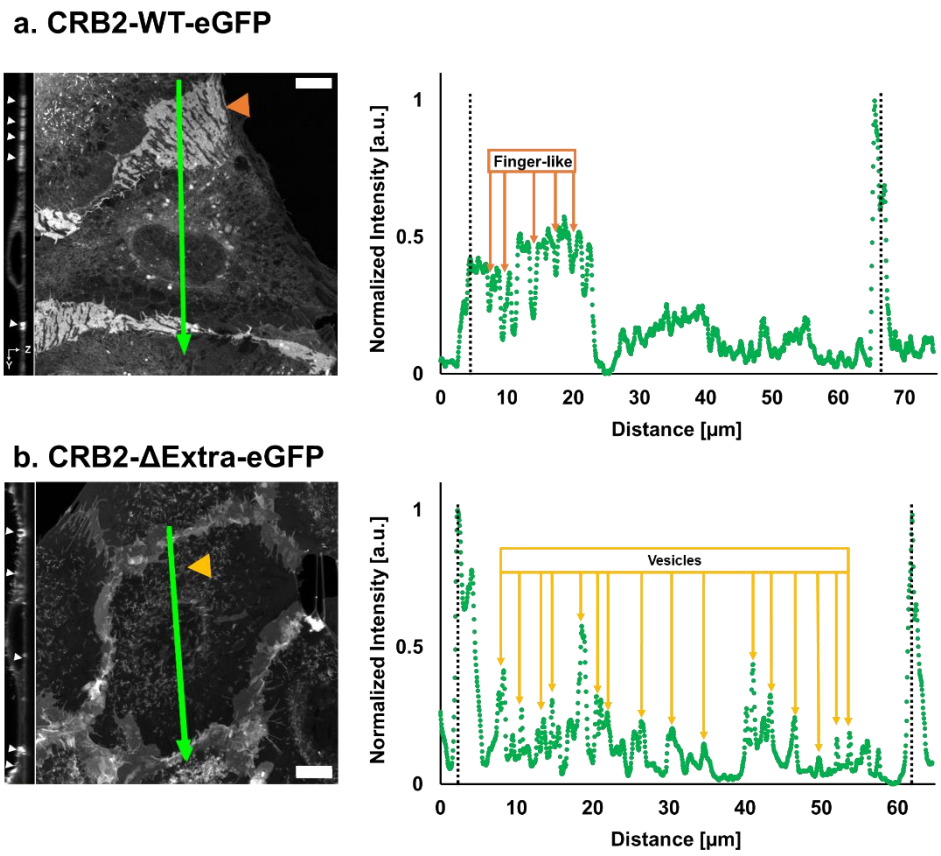

Figure 15: Sub-cellular protein localization within CRB2 ECD mutants.
(a) CRB2-WT-eGFP; and **(b)** CRB2-ΔExtra-eGFP cell lines. **Left:** Maximum intensity projection of a representative Z-stack along with a line profile. The YZ-orthogonal view was generated from the center of the shown line profile. White arrowheads: Protein accumulation sites; Red arrowheads: ER stress; Yellow arrowheads: Protein enriched intracellular vesicles; and Orange arrowheads: Finger-like interdigitation pattern. **Right:** Distance versus normalized intensity plot shown for the drawn line profile. Dotted lines represent cellular edges where two cells membranes overlap. All images were acquired with a 40X water immersion objective; NA 1.2 on Zeiss LSM 880 with Airyscan detector. Scale bar: 10 µm.

In conclusion, the protein localization observations in combination with the conformational information obtained from RoseTTaFold helped us establish essential structure-function relationships. The ability of the CRB2 mutants, namely ΔPBM, ΔFBM and ΔExtra to successfully localize viable protein within cell-cell contacts similar to the WT protein and ΔIntras inability to do so were intriguingly unique and unknown. These findings also highlighted the need to identify particular characteristics such as the proteins' mobility and morphology within said overlapping cellular contacts so as to further elucidate the role of CRB2 within human podocytes.

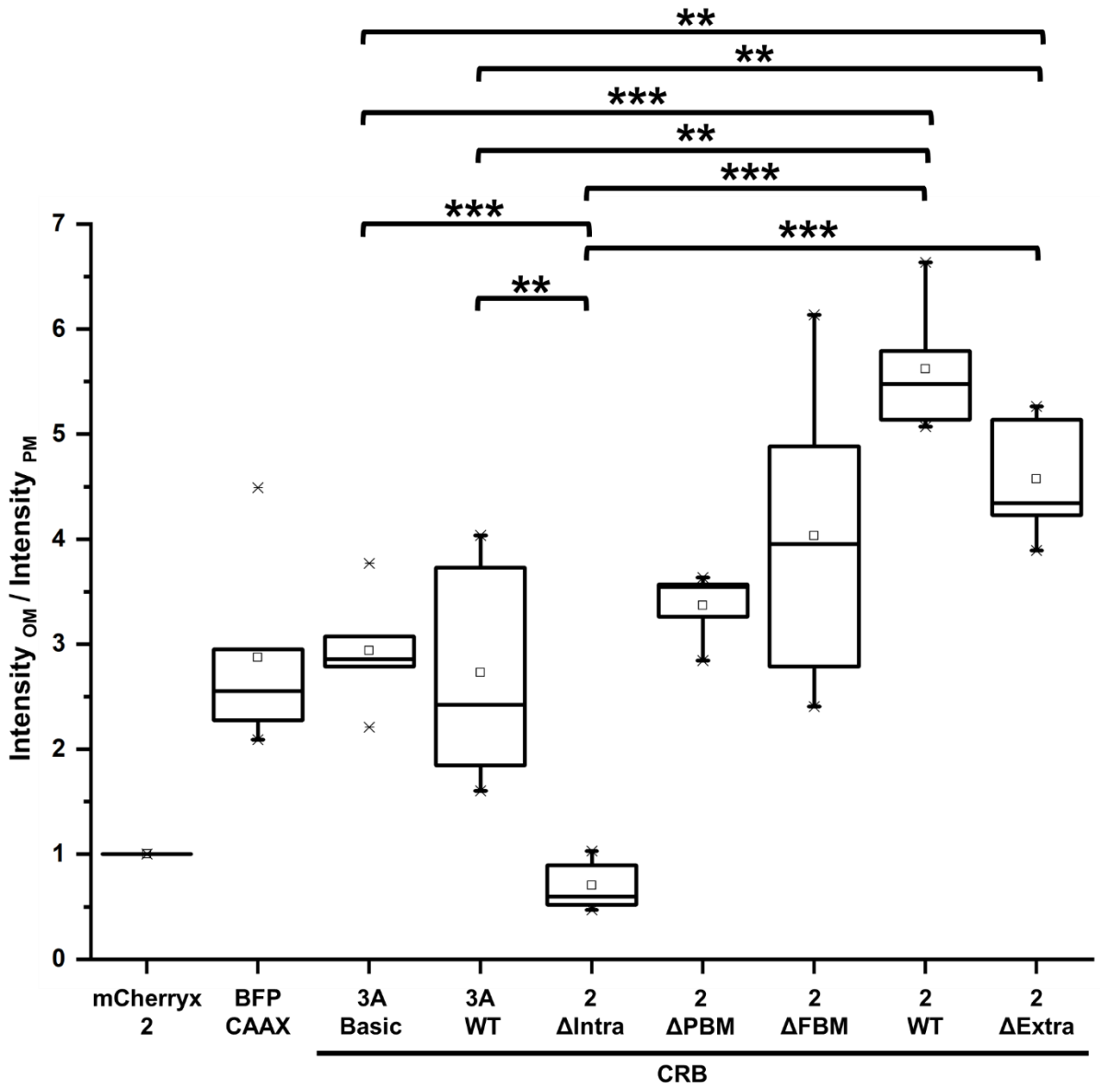

Figure 16: Ratio between OM and PM signal intensities.
Maximum intensity projections generated from Z-stacks for each image were generated and three circular ROIs of 2 µm each were positioned either in the overlapping membrane or the free plasma membrane. mCherryx2 cell line was chosen as the control and all other data points were normalized accordingly. Statistical significance was estimated using an unpaired student T-test. The two-tailed p values were measured for statistical significance. *** p<0.001, ** p<0.005. Number of plate replicates per cell line (N'): 2; and number of cells measured per plate replicate (n): 5.

4.4. Fluorescence Recovery After Photo-bleaching for assessing protein mobility

The conditionally immortalized AB8/13 cell lines mentioned above served as ideal candidates to enable visualization of protein localization at a cellular level. The inclusion of the eGFP-tag further allowed us to perform protein mobility assessments by measuring fluorescence signal recovery post-bleaching within a 2 µm ROI. Moreover, using an inducible promoter we could control protein expression and thus

maintain homogenous experimental parameters. Cell lines expressing mutant isoforms that went into ER stress and were unable to elicit an accumulation within cell-cell contacts were eliminated from this study. Therefore, only CRB2-WT, CRB3A-WT, CRB3A-Basic, CRB2-ΔPBM, CRB2-ΔFBM and CRB2-ΔExtra were further analyzed. Looking at their sub-cellular localization, two distinct regions were identified for analysis. Similar to the way we assessed protein localization, either the bleaching ROI was positioned within the cytoplasmic space called free plasma membrane (PM; Figure 5a) or within regions of overlapping cell-cell membrane contacts (OM; Figure 5c). It should be noted that the OM realistically comprises of an overlap from four lipid bilayers whereas the PM is only one lipid bilayer. Therefore, it can be said that protein recovery observed in the PM for each construct thus provides us with a baseline to compare protein mobility within the OM. Differences observed when comparing mobility of OM versus PM could then essentially be attributed to possible protein-protein interactions occurring within cell-cell contacts. Additionally, in this way if any differences are observed within the proteins' mutants when comparing with the WT, it would highlight the role the different domains perform for normal protein function at a cellular level.

For each measurement, podocytes expressing the respective inducible GFP-fusion constructs were seeded at ~70% confluency and maintained at permissible growing conditions of 33 °C with 5% CO_2. Preliminary testing (results not shown) revealed initiation of protein expression within 12 hours and optimal protein expression post 48 hours of doxycycline-induction. Therefore, samples were always induced 48h prior to taking the measurement with media changes every 24 hours. All FRAP measurements were strictly completed within 6 hours (half of the time needed for initiation of induction) in order to eliminate changes in expression. Thus, the measurement window was tightly maintained from 48-54 hours only. For each ROI (OM or PM) of every CRBs cell line analyzed, three independent samples were measured. From each sample, at least 15 cells were analyzed with a minimum of at least 30 FRAP curves resulting in an average of at least 90 FRAP curves per ROI per CRBs' cell line.

For each ROI from every cell line, the data from the 90 recovery curves was combined to calculate an average FRAP curve. A double-exponential function was fitted to this averaged curve which then provided us with two time constants, T_1 and T_2. Even though we attempted to accurately record protein dynamics at the cellular level, considering the limitations of FRAP, we opted for a more conservative approach. Therefore, we do not measure any diffusion constants from our recorded recovery

data. Instead, we only compare the smaller and faster time constant T_1 along with the proteins' recovering rate (mobile: immobile fraction) so as to semi-quantitatively differentiate between the different CRBs constructs (Table 16).

4.4.1. FRAP measurements of CRBs isoforms

Initial measurements were performed upon the two different Crumbs isoforms, namely, CRB2 and CRB3A. CRB3A-Basic was again chosen as a control cell line as the cells express only a transmembrane protein while lacking the extra- and intra-cellular domains. As can be seen from Table 16, Figure 17 and Figure 20(a, b), measurements performed within the free plasma membrane showed a significantly higher recovery rate of ~90% mobility as compared to the overlapping regions. Analyzing the individual proteins, it can be seen clearly that the CRB3A and CRB3A-Basic proteins are almost identical in their recovering kinetics with the CRB3A eventually being slightly faster with a higher mobile fraction as shown in Table 16 and Figure 20b. On the other hand, CRB2 shows a completely different mobility pattern. It was considerably slower in its recovery in both the free and overlapping membranes. Even with it being slower, it was still able to exhibit a nearly 90% intensity recovery within the free plasma membrane, thereby showing a similar mobile fraction as the CRB3A-Basic. In the overlapping membranes, however, one-third of the protein appears to be immobile with the maximum recovery only reaching ~70%.

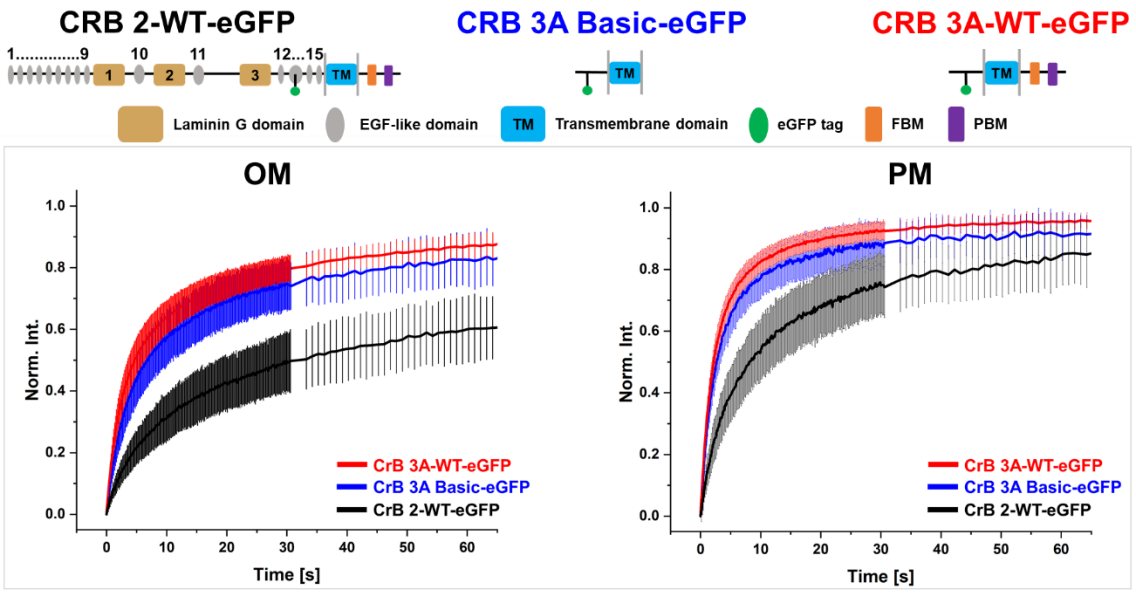

Figure 17: FRAP measurements of CRBs isoforms.
Averaged recovery curves for overlapping membrane (OM) and free plasma membrane (PM) was generated for CRB2-WT-eGFP, CRB3A-Basic-eGFP and CRB3A-WT-eGFP and plotted along with its standard deviation. A double exponential function was fitted to the averaged curves recorded over 2 minutes. Curves only shown up until 1 minute as recovery plateau was attained.

4.4.2. FRAP measurements of CRB mutants

In order to further elucidate the role of each domain upon the proteins' mobility, we also performed FRAP measurements with CRB2 mutants. In particular, they were divided into either intracellular or extracellular mutants. As can be seen from Section 4.3.2, ΔIntra, ΔEGF10, ΔLG1+2 and ΔLG1-3 failed to successfully export the protein within the extra-cellular milieu and exhibited increased levels of ER stress. Therefore, only ΔPBM and ΔFBM from the intracellular mutants and ΔExtra from the extracellular mutants could be selected for mobility measurements.

4.4.2.1. FRAP measurements of CRB2 ICD mutants

First comparing the intracellular mutants with CRB2-WT (Figure 18 and Figure 20 c,d), we observe no significant differences for the ΔFBM mutant within the free and overlapping plasma membranes. The ΔFBM mutant almost exactly mimicks the WTs recovery behaviour. The ΔPBM mutant, on the other hand, exhibits a slightly slower recovery (Figure 18). However, the mutants' overall kinetics represented from the T1 and overall mobile fraction still fell within the same range as that for the WT and was, therefore, not significantly different (Figure 20 c, d).

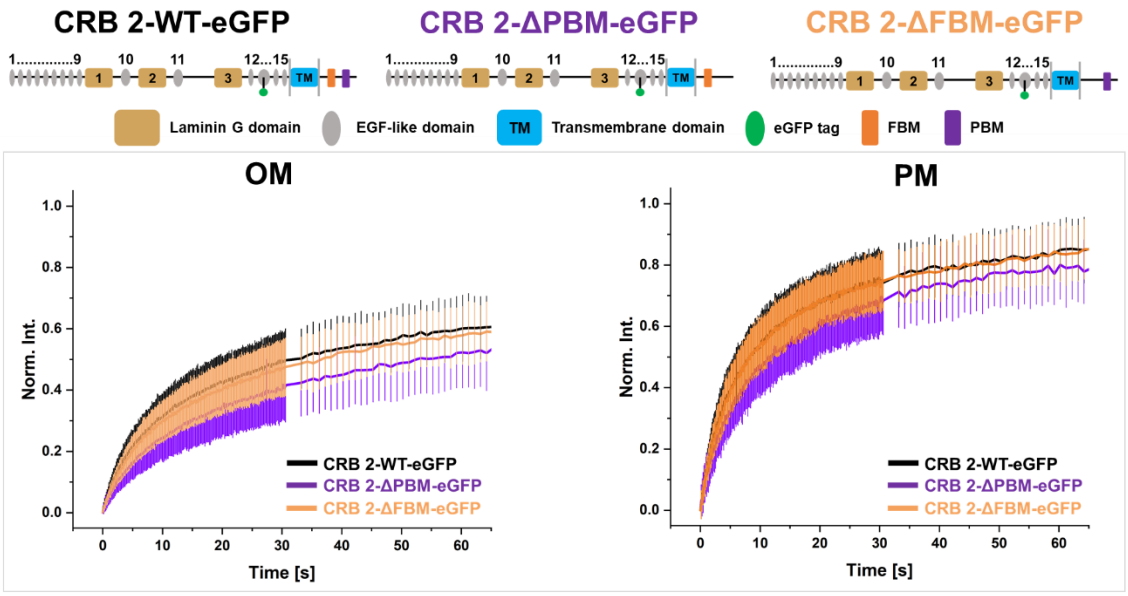

Figure 18: FRAP measurements of CRB2 ICD mutants.
Averaged recovery curves for the two selected ROIs, namely, overlapping membrane (OM) and free plasma membrane (PM) was generated for CRB2-WT-eGFP, CRB2-ΔPBM-eGFP and CRB2-ΔFBM-eGFP and plotted along with its standard deviation. A double exponential function was fitted to the averaged curves recorded over 2 minutes. Curves only shown up until 1 minute as recovery plateau was attained.

4.4.2.2. FRAP measurements of CRB2 ECD mutant

The extracellular mutant; CRB2-ΔExtra, exhibited an altered recovery when compared to the WT. The results in the free plasma membrane were consistent with the other mutants/WT (Figure 19). The protein showed a mobile fraction of ~90% with a relatively fast T1 (Table 16 and Figure 20 e, f). In the overlapping membranes of CRB2-ΔExtra, the value of T1 was similar to the T1 obtained for the free plasma membrane of CRB2-WT. The recovery itself, however, had two very distinctly different populations. One population exhibited a higher mobile fraction of almost 85-90% similar to that of the free plasma membrane. A second more immobile population could also be detected which exhibited a maximum recovery of only 40%, which was significantly lower than the WT within the same region (Figure 19 and Figure 20f).

In another attempt, we specifically characterized this dual behaviour by repeating the measurements. After completion, the measurements were then manually sorted into two different population categories based on their recovering kinetics. It should be noted that ROI selection was completely unbiased during the measurements since there were no morphological traits that could be identified that would provide hints as to which of the two populations (high or low mobile fraction) were being selected (Figure 19 (OM) and Figure 20f). It was only after the measurements were completed

that the data could be pooled into different populations based on their final recovery. Finally, the results from the second round of measurements provided greater insights into the dual nature of this proteins recovery behaviour, thereby highlighting protein accumulation plaques harboring either free floating proteins or entangled dysfunctional protein aggregates.

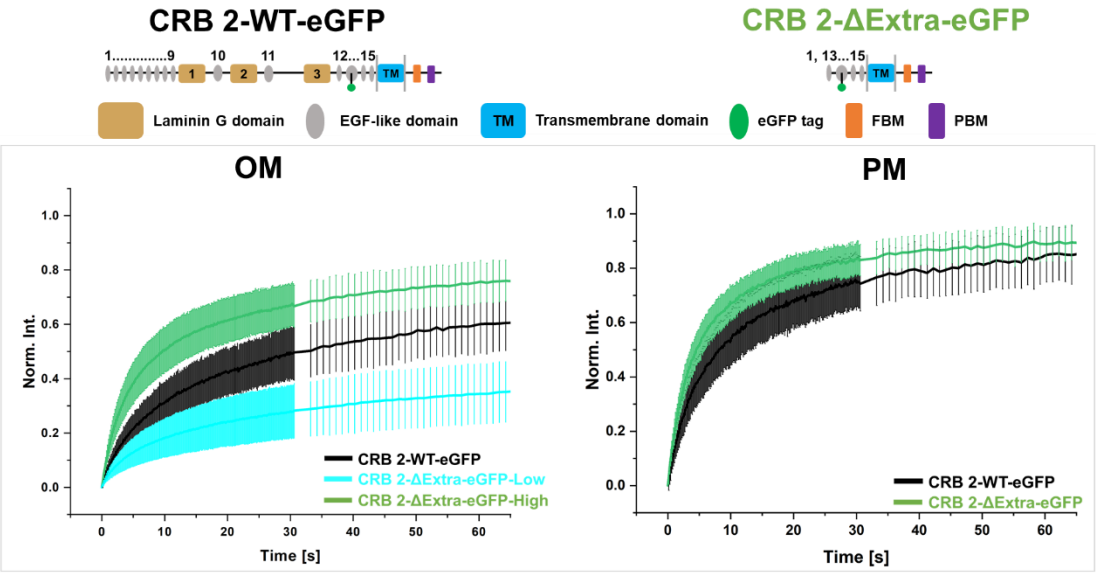

Figure 19: FRAP measurements of CRB2 ECD mutants.
Averaged recovery curves for the two selected ROIs, namely, overlapping membrane (OM) and free plasma membrane (PM) was generated for CRB2-WT-eGFP and CRB2-ΔExtra-eGFP and plotted along with its standard deviation. A double exponential function was fitted to the averaged curves recorded over 2 minutes. Curves only shown up until 1 minute as recovery plateau was attained.

Table 16: FRAP measurements.
Time constants T_1 and T_2 from the bi-exponential FRAP fits and the respective mobile fractions obtained for all CRB2, CRB3 and CRB mutant proteins tested. ±SEM

	Free Plasma membrane (PM)			***Overlapping membrane (OM)***		
Protein	**T_1 [s]**	**T_2 [s]**	**Mobile fraction**	**T_1 [s]**	**T_2 [s]**	**Mobile fraction**
CRB2-WT	4.2±0.4	32.7±3.2	0.91	5.6±0.42	55.6±5.9	0.74
CRB2-ΔPBM	4.1±0.3	36.0±3.4	0.87	5.9±0.4	70.3±5.6	0.70
CRB2-ΔFBM	4.4±0.2	37.2±3.0	0.90	5.8±0.4	64.0±4.8	0.75
CRB2-ΔExtra	2.9±0.07	25.7±1.4	0.93	4.2±0.2	51.0±8.0	0.63
CRB3A-WT	2.1±0.04	15.1±0.5	0.97	2.8±0.07	25.4±2.7	0.91
CRB3A-Basic	2.3±0.06	25.4±2.7	0.94	3.2±0.12	31.7±6.0	0.89

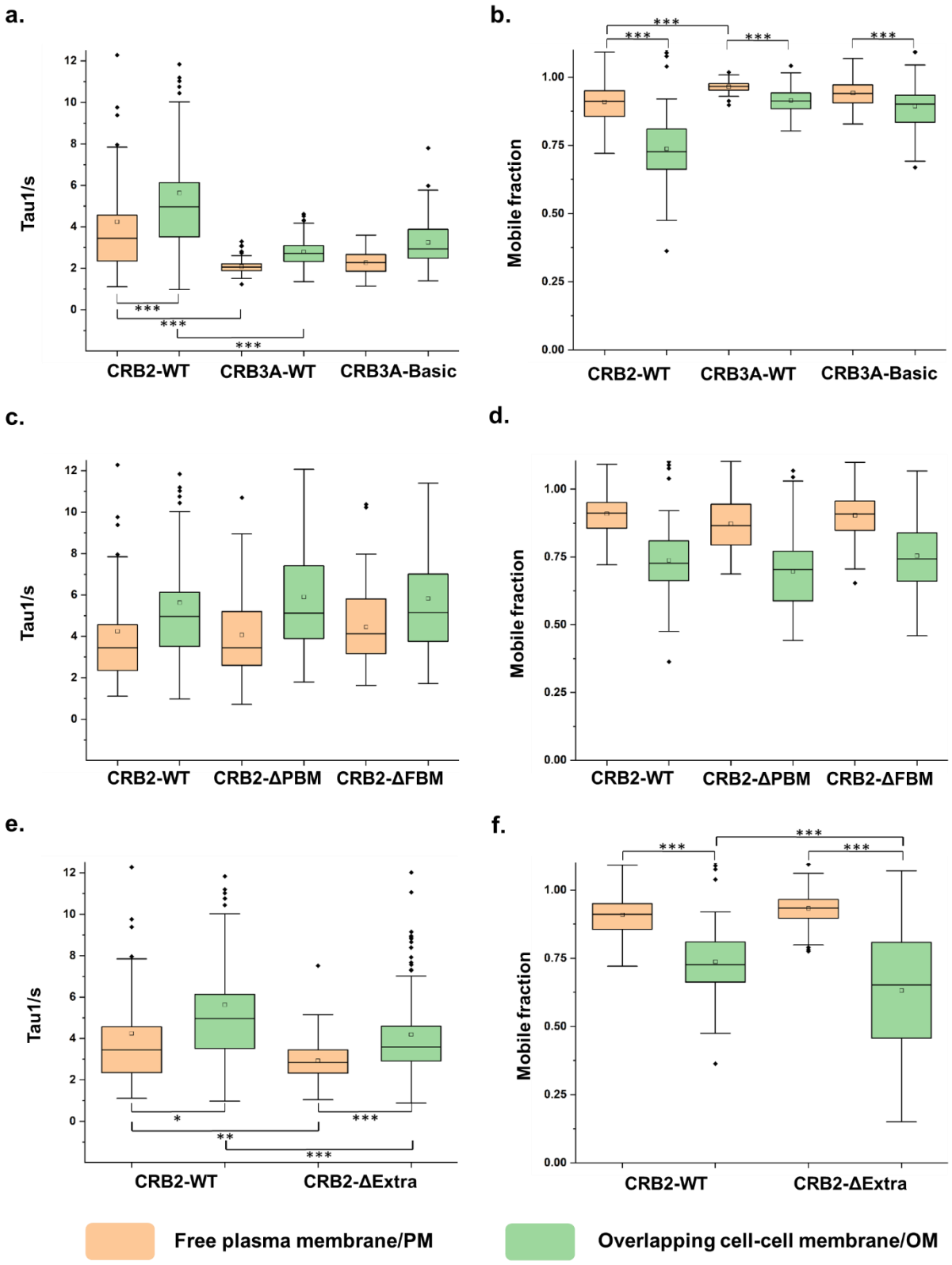

Figure 20: Comparison between recovery time constant Tau 1 versus mobile fraction.
(a, c, e) Plot for time constant T1 and **(b, d, f)** Plot for maximum recovery obtained/mobile fraction for different CRBs-eGFP constructs within the OM ROI and PM ROI. All measurements were fitted to a bi-exponential curve. Curves that exceeded beyond the pre-bleach intensity were manually removed. Individual T1 and mobile fraction from each curve was represented as a box plot and tested for significance using a two-way ANOVA test (*** - p<0.001, ** - p<0.005, * - p<0.01). **(a, b)** Comparison between CRB2-WT, CRB3A-WT and CRB3A-Basic. **(c, d)** Comparison between CRB2-WT and its intracellular mutants, namely CRB2-ΔPBM and CRB2-ΔFBM. **(e, f)** Comparison between CRB2-WT and its extracellular mutant, namely CRB2-ΔExtra.

4.5. Real-time visualization of podocyte co-cultures

The presence of distinct finger-like interdigitating patterns observed within the membrane overlaps of CRB2 expressing podocytes along with FRAP measurements highlighting a slower protein turnover cycle clearly hint towards a system that is governed by ECD specific protein-protein interactions. In order to further investigate the proteins' cytology and to ascertain its binding morphology in greater detail we first aimed to visualize these interactions via live-cell imaging.

Utilizing the CRBs constructs mentioned in Section 4.3, specific cell lines were co-cultured together and visualized for nearly 30 hours. Exactly the same number of cells from each cell type were co-cultured together and cellular density was controlled such that plates would attain ~70-90% confluency during the measurement window. Cells were maintained at 33°C and 5% CO_2 throughout the measurement. In order to maintain the same optical slice the Definite Focus stabilizer (Zeiss®) was utilized. After measurement, time-lapse videos were processed using FiJi. Regions/time points that lost focus due to temperature fluctuations were unfortunately lost and ultimately trimmed out.

4.5.1. Visualizing CRB2 vs. CRB3A-Basic expressing podocytes

Firstly, we examined the differences exhibited by podocytes expressing either the complete CRB2 protein or CRB3A-Basic mutant when co-cultured with mCherryx2 expressing AB8/13 podocytes. In post-processing, the mCherryx2 cell line was grayed out and the eGFP tagged cells were shown using the fire lookup table so as to generate a temporal heat map of protein accumulation (Figure 21).

Visualizing these cells using live cell imaging emphasizes their extremely mobile nature. These cells express the ability to constantly re-organize their plasma membrane while producing thin fiber-like 'Microvilli' as protrusions that enables them to scan their immediate environment (Figure 21, green arrows). These projections are also heavily enriched with the CRBs protein. Figure 21 highlights such an example. It shows that irrespective of the CRBs isoform being expressed, the cells are continuously trying to assess their ambient neighbors and thereby mobilize to reach favorable positions based on their adjacent environmental interactions. However, there

appears to be some disparity in the stability of certain cell-cell interactions that are isoform dependent.

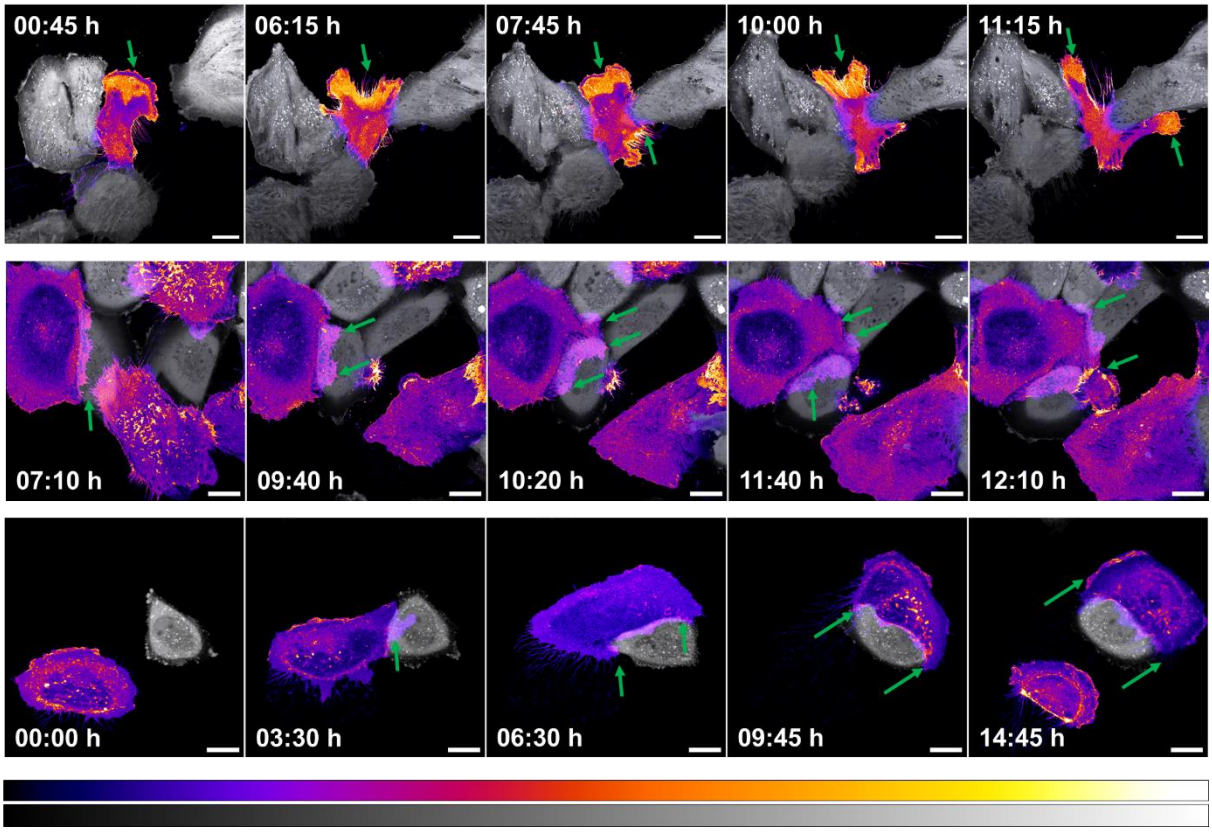

Figure 21: Time-lapse video montages showing different co-cultured cell lines.
mCherryx2 cell line was greyed out whereas the eGFP tagged cells were re-represented using the Fire lookup table in FiJi to compare protein localization. **Top and middle:** CRB2-WT-eGFP and mCherryx2; and **Bottom:** CRB3A-Basic-eGFP and mCherryx2 co-cultures. All images were acquired with a 40X water immersion objective; NA 1.2 on Zeiss LSM 880. Scale bars: 20 µm.

Cellular proximity appears to initiate CRBs protein recruitment towards the site of contact. During this scanning process, where opposing microvilli from two different cells come close, presence of the CRB2 isoform helps to govern cellular attachment or exclusion from site when compared with the CRB3A-Basic. Figure 22 (Top montage panel), highlights one such screening process. Initially at the onset of the time-lapse, we can visualize a stable interaction between two cells positively expressing CRB2 highlighted by green square brackets. This phenomenon was observed quite frequently in the case of CRB2 that once a membrane edge was attached to another cell, only open edges or cell fronts that were unattached were flexible for additional interactions. As can be seen from Figure 22 (Top montage panel, time point 04:15 h), microvilli towards the free edge of one of these cells are unattached and therefore still scanning. As two CRB2 positive cells approach closer to one another, there seems to

be some sort of membrane re-organization. This is followed by interdigitation highlighting an enrichment of CRB2 within the overlapping region. Ultimately, the interaction was unfavorable and the cells broke away. However, on the other hand, the initial stable interaction remained unhindered throughout the entire measurement window. In contrast to CRB2, cells expressing the CRB3A-Basic mutant were unable to maintain such a stable interaction as can be seen from Figure 22 (Bottom montage panel).

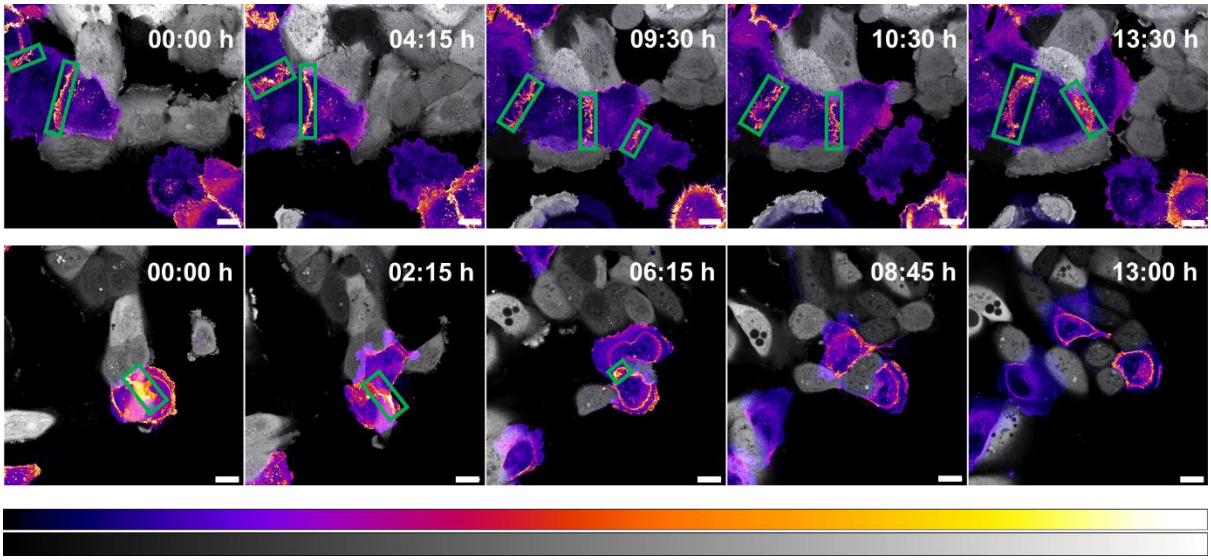

Figure 22: Time-lapse video montages showing stable interaction.
mCherryx2 cell line was greyed out whereas the eGFP tagged cells were re-represented using the Fire lookup table in FiJi to compare protein localization. **Top:** CRB2-WT-eGFP and mCherryx2; and **Bottom:** CRB3A-Basic-eGFP and mCherryx2 co-cultures. All images were acquired with a 40X water immersion objective; NA 1.2 on Zeiss LSM 880. Scale bars: 20 µm.

Another point of difference between the two isoforms was observed upon visualizing dividing cells. Multiple single cells expressing either CRB2 or CRB3A-Basic were assessed. The representative time-lapse montage results are as shown in Figure 23. After division, CRB2 expressing cells exhibit clear membrane overlaps enriched with CRB2. These overlaps remain stable for hours post-division. On the other hand, cells expressing CRB3A-Basic were unable to maintain these interactions and detach and drift away over time.

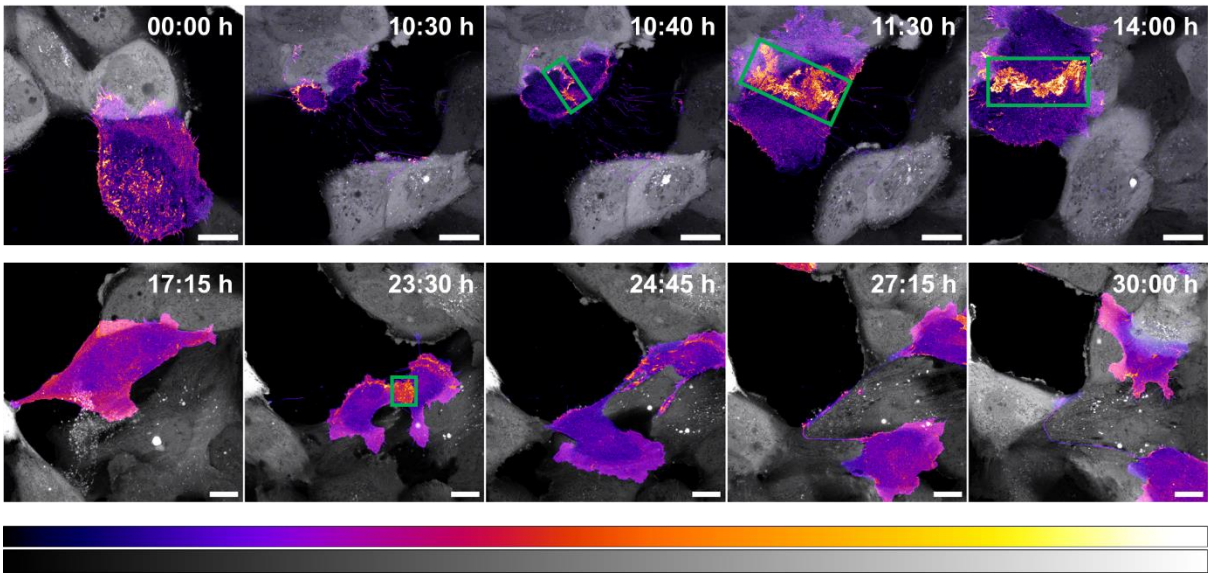

Figure 23: Time-lapse video montages comparing cellular division.
mCherryx2 cell line was greyed out whereas the eGFP tagged cells were re-represented using the Fire lookup table in FiJi to compare protein localization. **Top:** CRB2-WT-eGFP and mCherryx2; and **Bottom:** CRB3A-Basic-eGFP and mCherryx2 co-cultures. All images were acquired with a 40X water immersion objective; NA 1.2 on Zeiss LSM 880. Scale bars: 20 µm.

4.5.2. Visualizing CRB2-CRB2 vs. CRB2-CRB3A expressing podocytes

In order to better visualize CRB2-CRB2 interactions in living cells, two cells expressing CRB2 with different fluorescent tags were co-cultured together, namely, eGFP and HaloTag. Alternatively, as a control measurement, CRB2 cells expressing the HaloTag were also co-cultured with CRB3A-WT-eGFP cells. It should be noted here that the HaloTag was positioned exactly at the same place as the eGFP tag within the CRB2 construct at its 13th EGF-like domain. HaloTag was the preferred choice as it provides for the possibility to utilize a wide range of fluorophores since different synthetic dyes could potentially be coupled to this tag while providing high quantum efficiency. In order to avoid any spectral overlap with the eGFP signal, the Halo tagged cells were stained using 800 nM of the far red dye JF 646. The only disadvantage was that the protein containing the HaloTag was found to get internalized within the cell after 12 hours of staining which, therefore limited our measurement window (Figure 24 and Figure 25).

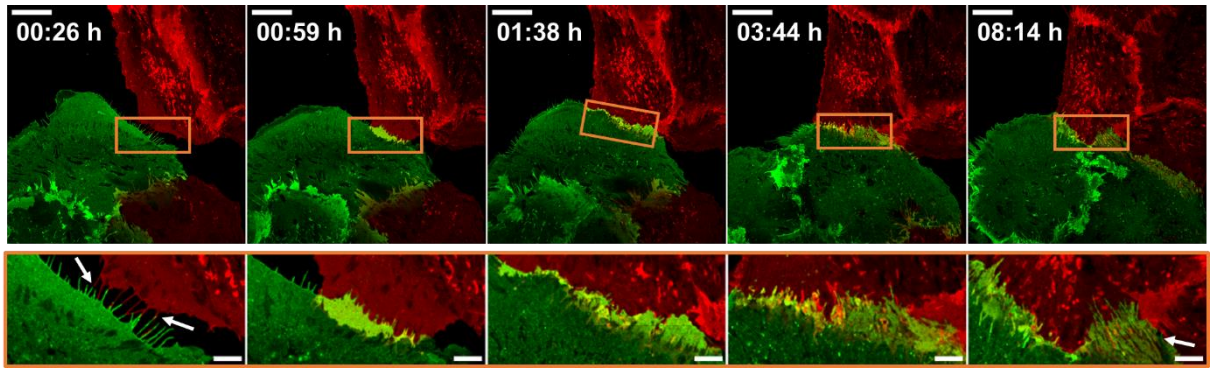

Figure 24: CRB2-WT-eGFP and CRB2-WT-Halo co-culture time lapse montage.
Scale bars: 20 µm; Zoom-Insets: 5 µm. All images were acquired with a 40X water immersion objective; NA 1.2 on Zeiss LSM 880. HaloTag staining dye: JF 646 ® [800 nM].

As visualized earlier, podocytes are extremely mobile cell types and have the ability to sense their immediate environment using microvilli. These microvillar projections are further enriched with the CRB2 transmembrane protein (Figure 24, zoom-inset, arrows shown at time point: 00:26 h). It seems that solely based upon the protein-protein interactions within opposing microvilli, the cells were able to regulate their cytology. As can be seen from Figure 24, cells expressing differently tagged variants of CRB2 form distinct protein accumulations leading to the formation of dense yellow plaques. On the contrary, these accumulations could also be visualized when CRB2 cells were co-cultured with CRB3A-eGFP cells (Figure 25). Distinct regions could be easily identified that highlight protein accumulation/recruitment near contact sites. However, there were certain morphological differences that could also be observed within these overlapping plaques. Most prominent was the presence of the interdigitating pattern that seems to be iconic for CRB2-CRB2 overlaps but was absent within CRB2-CRB3A overlaps. Additionally, the CRB2-CRB2 plaques as opposed to the CRB2-CRB3A plaques were stable throughout the measurement window which was in concurrence with the results shown in the previous section.

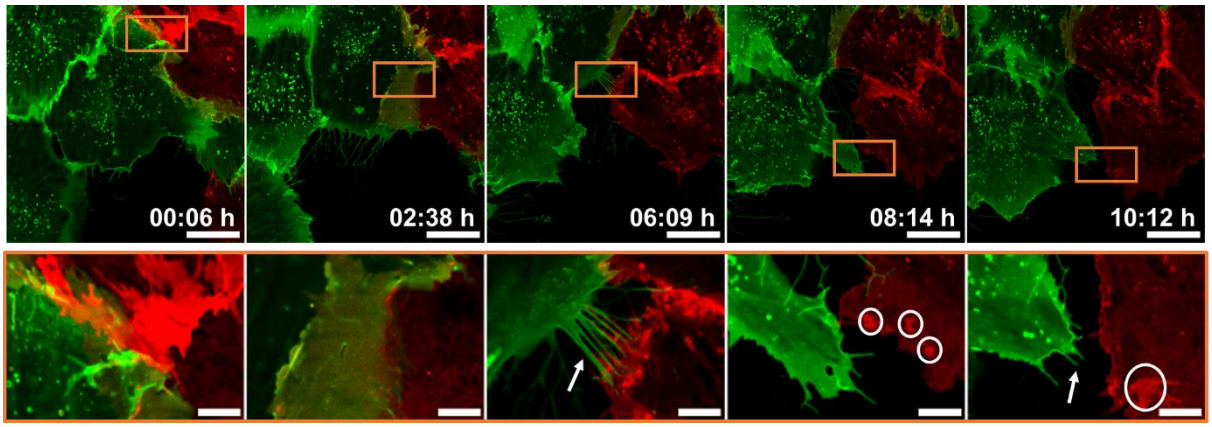

Figure 25: CRB3A-WT-eGFP and CRB2-WT-Halo co-culture time lapse montage.
Scale bars: 20 µm; Zoom-Inset: 5 µm. All images were acquired with a 40X water immersion objective; NA 1.2 on Zeiss LSM 880. HaloTag staining dye: JF 646 ® [800 nM].

4.6. Spatial distribution analysis of different CRBs isoforms

The potential for adjacent podocytes expressing CRB2 to scan their immediate environment along with their ability to maintain stable membrane interactions over extended periods of time highlight the importance of CRB2s' ECD. Developing upon the results from our time-lapse measurements, we decided to expand our observation window from a few hours to a whole week. Cells constitutively expressing eGFP tagged constructs from three CRBs isoforms, namely, CRB2, CRB3A and CRB3A-Basic were separately co-cultured with the mCherryx2 cell line. It was hypothesized that CRB2s long ECD would allow for the cells to remain attached to each other while cells multiply to increase in number. This would therefore, result in CRB2 expressing cells distributing over a broader spatial area while maintaining cell-cell contacts. Cellular density was maintained such that each plate had exactly the same number of cells from each cell type giving an ~20% plate confluency at the beginning of the week. From each of the three sample combinations, six plates were seeded. Three plates were fixed and nuclear stained 24 hours after seeding the cells. This was recorded as Day 1 (Figure 26). The other three plates were allowed to grow for 7 days before being fixed and nuclear stained. This was recorded as Day 7 (Figure 26). The entire plate was then imaged in three channels, namely, eGFP, mCherry and DAPI using a 10x air objective in Tile Scan mode. These measurements were then repeated again in order to attain a triplicate data set.

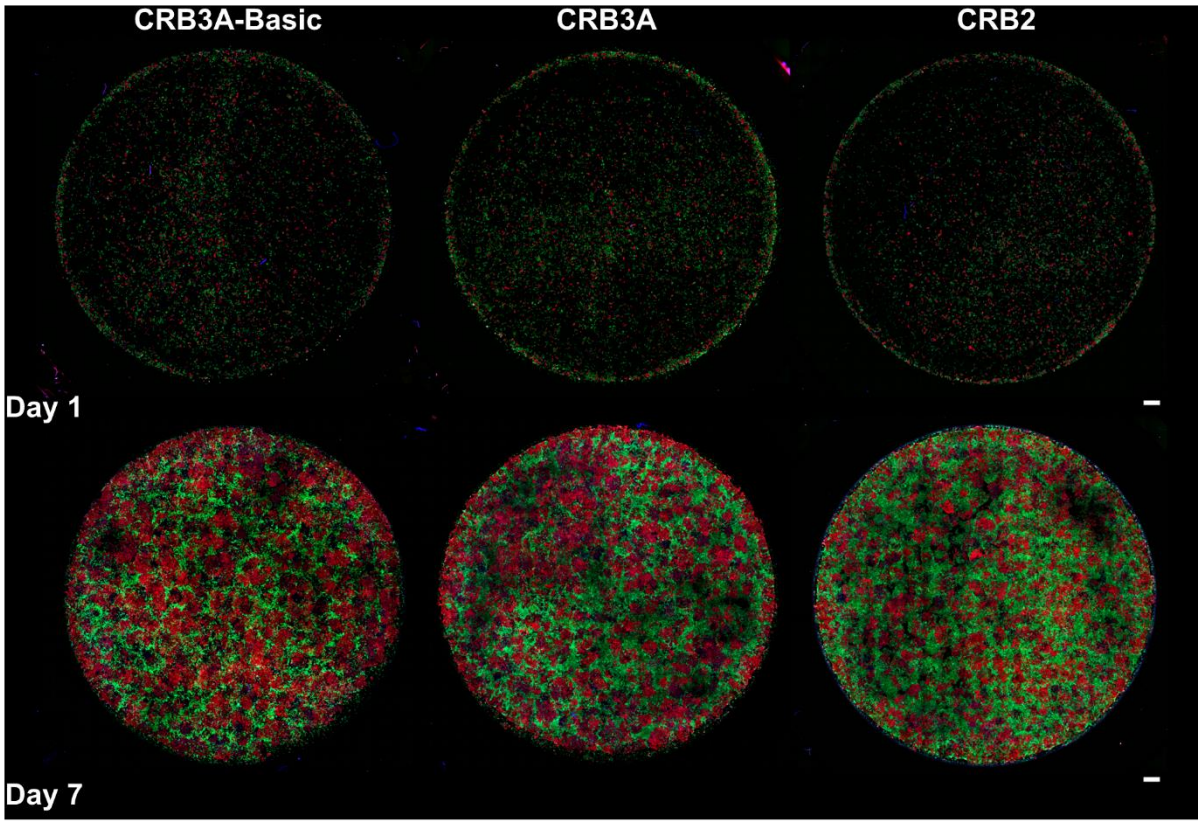

Figure 26: Spatial distribution analysis.
mCherryx2 cells (red) were co-cultured with either CRB3A-Basic-eGFP, CRB3A-WT-eGFP or CRB2-WT-eGFP cells (green). Co-cultured cell plates were fixed and DAPI stained (blue) either after 1 or 7 days of cultivation. Complete Ibidi plates ® were imaged at both time points. All eGFP tagged cell lines are represented as green. All images were acquired with a 10X air immersion objective; NA 0.45 on Zeiss LSM 880. Scale bars: 1 mm. Number of plate replicates per cell line co-culture (N'): 3.

Images recorded from each data set were processed after stitching the tiles such that a binary mask was generated using the GFP channel. CRB3A-Basic served as the negative control cell line for this experiment since it lacks both the extra- and intra-cellular domains. Additionally, time-lapse measurements highlighted this mutants' inability to maintain cell-cell contacts over longer periods of time. Utilizing the generated binary mask, it was possible to determine the cellular density and perimeter for every continuous cell cluster. For each data set, perimeter of the largest cell cluster found within CRB3A-Basic was selected as the minimum threshold (Figure 27f). Only cell accumulations bigger than the threshold, found within CRB2 (Figure 27b) and CRB3A (Figure 27d) cell lines were therefore selected for further analysis.

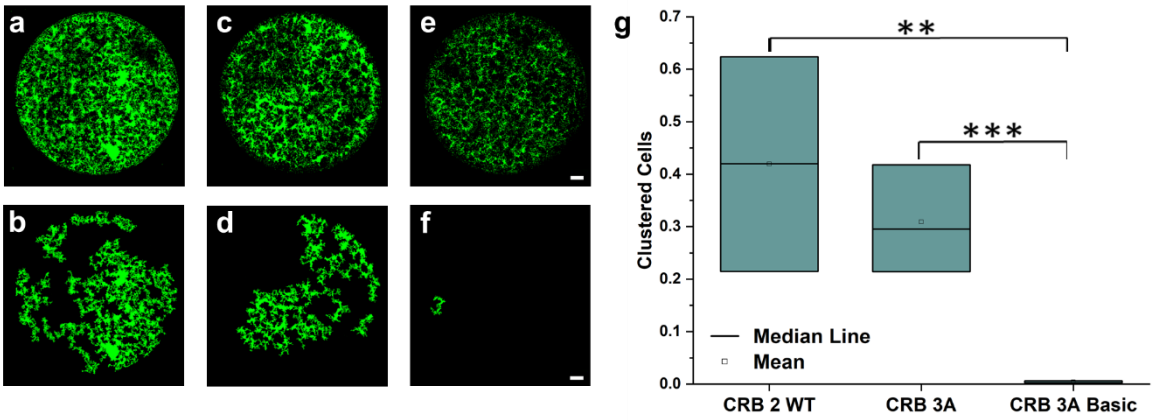

Figure 27: Spatial distribution analysis pipeline.
(a, c, e): Binary image generated from the eGFP channel using manual intensity thresholding. **(b, d and f):** Perimeter of largest identified cluster from CRB3A-Basic-eGFP was used as threshold and smaller clusters were subtracted from the binary image. **(a, b)** CRB2- WT-eGFP; **(c, d)** CRB3A-WT-eGFP; and **(e, f)** CRB3A-Basic-eGFP. **(g)** Graph comparing the clustering ability between CRB2- WT-eGFP, CRB3A-WT-eGFP and CRB3A-Basic-eGFP. Using the binary mask and DAPI channel, the number of cells within the identified clusters versus the total cell count within the complete Ibidi ® dish were quantified. Significance score: *** - p<0.001, ** - p<0.005. All images were acquired with a 10X air immersion objective; NA 0.45 on Zeiss LSM 880. Scale bar: 1 mm. Number of plate replicates per cell line co-culture (N'): 3.

Visualizing the binary image after threshold cluster subtraction, a prominent cell clustering effect was clearly visible for both CRBs isoforms. These observations clearly highlight that cells expressing either CRB2 or CRB3A possess the ability to form and maintain cell-cell contacts over extended periods of time thereby, enabling the formation of an intricate network of conjoined cell cluster mosaics. In order to further quantify this effect, we counted the cellular density within each individual cluster utilizing the DAPI channel. From each data set, the overall cluster density for each isoform was then normalized using the cellular density of the plate and plotted as a box plot showing the mean value along with the deviation from three data sets (Figure 27g). Although both CRB3A also exhibited the ability to form extended networks, it can be seen that this effect was strikingly more noticeable within CRB2 expressing podocytes.

4.7. Investigating the morphology of CRB2-CRB2 interactions

Membrane kinetic measurements along with time-lapse and cell aggregation analysis clearly outlined a crucial role for the ECD of CRB2. The distinct interaction pattern for these proteins within membrane microvilli, however, remains elusive. Drawing from different sources, the homotypic protein-protein interactions have previously been documented to be either present in *Cis* [132,133] or *Trans* [107,134,135] configurations. Therefore, we hypothesized two possible interaction models for the

CRB2 protein within membrane microvilli (Figure 28). Utilizing the ECDs size estimates from RoseTTaFold [109], which were in the range of 40-50 nm and by simply co-culturing cell lines expressing different C-terminally tagged variants of the CRB2 protein, we estimated the inter-fluorophore gap distances between the cells for the two hypothesized models.

As can be seen from Figure 28, for the *Cis* configuration, we expect that CRB2 being expressed within the microvilli of a podocyte could only interact with adjacent CRB2 present within the same microvilli. This would lead to a somewhat stacked protein morphology with an inter-fluorophore gap of ~80-100 nm. On the other hand, in the event of a *Trans* configuration, CRB2 being expressed within the microvilli from one podocyte should be able to interact with CRB2 being expressed within the microvilli from an adjacent podocyte. This configuration, would then provide for an interlocked protein morphology with a reduced inter-fluorophore gap. We hypothesized that only the hinge-like region of the protein was flexible enough to enable such an interaction. Therefore, the final inter-cellular gap within *Trans* acting podocytes would be ~55-75 nm. While we were able to visualize and follow the microvilli using conventional microscopy, it was not possible to resolve the proteins' distribution within these ultra-structures. Subsequently, observing a distance distortion as small as 30 nm between the two possible configurations of the protein would be impossible as was evident from the presence of yellow plaques observed during the time-lapse measurements.

Visualization of protein configuration with sub-50 nm precision necessitates the use of super-resolution microscopic techniques. The Airyscan detector from Zeiss with its unique 32-channel gallium arsenide phosphide photomultiplier tube has been previously shown to provide an ~1.7-fold higher spatial resolution in all three dimensions along with a 4-8 fold increase in signal-to-noise ratio (SNR) [136]. Lateral resolution for this detector reaches ~120 nm when observed with an 1.4 NA objective at an excitation wavelength of 488 nm. This was, however, not sufficient to observe the microvillar architecture. Therefore, to further augment its resolution capabilities, we aimed to combine Airyscan imaging with expansion microscopy. Owing to its enhanced SNR capability, the Airyscan detector could potentially compensate for the reduced fluorophore distribution caused from expansion. Thus, the combination of long-term co-culture cultivation of cells expressing differently tagged CRB2 variants along with expansion microscopy and Airyscan imaging would essentially allow us to visually resolve protein distribution within the podocyte microvilli.

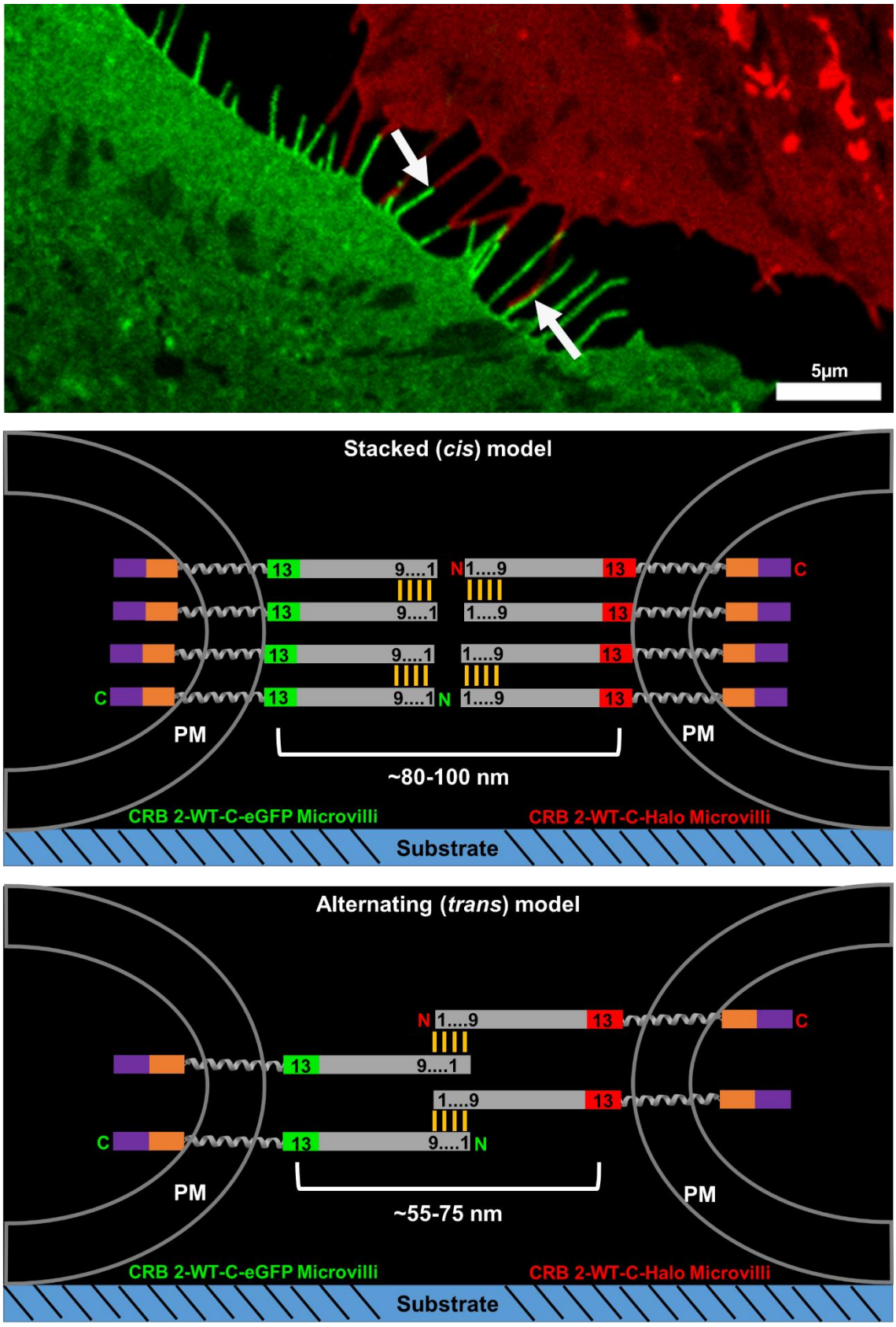

Figure 28: CRB2-CRB2 homotypic interaction models.
Two models as hypothesized from earlier findings are represented. Depending upon protein-protein interactions, fluorophore distribution was imagined to be either stacked or alternating representative of a *cis* or *trans* configuration, respectively. Based upon ECD size estimations from RoseTTaFold [109], the estimated inter-fluorophore distance is shown for each model. Numbers indicate the respective EGF-like domains. CRB2-WT-eGFP (green), CRB2-WT-Halo (red) with their respective distances from the transmembrane domain (blue). All images were acquired with a 40X water immersion objective; NA 1.2 on Zeiss LSM 880. Scale bar: 5 µm. HaloTag staining dye: JF 646 ® [800 nM].

Cells that were constitutively expressing either the CRB2-C-terminal eGFP or CRB2-C-terminal HaloTag construct were co-cultured. Cellular density was maintained such that each coverslip had exactly the same number of cells from each cell type giving an ~20% coverslip confluency. The cells were cultivated for a week to enable formation of membrane overlaps before fixation. Post-fixation labelling was performed for the Halo tagged protein with 200 nM Janelia Fluor ®549 coupled substrate and the eGFP signal was further enhanced using an AlexaFluor 488 coupled nanobody before the samples were processed for expansion microscopy (Section 2.4.3). Entire cell Z-stacks were imaged to enable accurate 3-D visualization of the proteins' distribution with microvillar ultra-structures. The experiment was repeated twice to attain a triplicate data set.

It should be noted that even though the same cellular regions could not be visualized before and after expansion, the results shown are representative of the interactions visualized from the triplicate data set. As can be seen from the representative Figure 29 (a, b), we were able to clearly visualize the microvilli expressing the different C-terminally tagged constructs using a high NA objective and Airyscan imaging. As expected, pre-expansion resolution was insufficient to delineate protein distribution within individual microvilli (Figure 29b; arrow). Membrane overlaps showcased protein accumulations that could only be observed as yellow plaques. When visualizing these overlapping cell-cell contacts post-expansion as shown in Figure 29 (c, d), the intrinsic microvillar protein distribution could be easily imaged. Distance measurements between the two fluorophores could be performed, however, the results were inhomogeneous. Certain regions demonstrated distances larger than 100 nm between the fluorophores whereas some spots exhibited fluorophore co-localization. The protein distribution within the microvilli itself was also neither stacked nor alternating, as previously hypothesized. Additionally, no distinct distribution pattern could be identified since fluorophore distribution was non-equidistant, thereby making it difficult to conclusively predict the exact morphology of CRB2-CRB2 interactions.

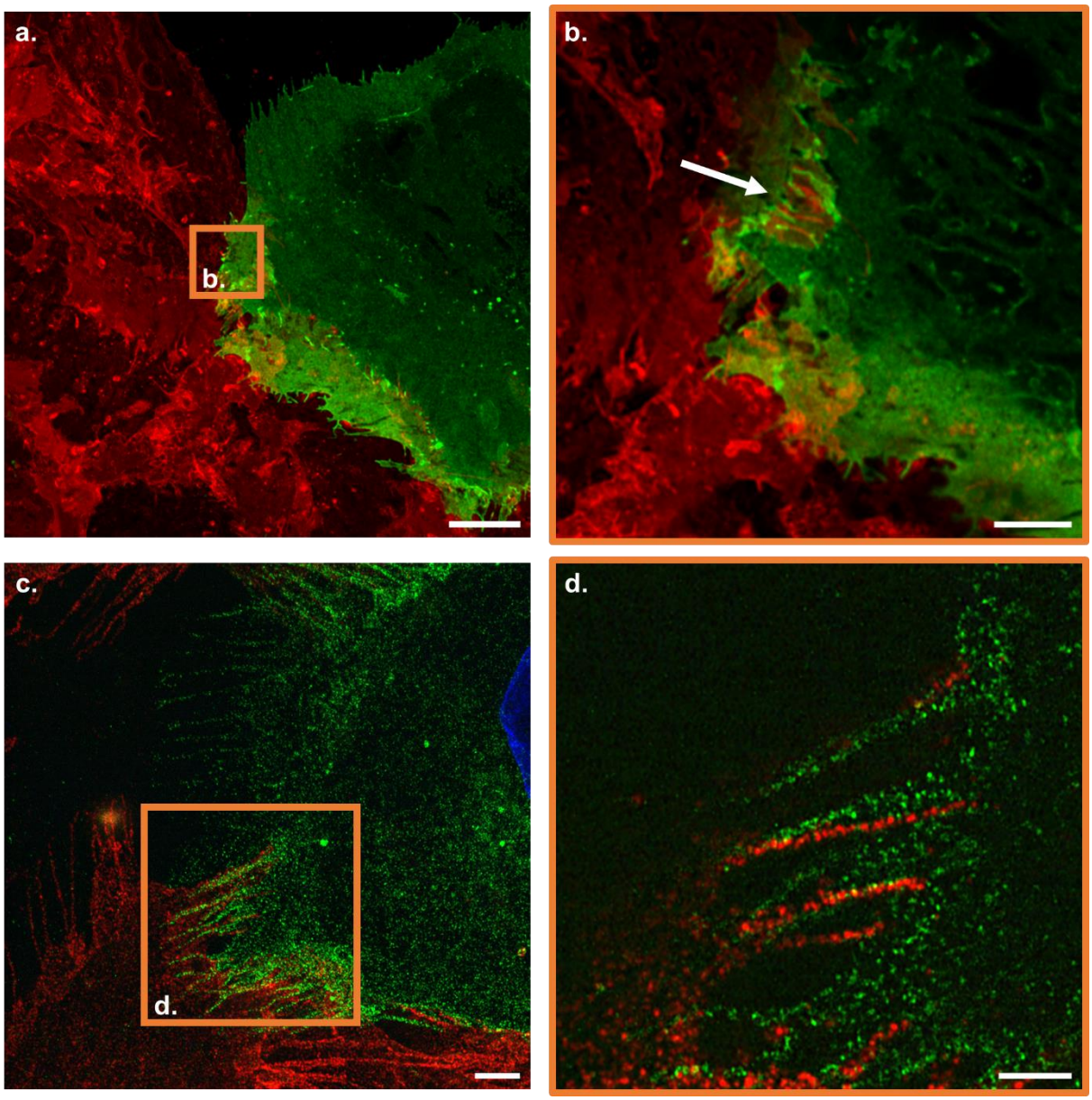

Figure 29: Expansion microscopy of CRB2-WT-eGFP and CRB2-WT-Halo co-cultures.
eGFP (green) and HaloTag (red) expressing CRB2-WT cells were co-cultured and cultivated for one week before fixation. After fixation, they were DAPI stained (blue) and expanded. **(a, b)** Pre-expansion images were acquired with a 63X oil immersion objective; NA 1.4; and **(c, d)** Post-expansion images were acquired with a 40X water immersion objective; NA 1.1 on Zeiss LSM 880 with Airyscan detector. Expansion factor was estimated to be ~3.3x using DAPI. **(a, c)** Overview image; and **(b, d)** Zoom-ins. Scale bars: 10 µm; Zoom: 5 µm. HaloTag staining dye: JF 549 ® [200 nM].

4.8. CRB2 controls cellular focal adhesion via vinculin

The results obtained thus far all aimed to indicate towards a *trans* mode of action for CRB2 (Figure 28). Unfortunately, the combination of high-resolution imaging and expansion microscopy proved ineffective in resolving CRB2-CRB2 interactions inside cell-cell contacts as expected. As a consequence, we applied a different approach known as traction force microscopy in order to understand the interactions between these cell-cell contacts. Our collaboration with the Institute of Biological Information Processing in Jülich headed by Prof. Dr. Rudolf Merkel helped us gain insights into the

force fields generated by these cells and whether they were CRB2-dependent or not. For these experiments, either single cells or two cells showing considerable membrane overlaps were selected. Two interacting cells will be referred to as a cell duplet for ease of understanding. A summary of the obtained traction force results along with their interpretation will be discussed in the subsequent chapter.

Based upon the observed cellular-force measurements, Prof. Dr. Rudolf Merkel also recommended to further investigate the interactions between CRB2 and the intracellular focal adhesion marker vinculin. Looking at Section 1.1.2 along with Figure 2, vinculin can be seen to be essential in cementing the podocytes to the GBM by linking the cell to other ECM proteins. Observing vinculin against actin, the initial immunostainings from Jülich showed a clear difference between the number and size of FAs formed between cells expressing CRB2 as opposed to the WT podocytes without any construct (results are shown in the subsequent chapter; Figure 32). Building upon these results, we performed similar immunostainings within CRB2-eGFP-WT and CRB3A-eGFP-WT cells as shown in Figure 30. Looking particularly at the overlaid images showing CRB2/CRB3A and vinculin distribution within cell duplets (Figure 30 g, o; white arrows), we observed that vinculin and eGFP signals co-localize in the case for CRB3A-eGFP-WT cells. Contrastingly, in the case of CRB2-eGFP-WT cells, the eGFP signal was excluded from membrane regions enriched in vinculin as highlighted in Figure 30 e-g versus m-o (white arrows) and evident from the line profiles shown in Figure 31 (a-d; red arrows). Utilizing these immunostaining images, a programmed computer software was prepared by our collaboration partners. Taking the vinculin staining as input, the program characterizes focal adhesions on multiple parameters such as number, size and area covered per cell surface. Two of these parameters, namely, number and percentage of coverage per cell surface area for each cell line are as shown in Figure 31 (e, f). It is evident that CRB2-eGFP-WT cells contain significantly lower FA sites than non-transduced AB8/13 podocytes that span a larger area per cell surface and are devoid of CRB2. On the other hand, CRB3A-eGFP-WT cells contain almost similar amounts of FA sites as the non-transduced AB8/13 cells. These FAs were comparable in size and cell coverage percentage to the CRB2-eGFP-WT cells' FAs. However, they are highly enriched with CRB3A.

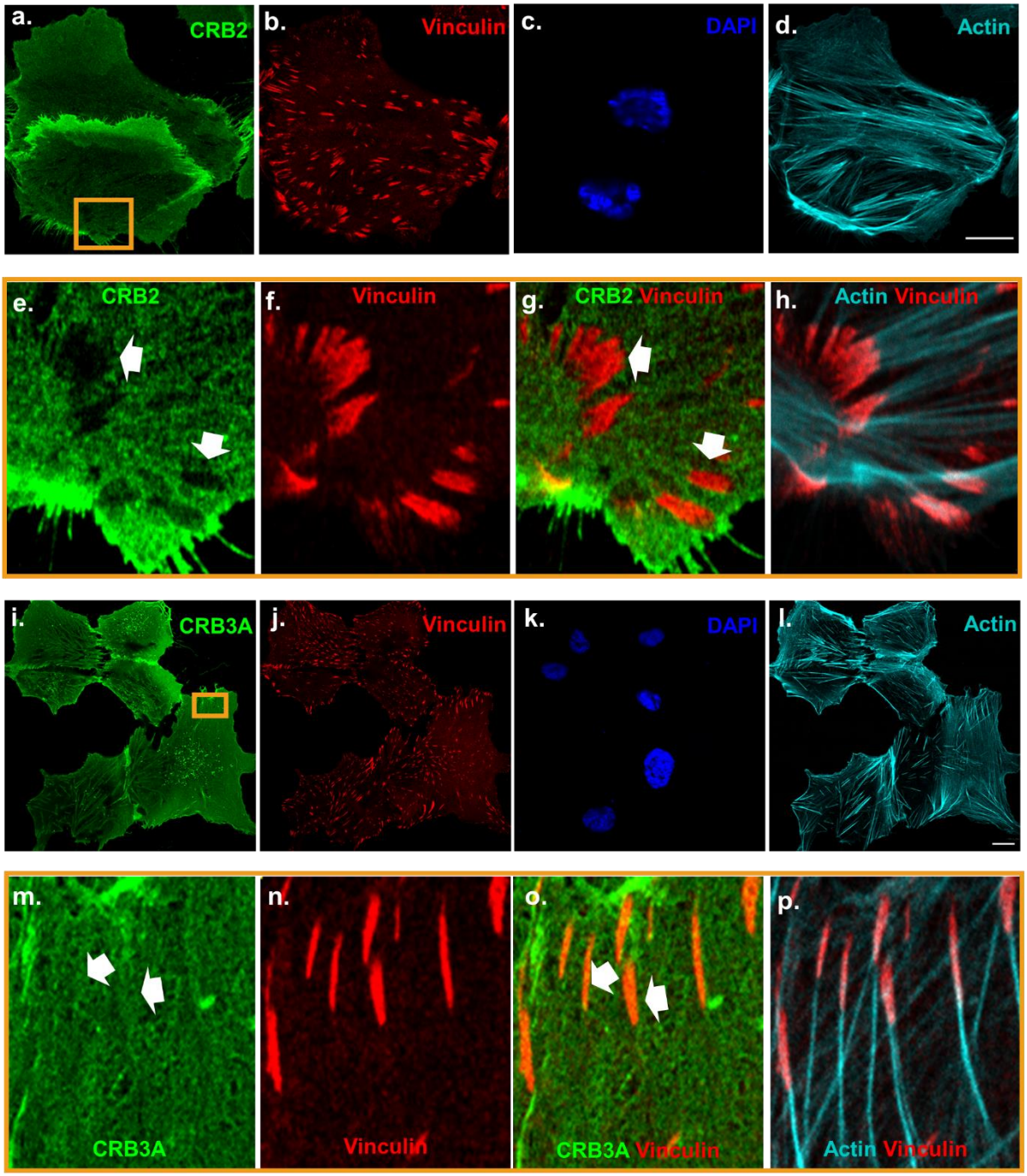

Figure 30: Comparison between CRB2-eGFP-WT and CRB3A-eGFP-WT.
(a-h) CRB2-eGFP-WT and **(i-p)** CRB3A-eGFP-WT were immunostained for vinculin **(b, f, j ,n)**, actin **(d, l)** and DAPI **(c, k)**. **(g, o)** Merged images of CRB2/CRB3A and vinculin. **(h, p)** Merged images of actin and vinculin. **(a-d and i-l)** Overview images. **(e-h and m-p)** Zoom-in views from regions highlighted in **(a)** and **(i)**. All images were acquired at 16-bit rate with a 63X oil immersion objective; NA 1.4 on Zeiss LSM 880. **(d, l)** Scale bars: 20µm.

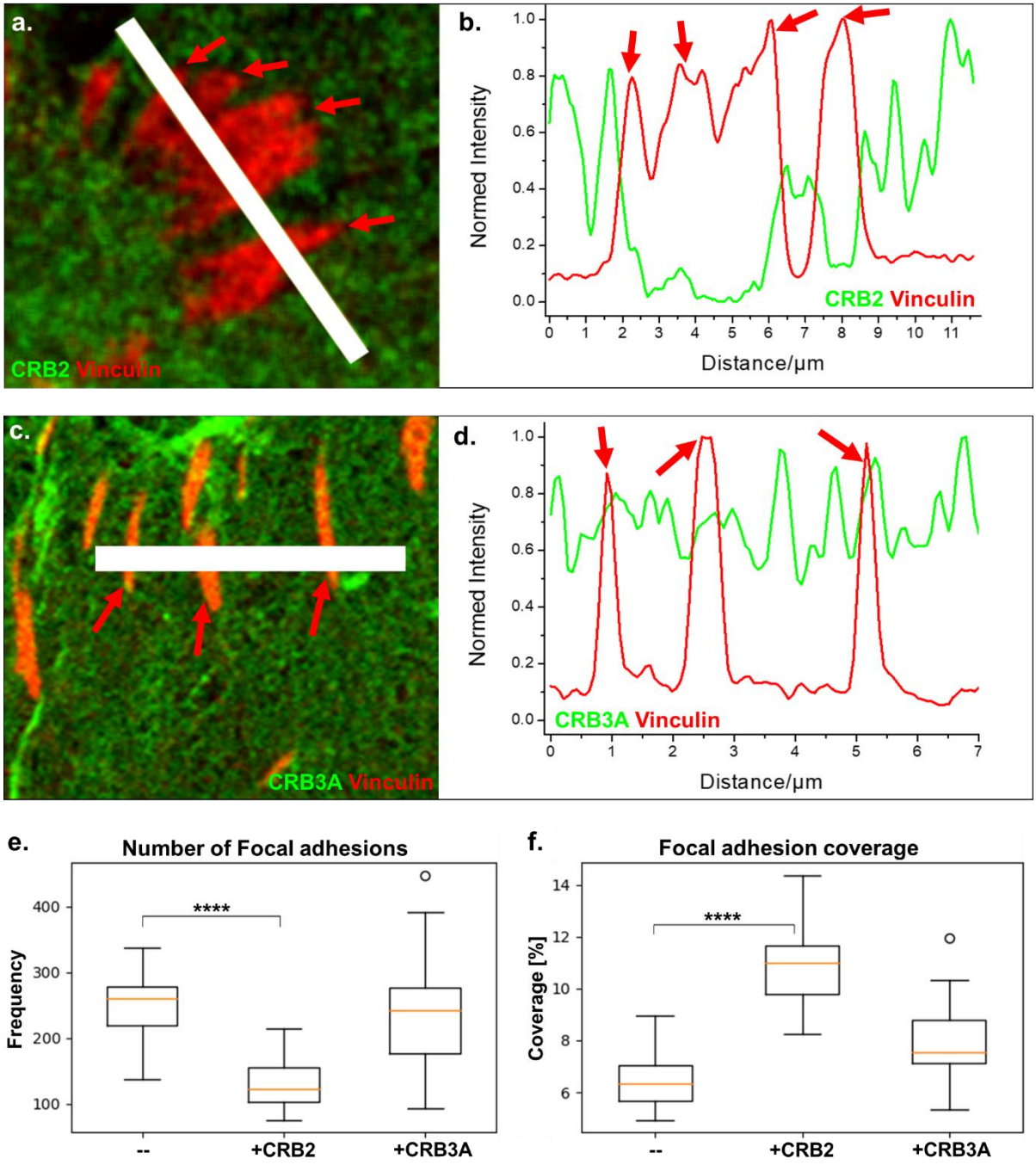

Figure 31: Analysis of CRB2/CRB3A versus vinculin.
(a, c) Cropped zoom-in views as shown in Figure 30 **(g, o)** with line profiles. **(b, d)** Line profiles comparing CRB2/CRB3A versus vinculin distribution. Vinculin staining was chosen as the criteria for identifying focal adhesion sites. **(e)** Box-plots comparing the average number of focal adhesion sites observed within cell-cell duplets. **(f)** Box-plots comparing the average area covered by focal adhesion sites within cell-cell duplets. --: Non-transduced AB8/13 cells; +CRB2: AB8/13 cells constitutively expressing CRB2-eGFP-WT; +CRB3A: AB8/13 cells constitutively expressing CRB3A-eGFP-WT; Significance scores based on student t-test: ****-p<0.001, ***-p<0.005, **-p<0.01. All images were acquired at 16-bit rate with a 63X oil immersion objective; NA 1.4 on Zeiss LSM 880. Number of plate replicates (N'): 3; and Number of cells measured per plate replicate (n): 10. (Data courtesy: Sven Gerlach [unpublished data])

5. Discussion

The human kidney is a very specialized organ with a highly dedicated architecture that supports its functionality [1]. Its formation involves a complex interplay of different proteins at crucial time points during embryogenesis that help orchestrate the establishment of a functional glomerular filtration barrier [88,89,92,131]. In vertebrates, the outer most layer within this filtration barrier is formed from podocytes. During development, polarity determinants and more predominantly the epithelial apico-basal polarity markers expressed within these podocytes potentially help guide cell migration, allowing for the establishment of tertiary foot processes that interdigitate leading to the formation of the highly organized slit diaphragm [1]. This thesis predominantly aims at unravelling the molecular functions of the polarity marker CRB2 with emphasis on the role of its long ECD.

5.1. Structure of CRB2

CRB2 in its canonical form is a single-pass type I transmembrane protein. Its large ECD possesses 15 EGF-like domains along with three interspersed Lam G domains when compared with CRB3A. The evolutionarily conserved ICD, however, harnesses the FERM and PDZ binding motifs in both isoforms of the protein. The complexity of CRB2s ECD has kept the structure of this protein and thereby, its function elusive. As can be seen from our results obtained from either AlphaFold2 [108] or RoseTTaFold [109], we were able to generate comparative 3-D structural models for the different protein isoforms. AlphaFold2 seemed to produce unreliable results since the algorithm was unable to clearly differentiate between the extra- and intra-cellular segments of the protein.

Modelling problems within AlphaFold2 might be associated with the algorithms architecture. The assignment of atomic co-ordinates in AlphaFold2 occurs instantly after the individual domains are identified using a multiple sequence alignment. Once the co-ordinates are fixed, the program then provides complete rotational freedom to each amino acid within each individual domain. Finally, after testing from multiple iterations, it generates a thermodynamically favorable inter-domain distance map that helps to determine the proteins' final structural conformation. The developers of a competing modelling team, named RoseTTaFold reasoned that this could lead to

possible conformational rigidity. Therefore, they attempted to circumvent this issue. They prepared a similar algorithm that had a parallel feedback loop that enabled cross-communication between the amino acid sequence information, the generated distance maps and 3-D amino acid co-ordinate positions. This would, thus enable a more flexible feedback mechanism which should eventually result in better protein structure prediction. Therefore, we opted to rely more upon on RoseTTaFold rather than AlphaFold2.

A common feature, however, evident from the different modelling algorithms was the prediction for the flexibility of the CRB2 molecule that strongly indicated for an adjustable hinge-like orientation of its large ECD. Looking at its structure (Figure 8a; orange arrow), this hinge-like flexible region of the ECD of CRB2 can be identified between the 7^{th} and 8^{th} EGF-like domain. Interestingly, amongst the 15 EGF-like domains within CRB2s ECD, EGFs- 2, 3, 4, 7 and 8 are known to be calcium binding. Looking closely at its structure, EGF domains typically contain six cysteine residues that are involved in the formation of disulfide bridges. A subset of these domains abundantly found within proteins responsible for numerous cellular processes such as cell growth are also known to be extremely sensitive towards local Ca^{2+} concentrations [137–139]. Ca^{2+} binding to EGF-like domains present within large transmembrane proteins harboring multitudes of these domains has previously been demonstrated to induce conformational changes within subsequently neighboring domains [137,140]. These changes can ultimately contribute towards protein stability that is crucial for normal biological activity [141] via modulation of protein-protein interactions [142–146]. Knowing the concentration of free Ca^{2+} within the extracellular milieu to be ~1.4 mM [147], it could be postulated that the elasticity imparted to the ECD of CRB2 might be derived from the presence of these five calcium-binding EGF-like domains. Thus, we speculate that these domains are pivotal for CRB2s biological function.

5.2. Localization of CRB2

5.2.1. CRB2 and Nephrin form adjacent clusters within the SD

Podocytes are polarized epithelial cells that envelope capillaries to form the outermost layer of the highly specialized glomerular filtration barrier. Interdigitating membrane protrusions from neighboring podocytes help establish an ~40 nm wide slit diaphragm crucial for healthy renal function [148]. Earlier studies focusing upon kidney

development have tried to characterize the composition of the slit diaphragm. The interplay of multiple proteins either alone or in complex within this 40 nm gap have posed a major challenge. For instance, the presence of adherens junction proteins such as P-cadherin [43], β-catenin and FAT [149] along with tight junction proteins such as ZO-1 and occludin [56] make it difficult to even classify this junction.

Until recently, only nephrin and Neph1 have been identified as the major components regulating the function of the slit diaphragm [150,46]. CRB2, on the other hand, has only been shown to be localized within the visceral layer of the Bowmans capsule in conjunction with its presence within endothelial cells surrounding the capillaries and squamous epithelium of the parietal layer along with marginal expression within tubular epithelia [92–94]. But, its expression within the SD remains broadly unknown. Therefore, using protein-retention expansion microscopy (Pro-ExM), we visualized CRB2 in murine kidney slices, achieving sub-100 nm resolution [118,96]. Nephrin served as a reference marker. Nephrin is known to localize within the apical domains of the SD while forming homotypic interactions between adjacent foot processes [48,49]. After the expansion protocol was optimized, we were able to successfully visualize the typical loop-like pattern of the SD. Subsequently, we were also able to compare the localization patterns between two interacting SD proteins, namely, nephrin and podocin [50]. Nephrin clusters appeared more apical when compared to podocin as shown in Figure 11 [96], thus confirming our methods precision.

Finally, upon comparing the localization of CRB2 with nephrin within 3-D image stacks of expanded immunostained WT murine glomeruli, we were able to identify them as individual protein clusters located adjacent to each other. The presence of adjacent protein clusters within interdigitating foot processes suggests homotypic CRB2-CRB2 interactions. Similar homotypic interactions have also been known to exist in tandem with nephrin-nephrin interactions within the SD in *Drosophila* [75,107,132]. Our findings, therefore, support for a complex SD architecture requiring both transmembrane proteins nephrin and CRB2. Each of these proteins form stable homotypic interactions through their ~40-50 nm wide ECD to maintain SD integrity.

5.2.2. CRB2 accumulates near membrane edges of adjoining podocytes

Drawing from our findings, we aimed to further characterize the role of CRB2 within podocyte membranes. Subsequent investigations were, therefore, carried out within two-dimensional cell culture systems stably expressing either WT or mutant versions of the protein. Instead of relying on non-podocyte cell lines such as human embryonic kidney (HEK; [151]) or podocytes of non-human origin such as Mardin-Darby canine kidney (MDCK; [152]), we proceeded to use conditionally immortalized human podocytes generated via viral transduction [110]. Maintaining these conditionally immortalized AB8/13 human podocytes at permissive conditions ensured their continuous survival [153].

In order to facilitate live cell measurements, consecutive viral transductions of eGFP tagged versions of CRBs constructs was performed within these podocytes. The constructs can be broadly classified as native WT, ECD or ICD deletion mutants. Native WT constructs were namely, CRB2, CRB3A and the control cell line CRB3A-Basic. The ECD mutants were, namely, CRB2-ΔLG1-2, CRB2-ΔEGF10, CRB2-ΔLG1-3 and CRB2-ΔExtra. Finally, the ICD mutants comprised of CRB2-ΔPBM, CRB2-ΔFBM, and CRB2-ΔIntra. These constructs yielded cells either exhibiting protein expression within the plasma membrane or culminating in ER stress (Figure 13-Figure 15).

In contrast to previous reports highlighting a rather apical localization of CRB2-WT within MDCK cells [92], these de-differentiated AB8/13 cells exhibit peculiar pockets of eGFP-signal accumulation seen predominantly near the lateral edges of adjoining cells. The other native constructs, CRB3A and CRB3A-Basic; along with the ICD mutants CRB2-ΔPBM and CRB2-ΔFBM and the ECD deletion mutant CRB2-ΔExtra displayed a similar cellular phenotype. A comparison of the signal intensity between overlapping membrane edges of adjoining cells to the free plasma membrane (Figure 16), shows that CRB2-WT cells exhibit maximum signal accumulation within overlapping membranes.

On the other hand, cells expressing certain ECD or ICD deletion mutants only resulted in ER stress. This includes ECD mutant constructs that harbor mutations within disease-associated regions of the ECD (Figure 4; [61]), namely, CRB2- ΔLG1-2, ΔEGF10 and ΔLG1-3 and the ICD mutant, CRB2-ΔIntra. The inability of the N-terminal mutants to exhibit normal membrane localization has previously been attributed to

impaired protein folding originating from N-glycosylation defects [92]. However, the ER stress finding for CRB2-ΔIntra, wherein the cells lack both the evolutionarily conserved intracellular domains was serendipitous.

Interestingly, localization of CRB2 within different cellular regions has also been shown to govern specific stages of podocyte maturation. Immunostaining studies within murine developmental kidneys show that premature podocytes purposefully withhold CRB2 within the apical region so as to mediate development of basolateral associations [89]. Post-development, these associations further recruit CRB2, where it gets reposed within cell-cell contacts and helps stabilize cellular topography demarcating the culmination of podocyte maturity [92]. The basolateral localization of our CRB2-WT construct within de-differentiated podocytes, therefore, seems to be representative of a skewed podocyte morphology that could be attributed to the absence of natural neighbors such as mesangial and endothelial cells [154].

Although, the current 2-D cell cultures present certain limitations, they are however, as of this time, the most ideal system to investigate protein-protein interactions within human podocytes. Therefore, simply by choosing cells transduced with CRBs constructs under different plasmid promoters we regulated protein expression to be either constitutive or inducible allowing us to perform long term live-cell and short-term membrane mobility studies, respectively.

5.3. Role of the ECD on CRB2 function

5.3.1. CRBs isoform kinetics define structure-function relationships

The mobility of proteins in cell membranes depends on their interaction partners, which can be localized either outside or inside the membrane. Investigating protein mobility provides information about such interactions and thus about the functionality of the proteins. Combining this with the proteins' structural information helps to further establish essential structure-function associations. FRAP mobility assessments, therefore, were performed with cells expressing inducible CRBs constructs while accounting for certain assumptions as mentioned earlier [119]. Based upon the cellular localization of CRBs proteins, the assessment of membrane mobility using FRAP necessitated the analysis to be conducted within two distinct membrane regions. The protein-dense lateral membrane overlaps were chosen as the first region. These overlaps present a major structural complexity owing to the overlay between two plasma membranes. Secondly, we chose the free plasma membrane that would provide information regarding diffusion limited protein recovery. The second region also helps to serve as the baseline for comparison since free membrane diffusion typically exceeds that of bound membrane molecules. Recording these recoveries individually also allowed us to accurately separate out the distinct timescales for the two protein fractions without requiring complicated bleaching and/or acquisition preferences [155]. Additionally, all measurements were recorded in two steps with different acquisition intervals to allow the correct analysis of a bi-phasic recovery process as initially observed within CRB2-WT cells. Pooled FRAP curves were fitted to a bi-exponential curve fit from which distinct isoform and/or mutant specific patterns could be identified.

Ideally in the case of transmembrane proteins, once the protein has docked within the membrane, the inter-membrane β-barrel/α-helices help define the molecular radius which ultimately controls their speed of diffusion [156,157]. Since both CRB2 and CRB3A harbor only one transmembrane α-helix coupled with two evolutionarily conserved C-terminal domains, the differences within their mobility could be attributed solely to the long ECD of CRB2. Building from our murine kidney expansion results, we confirm that CRB2 forms homotypic interactions within adjacent podocyte membrane edges. Further deriving from its structure, the stability of these interactions

could be hypothesized to be governed by the five calcium binding EGF-like domains within its ECD. Therefore, formation of these homotypic dimers either within CRB2 molecules originating from the same cell (*cis*) or from opposing cells (*trans*) would eventually result in a more immobile protein with an eventually longer recovery time (Table 16).

When comparing the recovery of CRB2-WT with CRB3A-WT and CRB3A-Basic within the two chosen membrane regions, we observed an elevated tau1 for CRB2-WT. Further when we compare the mobile fractions within these two regions for these isoforms we can highlight other crucial differences. In the case of the free plasma membrane region, CRB2-WT exhibits a mobile fraction of ~90% which is similar to CRB3A-WT and CRB3A-Basic. However, within the overlapping membrane region, the data suggests for a more complex molecular architecture since CRB2 shows only a ~70% mobile fraction as opposed to ~90% for CRB3A-WT and CRB3A-Basic.

5.3.1.1. ICD mutants cannot alter CRB2-WT mobility

Comparing the recovery of CRB2-WT against the various binding motif mutants, namely, CRB2-ΔPBM and CRB2-ΔFBM, significant differences with regard to their recovery time or mobile fraction could not be observed. Both these motifs within CRBs are known to interact with multiple other proteins in tandem which ultimately helps regulate podocyte functionality. In particular, the CRB-PALS-PATJ complex is known as a major regulator for cell polarity [71,158]. Whereas, the FBM has been linked to control the connection of CRBs with the actin cytoskeleton [93,159,160]. Additionally, amongst these two conserved motifs, the “ERLI” aa sequence coding for the PBM seems to be more highly conserved across different species as compared to the FBM (Figure 3b). Even within the three human CRBs isoforms, the PBM sequence remains unaltered except for the case of CRB3B [93].

Our initial observation wherein the CRB2-ΔIntra mutant culminates in ER stress (Figure 14d) demonstrates that at least one of the two motifs were essential for membrane localization. Therefore, the absence of kinetic differences amongst the individual mutants was surprising. However, in the case of the CRB2-ΔPBM mutant, we can attribute the effect to the lack of any discernable amounts of endogenous PALS1 being expressed within the podocyte model used. Similar findings have

previously also been reported that demonstrate decreased membrane mobility for CRB3A when co-expressed with PALS1 [101]. Additionally, recent evidence suggests an almost seven-fold higher binding affinity of PALS1 to the PBM of CRB3A as compared with that of CRB1 [161]. Simply based upon the high sequence identity between CRB1 and CRB2, we can therefore, safely assume that our kinetic measurements are in sync with previously known data.

Another point to consider is that the ECD of the ICD mutants was completely intact. Therefore, even though CRB2-ΔPBM and CRB2-ΔFBM lack essential ICDs, they may still be able to establish homotypic interactions using their functional ECDs. Thus, from these results, the existence of active homotypic interactions even within these mutant cell lines could be postulated. A functional CRB2-CRB2 interaction would still allow normal signal transduction to occur between adjoining cells. Downstream effects generated from the lack of individual motifs within these cells might then result in different responses being generated from the different mutants. However, protein kinetics in the free plasma and overlapping membranes remain unaffected.

5.3.1.2. Mutating CRB2s ECD causes increased protein immobilization

Upon complete removal of the ECD; as was the case for the CRB2-ΔExtra mutant, T1 was faster as compared to CRB2-WT. In the free plasma membrane region, CRB2-ΔExtra also shows an ~90% mobile fraction similar to CRB2-WT, CRB3A and CRB3A-Basic. But, contrary to expectations due to its missing ECD, the protein within the overlapping membrane exhibited an even lower mobile fraction than CRB2-WT of ~60%. Existence of such an immobile fraction within CRB2-WT and more specifically within cells expressing CRB2-ΔExtra would therefore require the formation of homotypic protein interactions. These findings would also be in accordance with our previous observations from expanded kidney slices. It also substantiates the hypothesis that calcium binding EGF-like domains could help impart conformational stability, although this remains as a speculation. The observation of a highly immobile fraction within membrane overlaps of CRB2-ΔExtra cells, therefore, suggests for a disturbed cellular morphology. These results in combination with the absence of any documented disease-associated point mutations within these Ca^{2+}-binding domains [61], could indicate that mutations within these domains are probably lethal.

5.3.2. Time-lapses reveal homotypic CRB2-CRB2 either in *Cis* or *Trans* or both

To investigate the interactions between CRB2 of adjacent cells over longer periods of time, we prepared several specific cell co-cultures for time-lapse microscopy (Section 4.5). Distinct morphological trends from multiple measurements were identified that proved to be cell-type specific. Co-cultures of cells expressing two differently labelled CRB2 constructs highlighted the formation of protein dense lateral membrane overlaps (Figure 24). Podocyte membranes form tiny microvillar projections that were enriched with CRB2. These protein-rich membrane protrusions from either cell make contact leading to an interdigitating morphology. Over time, these tiny microvilli diffuse while the membranes from opposing cells overlap one another. This overlapping region becomes heavily enriched with CRB2, which then appears to form a distinct finger-like pattern probably indicating completion of signal transduction (Figure 24; final time point, white arrow).

In comparison, when we look at co-cultures of cells expressing CRB3A-WT and CRB2-WT, the membrane overlaps appear slightly different. Even though, from our time lapses we could visualize that cellular proximity causes podocytes to recruit CRB2 at the site of contact, the membrane overlaps formed were not stable. The overlapping membranes also do not show the distinct finger-like pattern observed earlier with CRB2-CRB2 co-cultures. Finally, CRB2-WT or CRB3A-Basic cells co-cultured with the negative control cell line mCherryx2, helped reveal CRB2 specific cellular traits. It was evident that these podocytes were highly mobile and utilize their membrane protrusions to sense their environment. In the case of cells expressing CRB2-WT, interacting cells were stable over extended periods of time. On the other hand, cells expressing CRB3A-Basic detached within a few hours. Additionally, the presence of stable overlaps immediately post-cytokinesis further re-iterates the role of the ECD of CRB2 to form homotypic protein interactions. Thereby, we conclude that presence and/or absence of CRB2 within microvillar protrusions help decide the fate for cell-cell contacts when two podocytes come close to one another.

5.4. Resolving CRB2-CRB2 homotypic interactions

The enhanced stability of membrane overlaps formed between cells expressing CRB2-WT further led us to investigate this interaction in greater detail. Previously, cell adhesion assays on differentiated podocytes have demonstrated profound differences between intracellularly mutated versions of CRB2 from its WT counterpart [130]. To this effect, the role of the FBM within CRB2 has been extensively investigated. Proteins interacting with the FBM have been postulated to be vital for podocyte foot process reorganization. Probably, signaling cues from the extracellular environment get transmitted through CRB2 leading to conformational changes within the protein structure. These changes mediate interactions with FBM-specific binding partners, which help the cells to reorganize their cytoskeleton depending upon the received signal [159,160]. Therefore, based upon our findings already discussed above we speculate that CRB2 acts more as a sensor within podocyte membrane protrusions. The effective binding of its N-terminal EGF repeats eventually helps to detect the cells' immediate surroundings while simultaneously providing impulses to the inside of the cell. Subsequently, intracellular binding partners form crucial protein complexes after signal transmission. These protein complexes stimulate cytoskeleton arrangement and can govern the direction of cellular mobility.

5.4.1. Super-resolution microscopy cannot resolve CRB2-CRB2 interactions

In order to better understand CRB2s signaling mechanism that eventually could lead to the formation of the SD, it becomes crucial to resolve the exact protein conformation occurring within homotypic CRB2-CRB2 interactions. Across species, depending solely upon their function, CRBs isoforms are expressed heterogeneously within different epithelial cell types [75,132,134,162,135]. Homotypic CRBs interactions within these cells exist within one of two known conformations, either *cis* [132,133] or *trans* [134,107,135]. Thus, assuming a random distribution of CRB2 over the membrane combined with its estimated ECD length derived using RoseTTaFold (Section 4.1; [109]), we hypothesized the inter-cellular gap between adjoining cells expressing CRB2 to be between 50-100 nm depending on its configuration. The combination of Pro-ExM [116,163,164] with Airyscan laser scanning confocal imaging [136] could theoretically achieve a resolution of ~30-40 nm. At this resolution, we assumed that the dense yellow plaques formed by the interdigitating podocyte

membranes expressing differently tagged CRB2 variants as visualized earlier in Section 4.5.2 would appear as distinct fluorophores. Depending on the fluorophore distribution originating from the inter-fluorophore distance we assumed either a stacked or alternating morphology. These two assumed morphologies with their respective inter-fluorophore distance of either ~80-100 nm or ~55-75 nm, would be representative of a *cis* or *trans* configuration, respectively (Figure 28).

Our results, however, were not in accordance with our expectations. Apart from the fact that we were never practically able to achieve a sub-60 nm resolution, multiple factors could be identified that may have distorted the signal. First, in order to circumvent fluorophore instability in expanded cells, especially observed in the case of eGFP [165,166], we made use of antibody labelling for signal enhancement. Conventional IgGs are known to be on average ~15nm in length [167]. This implies that even with direct labelling, the minimum distance introduced between the fluorophore and labelled epitope by using these antibodies would be 15nm. In the case of indirect labelling, however, depending upon molecular crowding the same distance might range from as low as 30 to ~50nm. Thus, in order to keep the fluorophore-to-epitope distortion below 6nm, especially in the case for eGFP, we made use of AlexaFluor 488-labelled GFP-booster nanobodies® [168]. However, the inclusion of the additional fluorophores might have contributed to erroneous signal detection. Secondly, the fixing agent utilized for immunocytochemistry and the protocol conditions, have also been known to cause distortions within the actin cytoskeleton leading to introduction of unwanted artefacts [169]. Recent publications have also highlighted how different fixatives especially alter transmembrane proteins. Creation of heavy crosslinks via aldehyde-based fixatives or dehydration and precipitation caused by alcohol fixatives could lead to protein aggregate formation. Random clusters of protein aggregates formed in this manner, would cause distortions of the naturally present inter-protein distances [170]. Conclusively, both these factors along with minute expansion related distortions would thus, explain the randomly organized dot-like fluorophore distribution we observed within expanded microvilli. We assume that what we observed after expansion were randomly aggregated eGFP or Halo tagged-CRB2 proteins distributed unevenly within podocyte microvilli.

5.4.2. Traction force microscopy confirms CRB2-CRB2 act in *Trans*

The final attempt to clarify CRB2-CRB2 interactions came from data generated by our collaboration partners at the Institute of Biological Image Processing in Jülich headed by Prof. Dr. Rudolf Merkel. Using traction force microscopy, they were able to directly visualize differences in strain energy being exerted by cell duplets expressing CRB2. We hypothesized that two adjacent podocytes expressing CRB2, would exert antagonistic forces against each other in order to bring their membranes in contact as seen with our time lapse measurements. Additionally, since we observed that CRB2 expressing cells can maintain their interactions over time (see Section 4.5.1), we speculated that similar antagonistic forces would persist even after initial contact to help maintain the interdigitated state and could therefore be observed within cell duplets. Surprisingly, however, even though we observed higher forces being exerted in the case of cell duplets expressing CRB2 as opposed to the native podocytes but the force fields were directed towards the substrate on which the cells were seeded (Figure 32 a-c versus g-i and m).

Subsequently, it was suggested that further investigations be considered so as to explore the changes occurring within the actin cytoskeleton and FA sites with respect to CRB2 expression. Upon comparing the distribution of actin and vinculin with CRB2 expressing cells against native podocytes, it becomes evidently clear that CRB2 acts as a cellular environment sensor. CRB2 expressing duplets occupy a smaller substrate area with lesser number of FA sites as opposed to native podocytes. The FAs formed by CRB2 expressing duplets, however, have higher area coverage (Figure 32 n-p). Additionally, CRB2 expressing podocyte duplets localize actin closer to cell borders in a cortical structure as opposed to native podocytes (Figure 32 d versus j). Building from our mobility assessments performed within the overlapping membranes in these duplets and the traction force microscopy data along with cytoskeletal and FA immunostainings, we conclude that CRB2 acts in *trans* with its long ECD serving as the antennae for the sensor. Single CRB2 expressing podocytes potentially scan their immediate environment using the ECD. Signals received from neighboring cells expressing CRB2 trigger conformational changes that transmit towards the inside. CRB2s ICDs possibly stimulate the actin cytoskeleton to control the direction of cellular movement or cause the cells to arrest motion and repose in place by broadening its FA sites with the substrate.

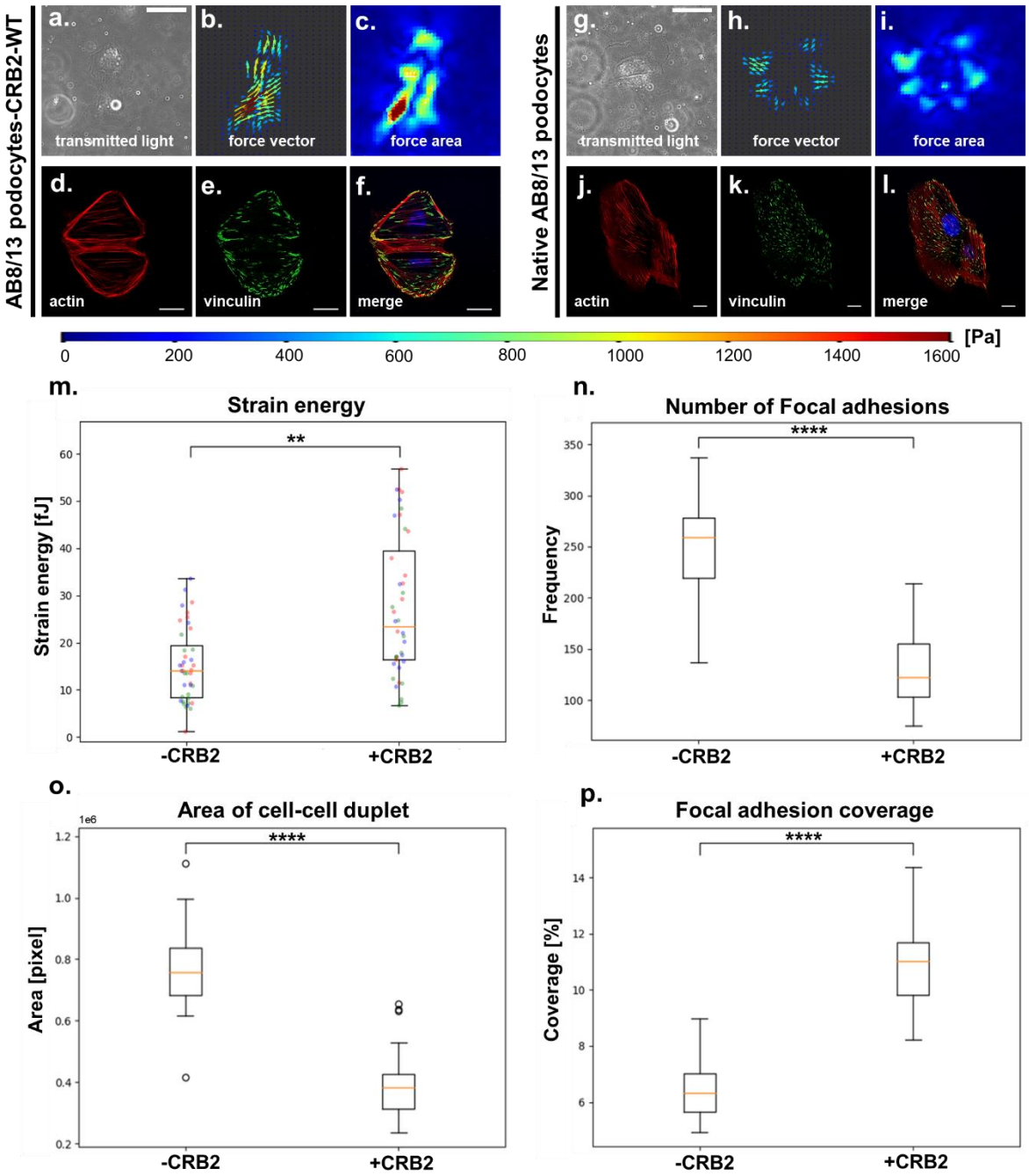

Figure 32: Traction force microscopy measurements and analysis.
(a-f) AB8/13 podocytes expressing CRB2-WT. **(g-l)** Non-transduced AB8/13 podocytes. **(a,g)** Representative transmitted light images of cell duplets. **(b,h)** Calculated forces highlighting force directions within cell duplets. **(c,i)** Calculated forces highlighting force amplitudes within cell duplets. False color code applies to **(b)**, **(c)**, **(h)** and **(i)**. **(d,j)** Representative image showing actin distribution within cell duplets. **(e,k)** Representative image showing vinculin distribution within cell duplets. **(f, l)** Merged image showing actin and vinculin distribution within cell duplets. **(m)** Individual strain energies retrieved from at least 30 different cell duplet measurements. Different color dots represent independent measurements. Significance score: **-p<0.05. (n) Total number of focal adhesion sites. **(o)** Area of a complete cell duplet estimated using a computer-software using mean gray values. **(p)** Overall focal adhesion coverage area as percentage of total surface area. Significance score: ****-p<0.001.Scale bars: **a,g:** 25µm; **d-f** and **j-l:** 20µm. (Data courtesy: Sven Gerlach [unpublished data])

5.4.3. CRB2-CRB2 *trans* interactions signal ICDs to arrest mobility leading to enhanced cellular adhesion

As evidenced from our kinetic measurements, co-culture time-lapses, traction force assessment and immunostaining analysis CRB2 expressing cell duplets maintain stable interactions over time. Even after cell division, CRB2 expressing podocytes maintain interactions amongst daughter cells. To further substantiate our claim that CRB2 acting in *trans* governs cellular mobility/arrest, we co-cultivated CRB2-WT, CRB3A-WT and CRB3A-Basic cells along with the mCherryx2 cells over extended periods of time such as for a week. Our hypothesis was that *trans* acting CRB2 expressing cell duplets should be able to stick together. In order to circumvent other contributors to clustering such as cell duplication, the same number of cells from each cell type were seeded at the beginning of each experiment replicate. Therefore, CRB2 expression within podocytes could be attributed as the root cause for observing clustering effects, if any. These CRB2 expressing cell clusters would eventually grow in size forming dense inter-connected cellular plaques. CRB3A-WT and CRB3A-Basic expressing podocytes, on the other hand, would only be able to form smaller clusters. Since, our non-transduced AB8/13 native podocyte cells had a doubling rate of ~37 hours, hence a week of cultivation would essentially provide for nearly three duplication events. The final cell count obtained at the end of the week calculated from the nuclear staining confirmed accurate cell seeding at the start of the experiment. It also helped to normalize the cell clustering effects observed (Section 4.6). Deriving from their ability to pilot cellular mobility and therefore, subsequently to sort against other cell types, CRB2 expressing cells were able to demonstrate a higher clustering effect. Anomalously, as opposed to recent findings within Zebrafish retinal cells [107], our CRB3A expressing cells were also found to elicit a similar clustering response as CRB2, although to a much lesser extent. The occurrence of such an enhanced cellular cohesion within CRB3A expressing HeLa and HEK cells have also been investigated earlier [171].

Lastly, we compared CRB2 versus CRB3A expressing podocyte duplets in terms of their actin organization and FA sites. Surprisingly, both CRB2 and CRB3A showcased the ability to orient actin bundles near the cell borders in a cortical structure. Therefore, CRB3A, much like CRB2 leads to enhanced cellular cohesion along with actin bundle reorganization. Our findings complement previously documented results observed in other cell types [171]. A striking feature observed was the ability of CRB2 expressing

cells to vacate membrane space so as to allow formation of broader vinculin rich FA sites (Figure 30 and Figure 31). However, such a feature could not be observed in the case for CRB3A expressing cell duplets. Additionally, CRB3A expressing duplets had more FAs that were smaller than the ones measured for the CRB2 duplets.

5.5. Conclusion and Outlook

Both CRB2 and CRB3A are co-expressed during early stages of human kidney development. Their localization and the time at which they begin to get expressed predominantly governs podocyte maturity. From our results, we would infer that within interdigitating podocyte microvilli, expression of CRB3A probably precedes the recruitment of CRB2. This inference is solely based upon its higher membrane mobility along with the ability of CRB3A expressing podocytes to show cellular cohesion. Therefore, podocyte microvillar cohesion is initiated by CRB3A. Once recruited, podocytes use CRB2 as a possible sensor for extracellular cues. Conformational changes within CRB2 caused by homotypic *trans* interactions in the presence of other CRB2 expressing podocytes lead to signal transductions. CRB2-CRB2 interactions are not static but rather a highly dynamic process and extracellular signals, thus transmitted into the cell help direct cellular mobility via activation of intracellular protein complexes that connect with the actin cytoskeleton. Cytoskeletal re-organization along with forces that initiate strong substrate adhesion, thereby, enables podocytes to arrest motion (Figure 33). The location at which podocytes arrest their motion, hence, demarcate the final apical orientation. Eventually this then helps establish the apico-basal polarity wherein apically oriented podocytes begin to secrete factors that recruit GEC's, thus forming the basal GBM. Finally, a functional filtration barrier gets formed that allows for normal renal function.

The findings from this thesis provide a basic understanding of the functioning mechanism of CRB2. Further research should, therefore, be conducted so as to fully elucidate the function of the individual domains within CRB2s ECD. Developing upon the results from our traction force microscopy data, it would be possible to generate N-terminal tagged CRB2 constructs for visualizing *trans* interactions in living cells via Fluorecence Resonance Energy Transfer (FRET; [172]) imaging.

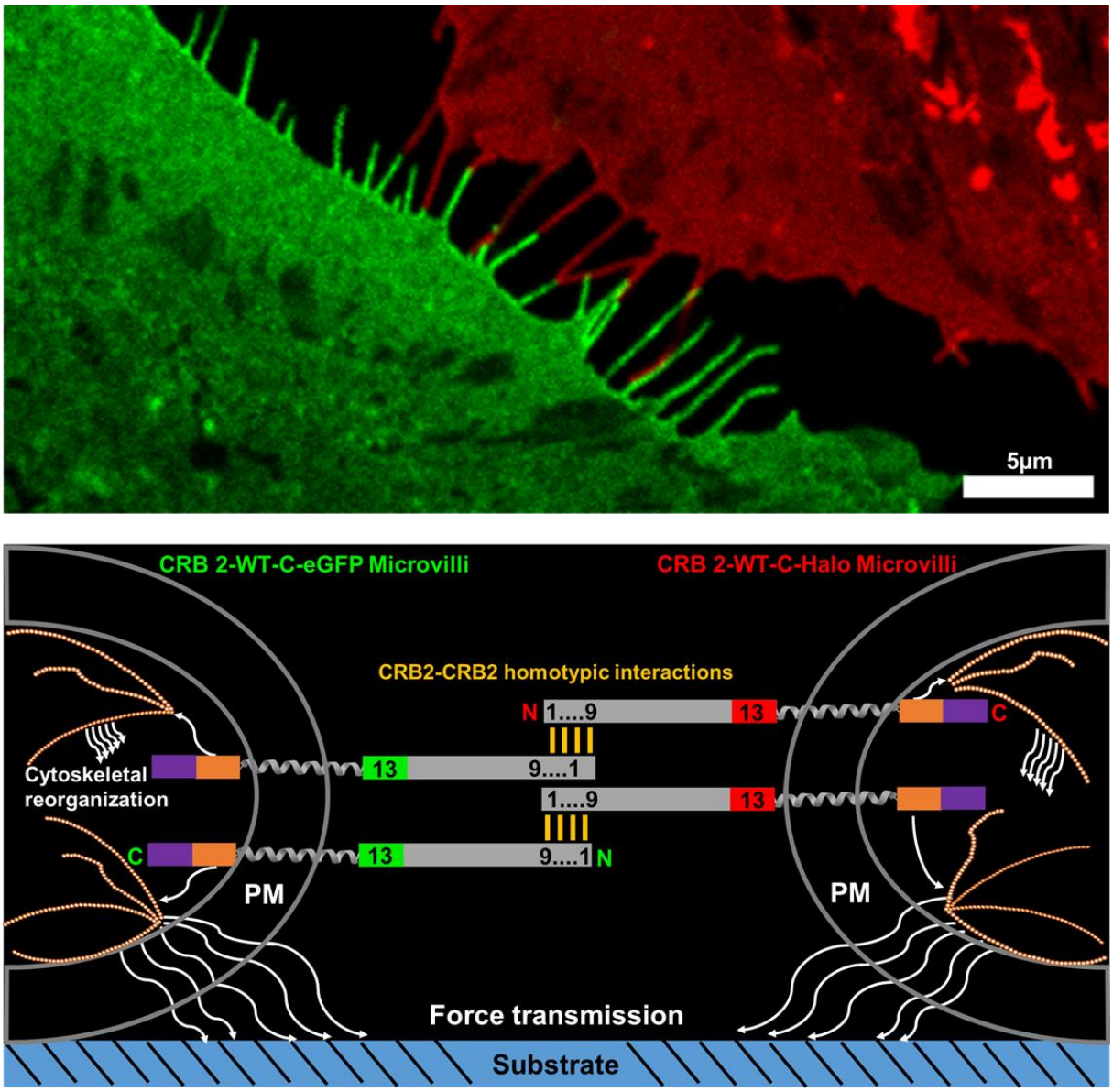

Figure 33: Proposed model of CRB2-CRB2 homotypic interactions in *trans*.
Calcium-binding N-terminal EGF repeats from opposing microvilli interdigitate that eventually lead to signal transmission into the cell. Activation via intracellular protein complexes binding with the FBM (orange squares) connect with the actin cytoskeleton leading to cellular re-organization. eGFP: green squares; FERM binding motif or FBM: orange squares; HaloTag: red squares; Numbers: Respective EGF-like domains; PDZ-binding motif or PBM: purple squares; and PM: Plasma membrane. Scale bar: 5 µm. HaloTag staining dye: JF 646 ® [800 nM].

6. References

1. Scott RP, Quaggin SE (2015) Review series: The cell biology of renal filtration. The Journal of cell biology 209 (2): 199–210.
2. Wadei HM, Textor SC (2012) The role of the kidney in regulating arterial blood pressure. Nature reviews. Nephrology 8 (10): 602–609.
3. Donnelly S (2003) Why is erythropoietin made in the kidney? The kidney functions as a 'critmeter' to regulate the hematocrit. Advances in experimental medicine and biology 543: 73–87.
4. Goltzman D (2018) Functions of vitamin D in bone. Histochemistry and cell biology 149 (4): 305–312.
5. Wei K, Yin Z, Xie Y (2016) Roles of the kidney in the formation, remodeling and repair of bone. Journal of nephrology 29 (3): 349–357.
6. Munger K, Kost C, Brenner B, Maddox D (2012) The Renal Circulations and Glomerular Ultrafiltration. pp. 94–137.
7. Stein JH, Fadem SZ (1978) The renal circulation. JAMA 239 (13): 1308–1312.
8. Lote C (2012) Principles of Renal Physiology. Principles of Renal Physiology. pp. 161–165.
9. Puelles VG, Hoy WE, Hughson MD, Diouf B, Douglas-Denton RN et al. (2011) Glomerular number and size variability and risk for kidney disease. Current opinion in nephrology and hypertension 20 (1): 7–15.
10. Kalluri R (2006) Proteinuria with and without renal glomerular podocyte effacement. Journal of the American Society of Nephrology : JASN 17 (9): 2383–2389.
11. Tryggvason K, Wartiovaara J (2005) How does the kidney filter plasma. Physiology (Bethesda, Md.) 20: 96–101.
12. Inker LA, Eneanya ND, Coresh J, Tighiouart H, Wang D et al. (2021) New Creatinine- and Cystatin C-Based Equations to Estimate GFR without Race. The New England journal of medicine 385 (19): 1737–1749.
13. Lerma EV (2008) Approach to the patient with renal disease. Primary care 35 (2): 183-94, v.
14. Daehn IS, Duffield JS (2021) The glomerular filtration barrier: a structural target for novel kidney therapies. Nature reviews. Drug discovery 20 (10): 770–788.
15. Casalena GA, Yu L, Gil R, Rodriguez S, Sosa S et al. (2020) The diabetic microenvironment causes mitochondrial oxidative stress in glomerular endothelial cells and pathological crosstalk with podocytes. Cell communication and signaling : CCS 18 (1): 105.
16. Wikimedia Foundation (2014) WikiJournal of medicine. Available: http://bibpurl.oclc.org/web/81473.
17. Chiang C-K, Inagi R (2010) Glomerular diseases: genetic causes and future therapeutics. Nature reviews. Nephrology 6 (9): 539–554.
18. Peti-Peterdi J, Sipos A (2010) A high-powered view of the filtration barrier. Journal of the American Society of Nephrology : JASN 21 (11): 1835–1841.
19. Haraldsson B, Nyström J, Deen WM (2008) Properties of the glomerular barrier and mechanisms of proteinuria. Physiological reviews 88 (2): 451–487.

20. Assady S, Wanner N, Skorecki KL, Huber TB (2017) New Insights into Podocyte Biology in Glomerular Health and Disease. Journal of the American Society of Nephrology : JASN 28 (6): 1707–1715.
21. Farquhar MG (1975) Editorial: The primary glomerular filtration barrier--basement membrane or epithelial slits. Kidney international 8 (4): 197–211.
22. Karnovsky MJ, Ainsworth SK (1972) The structural basis of glomerular filtration. Advances in nephrology from the Necker Hospital 2: 35–60.
23. Chang RL, Deen WM, Robertson CR, Brenner BM (1975) Permselectivity of the glomerular capillary wall: III. Restricted transport of polyanions. Kidney international 8 (4): 212–218.
24. Thomson SC, Blantz RC (2010) A new role for charge of the glomerular capillary membrane. Journal of the American Society of Nephrology : JASN 21 (12): 2011–2013.
25. Robert B, Zhao X, Abrahamson DR (2000) Coexpression of neuropilin-1, Flk1, and VEGF(164) in developing and mature mouse kidney glomeruli. American journal of physiology. Renal physiology 279 (2): F275-82.
26. Eremina V, Cui S, Gerber H, Ferrara N, Haigh J et al. (2006) Vascular endothelial growth factor a signaling in the podocyte-endothelial compartment is required for mesangial cell migration and survival. Journal of the American Society of Nephrology : JASN 17 (3): 724–735.
27. Eremina V, Sood M, Haigh J, Nagy A, Lajoie G et al. (2003) Glomerular-specific alterations of VEGF-A expression lead to distinct congenital and acquired renal diseases. The Journal of clinical investigation 111 (5): 707–716.
28. Sugimoto H, Hamano Y, Charytan D, Cosgrove D, Kieran M et al. (2003) Neutralization of circulating vascular endothelial growth factor (VEGF) by anti-VEGF antibodies and soluble VEGF receptor 1 (sFlt-1) induces proteinuria. The Journal of biological chemistry 278 (15): 12605–12608.
29. Levick JR, Smaje LH (1987) An analysis of the permeability of a fenestra. Microvascular research 33 (2): 233–256.
30. Rostgaard J, Qvortrup K (2002) Sieve plugs in fenestrae of glomerular capillaries--site of the filtration barrier. Cells, tissues, organs 170 (2-3): 132–138.
31. Curry FE, Adamson RH (2012) Endothelial glycocalyx: permeability barrier and mechanosensor. Annals of biomedical engineering 40 (4): 828–839.
32. Hjalmarsson C, Johansson BR, Haraldsson B (2004) Electron microscopic evaluation of the endothelial surface layer of glomerular capillaries. Microvascular research 67 (1): 9–17.
33. Hobeika L, Barati MT, Caster DJ, McLeish KR, Merchant ML (2017) Characterization of glomerular extracellular matrix by proteomic analysis of laser-captured microdissected glomeruli. Kidney international 91 (2): 501–511.
34. Abrahamson DR (2012) Role of the podocyte (and glomerular endothelium) in building the GBM. Seminars in nephrology 32 (4): 342–349.
35. Miner JH (2012) The glomerular basement membrane. Experimental cell research 318 (9): 973–978.
36. Kubosawa H, Kondo Y (1985) Ultrastructural organization of the glomerular basement membrane as revealed by a deep-etch replica method. Cell and tissue research 242 (1): 33–39.

37. Hironaka K, Makino H, Yamasaki Y, Ota Z (1993) Pores in the glomerular basement membrane revealed by ultrahigh-resolution scanning electron microscopy. Nephron 64 (4): 647–649.
38. Suleiman H, Zhang L, Roth R, Heuser JE, Miner JH et al. (2013) Nanoscale protein architecture of the kidney glomerular basement membrane. eLife 2: e01149.
39. Grahammer F (2017) New structural insights into podocyte biology. Cell and tissue research 369 (1): 5–10.
40. Ichimura K, Kurihara H, Sakai T (2003) Actin filament organization of foot processes in rat podocytes. The journal of histochemistry and cytochemistry : official journal of the Histochemistry Society 51 (12): 1589–1600.
41. Furukawa T, Ohno S, Oguchi H, Hora K, Tokunaga S et al. (1991) Morphometric study of glomerular slit diaphragms fixed by rapid-freezing and freeze-substitution. Kidney international 40 (4): 621–624.
42. Pätäri-Sampo A, Ihalmo P, Holthöfer H (2006) Molecular basis of the glomerular filtration: nephrin and the emerging protein complex at the podocyte slit diaphragm. Annals of medicine 38 (7): 483–492.
43. Reiser J, Kriz W, Kretzler M, Mundel P (2000) The glomerular slit diaphragm is a modified adherens junction. Journal of the American Society of Nephrology : JASN 11 (1): 1–8.
44. Akilesh S, Huber TB, Wu H, Wang G, Hartleben B et al. (2008) Podocytes use FcRn to clear IgG from the glomerular basement membrane. Proceedings of the National Academy of Sciences of the United States of America 105 (3): 967–972.
45. Pavenstädt H, Kriz W, Kretzler M (2003) Cell biology of the glomerular podocyte. Physiological reviews 83 (1): 253–307.
46. Ruotsalainen V, Ljungberg P, Wartiovaara J, Lenkkeri U, Kestilä M et al. (1999) Nephrin is specifically located at the slit diaphragm of glomerular podocytes. Proceedings of the National Academy of Sciences of the United States of America 96 (14): 7962–7967.
47. Holzman LB, St John PL, Kovari IA, Verma R, Holthofer H et al. (1999) Nephrin localizes to the slit pore of the glomerular epithelial cell. Kidney international 56 (4): 1481–1491.
48. Grahammer F, Wigge C, Schell C, Kretz O, Patrakka J et al. (2016) A flexible, multilayered protein scaffold maintains the slit in between glomerular podocytes. JCI insight 1 (9).
49. Wartiovaara J, Ofverstedt L-G, Khoshnoodi J, Zhang J, Mäkelä E et al. (2004) Nephrin strands contribute to a porous slit diaphragm scaffold as revealed by electron tomography. The Journal of clinical investigation 114 (10): 1475–1483.
50. Schwarz K, Simons M, Reiser J, Saleem MA, Faul C et al. (2001) Podocin, a raft-associated component of the glomerular slit diaphragm, interacts with CD2AP and nephrin. The Journal of clinical investigation 108 (11): 1621–1629.
51. Kestilä M, Lenkkeri U, Männikkö M, Lamerdin J, McCready P et al. (1998) Positionally cloned gene for a novel glomerular protein--nephrin--is mutated in congenital nephrotic syndrome. Molecular cell 1 (4): 575–582.
52. Boute N, Gribouval O, Roselli S, Benessy F, Lee H et al. (2000) NPHS2, encoding the glomerular protein podocin, is mutated in autosomal recessive steroid-resistant nephrotic syndrome. Nature genetics 24 (4): 349–354.
53. Ciani L, Patel A, Allen ND, ffrench-Constant C (2003) Mice Lacking the Giant Protocadherin mFAT1 Exhibit Renal Slit Junction Abnormalities and a Partially

Penetrant Cyclopia and Anophthalmia Phenotype. Molecular and cellular biology 23 (10): 3575–3582.
54. Gerke P, Huber TB, Sellin L, Benzing T, Walz G (2003) Homodimerization and heterodimerization of the glomerular podocyte proteins nephrin and NEPH1. Journal of the American Society of Nephrology : JASN 14 (4): 918–926.
55. Heikkilä E, Ristola M, Havana M, Jones N, Holthöfer H et al. (2011) Trans-interaction of nephrin and Neph1/Neph3 induces cell adhesion that associates with decreased tyrosine phosphorylation of nephrin. The Biochemical journal 435 (3): 619–628.
56. Fukasawa H, Bornheimer S, Kudlicka K, Farquhar MG (2009) Slit diaphragms contain tight junction proteins. Journal of the American Society of Nephrology : JASN 20 (7): 1491–1503.
57. Hartleben B, Schweizer H, Lübben P, Bartram MP, Möller CC et al. (2008) Neph-Nephrin proteins bind the Par3-Par6-atypical protein kinase C (aPKC) complex to regulate podocyte cell polarity. The Journal of biological chemistry 283 (34): 23033–23038.
58. Hirose T, Satoh D, Kurihara H, Kusaka C, Hirose H et al. (2009) An essential role of the universal polarity protein, aPKClambda, on the maintenance of podocyte slit diaphragms. PloS one 4 (1): e4194.
59. Huber TB, Hartleben B, Winkelmann K, Schneider L, Becker JU et al. (2009) Loss of podocyte aPKClambda/iota causes polarity defects and nephrotic syndrome. Journal of the American Society of Nephrology : JASN 20 (4): 798–806.
60. Blattner SM, Hodgin JB, Nishio M, Wylie SA, Saha J et al. (2013) Divergent functions of the Rho GTPases Rac1 and Cdc42 in podocyte injury. Kidney international 84 (5): 920–930.
61. Slavotinek AM (2016) The Family of Crumbs Genes and Human Disease. Molecular syndromology 7 (5): 274–281.
62. Kovesdy CP (2022) Epidemiology of chronic kidney disease: an update 2022. Kidney international supplements 12 (1): 7–11.
63. Romagnani P, Remuzzi G, Glassock R, Levin A, Jager KJ et al. (2017) Chronic kidney disease. Nature reviews. Disease primers 3: 17088.
64. Shankland SJ (2006) The podocyte's response to injury: role in proteinuria and glomerulosclerosis. Kidney international 69 (12): 2131–2147.
65. Khanna R (2011) Clinical presentation & management of glomerular diseases: hematuria, nephritic & nephrotic syndrome. Missouri medicine 108 (1): 33–36.
66. Rosenberg AZ, Kopp JB (2017) Focal Segmental Glomerulosclerosis. Clinical journal of the American Society of Nephrology : CJASN 12 (3): 502–517.
67. Hull RP, Goldsmith DJA (2008) Nephrotic syndrome in adults. Bmj 336 (7654): 1185–1189.
68. Ciechanowicz A, Brodkiewicz A, Bińczak-Kuleta A, Parczewski M, Czekalski S (2008) "Treasure your exceptions": recent advances in molecular genetics of glomerular disease. Journal of applied genetics 49 (1): 93–99.
69. Menzel S, Moeller MJ (2011) Role of the podocyte in proteinuria. Pediatric nephrology 26 (10): 1775–1780.
70. Assémat E, Bazellières E, Pallesi-Pocachard E, Le Bivic A, Massey-Harroche D (2008) Polarity complex proteins. Biochimica et biophysica acta 1778 (3): 614–630.

71. Bulgakova NA, Knust E (2009) The Crumbs complex: from epithelial-cell polarity to retinal degeneration. Journal of cell science 122 (Pt 15): 2587–2596.
72. Tepass U, Theres C, Knust E (1990) crumbs encodes an EGF-like protein expressed on apical membranes of Drosophila epithelial cells and required for organization of epithelia. Cell 61 (5): 787–799.
73. Nüsslein-Volhard C, Wieschaus E, Kluding H (1984) Mutations affecting the pattern of the larval cuticle inDrosophila melanogaster : I. Zygotic loci on the second chromosome. Wilhelm Roux's archives of developmental biology 193 (5): 267–282.
74. Tepass U (2012) The apical polarity protein network in Drosophila epithelial cells: regulation of polarity, junctions, morphogenesis, cell growth, and survival. Annual review of cell and developmental biology 28: 655–685.
75. Thompson BJ, Pichaud F, Röper K (2013) Sticking together the Crumbs - an unexpected function for an old friend. Nature reviews. Molecular cell biology 14 (5): 307–314.
76. Robinson BS, Huang J, Hong Y, Moberg KH (2010) Crumbs regulates Salvador/Warts/Hippo signaling in Drosophila via the FERM-domain protein Expanded. Current biology : CB 20 (7): 582–590.
77. Grzeschik NA, Parsons LM, Allott ML, Harvey KF, Richardson HE (2010) Lgl, aPKC, and Crumbs regulate the Salvador/Warts/Hippo pathway through two distinct mechanisms. Current biology : CB 20 (7): 573–581.
78. Ling C, Zheng Y, Yin F, Yu J, Huang J et al. (2010) The apical transmembrane protein Crumbs functions as a tumor suppressor that regulates Hippo signaling by binding to Expanded. Proceedings of the National Academy of Sciences of the United States of America 107 (23): 10532–10537.
79. Chen C-L, Gajewski KM, Hamaratoglu F, Bossuyt W, Sansores-Garcia L et al. (2010) The apical-basal cell polarity determinant Crumbs regulates Hippo signaling in Drosophila. Proceedings of the National Academy of Sciences of the United States of America 107 (36): 15810–15815.
80. Richardson ECN, Pichaud F (2010) Crumbs is required to achieve proper organ size control during Drosophila head development. Development 137 (4): 641–650.
81. Ohata S, Aoki R, Kinoshita S, Yamaguchi M, Tsuruoka-Kinoshita S et al. (2011) Dual roles of Notch in regulation of apically restricted mitosis and apicobasal polarity of neuroepithelial cells. Neuron 69 (2): 215–230.
82. Gosens I, den Hollander AI, Cremers FPM, Roepman R (2008) Composition and function of the Crumbs protein complex in the mammalian retina. Experimental eye research 86 (5): 713–726.
83. Watanabe T, Miyatani S, Katoh I, Kobayashi S, Ikawa Y (2004) Expression of a novel secretory form (Crb1s) of mouse Crumbs homologue Crb1 in skin development. Biochemical and biophysical research communications 313 (2): 263–270.
84. Richard M, Roepman R, Aartsen WM, van Rossum AGSH, Hollander AI den et al. (2006) Towards understanding CRUMBS function in retinal dystrophies. Human molecular genetics 15 Spec No 2: R235-43.
85. Hollander AI den, Davis J, van der Velde-Visser SD, Zonneveld MN, Pierrottet CO et al. (2004) CRB1 mutation spectrum in inherited retinal dystrophies. Human mutation 24 (5): 355–369.

86. Hollander AI den, Ghiani M, Kok YJM de, Wijnholds J, Ballabio A et al. (2002) Isolation of Crb1, a mouse homologue of Drosophila crumbs, and analysis of its expression pattern in eye and brain. Mechanisms of development 110 (1-2): 203–207.
87. Pocha SM, Knust E (2013) Complexities of Crumbs function and regulation in tissue morphogenesis. Current biology : CB 23 (7): R289-93.
88. Xiao Z, Patrakka J, Nukui M, Chi L, Niu D et al. (2011) Deficiency in Crumbs homolog 2 (Crb2) affects gastrulation and results in embryonic lethality in mice. Developmental dynamics : an official publication of the American Association of Anatomists 240 (12): 2646–2656.
89. Ramkumar N, Omelchenko T, Silva-Gagliardi NF, McGlade CJ, Wijnholds J et al. (2016) Crumbs2 promotes cell ingression during the epithelial-to-mesenchymal transition at gastrulation. Nature cell biology 18 (12): 1281–1291.
90. van den Hurk, José A J M, Rashbass P, Roepman R, Davis J, Voesenek KEJ et al. (2005) Characterization of the Crumbs homolog 2 (CRB2) gene and analysis of its role in retinitis pigmentosa and Leber congenital amaurosis. Molecular vision 11: 263–273.
91. Dudok JJ, Murtaza M, Henrique Alves C, Rashbass P, Wijnholds J (2016) Crumbs 2 prevents cortical abnormalities in mouse dorsal telencephalon. Neuroscience research 108: 12–23.
92. Hamano S, Nishibori Y, Hada I, Mikami N, Ito-Nitta N et al. (2018) Association of crumbs homolog-2 with mTORC1 in developing podocyte. PloS one 13 (8): e0202400.
93. Hochapfel F, Denk L, Mendl G, Schulze U, Maaßen C et al. (2017) Distinct functions of Crumbs regulating slit diaphragms and endocytosis in Drosophila nephrocytes. Cellular and molecular life sciences : CMLS 74 (24): 4573–4586.
94. Ebarasi L, Ashraf S, Bierzynska A, Gee HY, McCarthy HJ et al. (2015) Defects of CRB2 cause steroid-resistant nephrotic syndrome. American journal of human genetics 96 (1): 153–161.
95. Slavotinek A, Kaylor J, Pierce H, Cahr M, DeWard SJ et al. (2015) CRB2 mutations produce a phenotype resembling congenital nephrosis, Finnish type, with cerebral ventriculomegaly and raised alpha-fetoprotein. American journal of human genetics 96 (1): 162–169.
96. Möller-Kerutt A, Rodriguez-Gatica JE, Wacker K, Bhatia R, Siebrasse J-P et al. (2021) Crumbs2 Is an Essential Slit Diaphragm Protein of the Renal Filtration Barrier. Journal of the American Society of Nephrology : JASN 32 (5): 1053–1070.
97. Quinn PM, Buck TM, Mulder AA, Ohonin C, Alves CH et al. (2019) Human iPSC-Derived Retinas Recapitulate the Fetal CRB1 CRB2 Complex Formation and Demonstrate that Photoreceptors and Müller Glia Are Targets of AAV5. Stem cell reports 12 (5): 906–919.
98. Quinn PM, Pellissier LP, Wijnholds J (2017) The CRB1 Complex: Following the Trail of Crumbs to a Feasible Gene Therapy Strategy. Frontiers in neuroscience 11: 175.
99. Alves CH, Bossers K, Vos RM, Essing AHW, Swagemakers S et al. (2013) Microarray and morphological analysis of early postnatal CRB2 mutant retinas on a pure C57BL/6J genetic background. PloS one 8 (12): e82532.
100. Charrier LE, Loie E, Laprise P (2015) Mouse Crumbs3 sustains epithelial tissue morphogenesis in vivo. Scientific reports 5: 17699.

101. Djuric I, Siebrasse JP, Schulze U, Granado D, Schlüter MA et al. (2016) The C-terminal domain controls the mobility of Crumbs 3 isoforms. Biochimica et biophysica acta 1863 (6 Pt A): 1208–1217.
102. Makarova O, Roh MH, Liu C-J, Laurinec S, Margolis B (2003) Mammalian Crumbs3 is a small transmembrane protein linked to protein associated with Lin-7 (Pals1). Gene 302 (1-2): 21–29.
103. Katoh M, Katoh M (2004) Identification and characterization of Crumbs homolog 2 gene at human chromosome 9q33.3. International journal of oncology 24 (3): 743–749.
104. Adutwum M, Hurst A, Mirzaa G, Kushner JD, Rogers C et al. (2023) Six new cases of CRB2-related syndrome and a review of clinical findings in 28 reported patients. Clinical genetics 103 (1): 97–102.
105. Jaron R, Rosenfeld N, Zahdeh F, Carmi S, Beni-Adani L et al. (2016) Expanding the phenotype of CRB2 mutations - A new ciliopathy syndrome. Clinical genetics 90 (6): 540–544.
106. Lamont RE, Tan W-H, Innes AM, Parboosingh JS, Schneidman-Duhovny D et al. (2016) Expansion of phenotype and genotypic data in CRB2-related syndrome. European journal of human genetics : EJHG 24 (10): 1436–1444.
107. Zou J, Wang X, Wei X (2012) Crb apical polarity proteins maintain zebrafish retinal cone mosaics via intercellular binding of their extracellular domains. Developmental cell 22 (6): 1261–1274.
108. Jumper J, Evans R, Pritzel A, Green T, Figurnov M et al. (2021) Highly accurate protein structure prediction with AlphaFold. Nature 596 (7873): 583–589. Available: https://doi.org/10.1038/s41586-021-03819-2.
109. Baek M, DiMaio F, Anishchenko I, Dauparas J, Ovchinnikov S et al. (2021) Accurate prediction of protein structures and interactions using a three-track neural network. Science (New York, N.Y.) 373 (6557): 871–876.
110. Saleem MA, O'Hare MJ, Reiser J, Coward RJ, Inward CD et al. (2002) A conditionally immortalized human podocyte cell line demonstrating nephrin and podocin expression. Journal of the American Society of Nephrology : JASN 13 (3): 630–638.
111. Granado D, Müller D, Krausel V, Kruzel-Davila E, Schuberth C et al. (2017) Intracellular APOL1 Risk Variants Cause Cytotoxicity Accompanied by Energy Depletion. Journal of the American Society of Nephrology : JASN 28 (11): 3227–3238.
112. Schulze U, Vollenbröker B, Braun DA, van Le T, Granado D et al. (2014) The Vac14-interaction network is linked to regulators of the endolysosomal and autophagic pathway. Molecular & cellular proteomics : MCP 13 (6): 1397–1411.
113. Thomas P, Smart TG (2005) HEK293 cell line: a vehicle for the expression of recombinant proteins. Journal of pharmacological and toxicological methods 51 (3): 187–200.
114. van de Pavert SA, Kantardzhieva A, Malysheva A, Meuleman J, Versteeg I et al. (2004) Crumbs homologue 1 is required for maintenance of photoreceptor cell polarization and adhesion during light exposure. Journal of cell science 117 (Pt 18): 4169–4177.
115. Boroviak T, Rashbass P (2011) The apical polarity determinant Crumbs 2 is a novel regulator of ESC-derived neural progenitors. Stem cells 29 (2): 193–205.

116. Chen F, Tillberg PW, Boyden ES (2015) Optical imaging. Expansion microscopy. Science (New York, N.Y.) 347 (6221): 543–548.
117. Terasaki M, Brunson JC, Sardi J (2020) Analysis of the three dimensional structure of the kidney glomerulus capillary network. Scientific reports 10 (1): 20334.
118. Chozinski TJ, Mao C, Halpern AR, Pippin JW, Shankland SJ et al. (2018) Volumetric, Nanoscale Optical Imaging of Mouse and Human Kidney via Expansion Microscopy. Scientific reports 8 (1): 10396.
119. Lorén N, Hagman J, Jonasson JK, Deschout H, Bernin D et al. (2015) Fluorescence recovery after photobleaching in material and life sciences: putting theory into practice. Quarterly reviews of biophysics 48 (3): 323–387.
120. Braeckmans K, Peeters L, Sanders NN, Smedt SC de, Demeester J (2003) Three-dimensional fluorescence recovery after photobleaching with the confocal scanning laser microscope. Biophysical journal 85 (4): 2240–2252.
121. Schindelin J, Arganda-Carreras I, Frise E, Kaynig V, Longair M et al. (2012) Fiji: an open-source platform for biological-image analysis. Nature Methods 9 (7): 676–682.
122. Fischer H, Polikarpov I, Craievich AF (2004) Average protein density is a molecular-weight-dependent function. Protein science : a publication of the Protein Society 13 (10): 2825–2828.
123. Signal P; https://services.healthtech.dtu.dk/services/SignalP-5.0/.
124. Pettersen EF, Goddard TD, Huang CC, Meng EC, Couch GS et al. (2021) UCSF ChimeraX: Structure visualization for researchers, educators, and developers. Protein science : a publication of the Protein Society 30 (1): 70–82.
125. Uhlén M, Fagerberg L, Hallström BM, Lindskog C, Oksvold P et al. (2015) Proteomics. Tissue-based map of the human proteome. Science (New York, N.Y.) 347 (6220): 1260419.
126. Alves CH, Sanz AS, Park B, Pellissier LP, Tanimoto N et al. (2013) Loss of CRB2 in the mouse retina mimics human retinitis pigmentosa due to mutations in the CRB1 gene. Human molecular genetics 22 (1): 35–50.
127. Lemmers C, Michel D, Lane-Guermonprez L, Delgrossi M-H, Médina E et al. (2004) CRB3 binds directly to Par6 and regulates the morphogenesis of the tight junctions in mammalian epithelial cells. Molecular biology of the cell 15 (3): 1324–1333.
128. Bucur O, Zhao Y (2018) Nanoscale Imaging of Kidney Glomeruli Using Expansion Pathology. Frontiers in medicine 5: 322.
129. Huber TB, Simons M, Hartleben B, Sernetz L, Schmidts M et al. (2003) Molecular basis of the functional podocin-nephrin complex: mutations in the NPHS2 gene disrupt nephrin targeting to lipid raft microdomains. Human molecular genetics 12 (24): 3397–3405.
130. Tanoue A, Katayama K, Ito Y, Joh K, Toda M et al. (2021) Podocyte-specific Crb2 knockout mice develop focal segmental glomerulosclerosis. Scientific reports 11 (1): 20556.
131. Mahesaniya A, Williamson CR, Keyvani Chahi A, Martin CE, Mitro AE et al. (2022) Sex Differences in Glomerular Protein Expression and Effects of Soy-Based Diet on Podocyte Signaling. Canadian journal of kidney health and disease 9: 20543581221121636.

132. Fletcher GC, Lucas EP, Brain R, Tournier A, Thompson BJ (2012) Positive feedback and mutual antagonism combine to polarize Crumbs in the Drosophila follicle cell epithelium. Current biology : CB 22 (12): 1116–1122.
133. Niewiadomska P, Godt D, Tepass U (1999) DE-Cadherin is required for intercellular motility during Drosophila oogenesis. The Journal of cell biology 144 (3): 533–547.
134. Chen C-L, Gajewski KM, Hamaratoglu F, Bossuyt W, Sansores-Garcia L et al. (2010) The apical-basal cell polarity determinant Crumbs regulates Hippo signaling in Drosophila. Proceedings of the National Academy of Sciences of the United States of America 107 (36): 15810–15815.
135. Röper K (2012) Anisotropy of Crumbs and aPKC drives myosin cable assembly during tube formation. Developmental cell 23 (5): 939–953.
136. Huff J (2015) The Airyscan detector from ZEISS: confocal imaging with improved signal-to-noise ratio and super-resolution. Nature Methods 12 (12): i–ii. Available: https://doi.org/10.1038/nmeth.f.388.
137. Wang CK, Ghani HA, Bundock A, Weidmann J, Harvey PJ et al. (2018) Calcium-Mediated Allostery of the EGF Fold. ACS chemical biology 13 (6): 1659–1667.
138. Yáñez M, Gil-Longo J, Campos-Toimil M (2012) Calcium binding proteins. Advances in experimental medicine and biology 740: 461–482.
139. Elíes J, Yáñez M, Pereira TMC, Gil-Longo J, MacDougall DA et al. (2020) An Update to Calcium Binding Proteins. Advances in experimental medicine and biology 1131: 183–213.
140. Pena F, Jansens A, van Zadelhoff G, Braakman I (2010) Calcium as a crucial cofactor for low density lipoprotein receptor folding in the endoplasmic reticulum. The Journal of biological chemistry 285 (12): 8656–8664.
141. Jensen SA, Handford PA (2016) New insights into the structure, assembly and biological roles of 10-12 nm connective tissue microfibrils from fibrillin-1 studies. The Biochemical journal 473 (7): 827–838.
142. Balzar M, Briaire-de Bruijn IH, Rees-Bakker HA, Prins FA, Helfrich W et al. (2001) Epidermal growth factor-like repeats mediate lateral and reciprocal interactions of Ep-CAM molecules in homophilic adhesions. Molecular and cellular biology 21 (7): 2570–2580.
143. Appella E, Robinson EA, Ullrich SJ, Stoppelli MP, Corti A et al. (1987) The receptor-binding sequence of urokinase. A biological function for the growth-factor module of proteases. The Journal of biological chemistry 262 (10): 4437–4440.
144. Artavanis-Tsakonas S, Matsuno K, Fortini ME (1995) Notch Signaling. Science 268 (5208): 225–232. Available: https://doi.org/10.1126/science.7716513.
145. Stenflo J, Stenberg Y, Muranyi A (2000) Calcium-binding EGF-like modules in coagulation proteinases: function of the calcium ion in module interactions. Biochimica et biophysica acta 1477 (1-2): 51–63.
146. Sakamoto K, Chao WS, Katsube K, Yamaguchi A (2005) Distinct roles of EGF repeats for the Notch signaling system. Experimental cell research 302 (2): 281–291.
147. Breitwieser GE (2008) Extracellular calcium as an integrator of tissue function. The international journal of biochemistry & cell biology 40 (8): 1467–1480.
148. Grahammer F, Schell C, Huber TB (2013) The podocyte slit diaphragm--from a thin grey line to a complex signalling hub. Nature reviews. Nephrology 9 (10): 587–598.

149. Inoue T, Yaoita E, Kurihara H, Shimizu F, Sakai T et al. (2001) FAT is a component of glomerular slit diaphragms. Kidney international 59 (3): 1003–1012.
150. Martin CE, Jones N (2018) Nephrin Signaling in the Podocyte: An Updated View of Signal Regulation at the Slit Diaphragm and Beyond. Frontiers in endocrinology 9: 302.
151. Graham FL, Smiley J, Russell WC, Nairn R (1977) Characteristics of a human cell line transformed by DNA from human adenovirus type 5. The Journal of general virology 36 (1): 59–74.
152. Gaush CR, Hard WL, Smith TF (1966) Characterization of an established line of canine kidney cells (MDCK). Proceedings of the Society for Experimental Biology and Medicine. Society for Experimental Biology and Medicine (New York, N.Y.) 122 (3): 931–935.
153. Shankland SJ, Pippin JW, Reiser J, Mundel P (2007) Podocytes in culture: past, present, and future. Kidney international 72 (1): 26–36.
154. Agarwal S, Sudhini YR, Reiser J, Altintas MM (2021) From Infancy to Fancy: A Glimpse into the Evolutionary Journey of Podocytes in Culture. Kidney360 2 (2): 385–397.
155. Goehring NW, Chowdhury D, Hyman AA, Grill SW (2010) FRAP analysis of membrane-associated proteins: lateral diffusion and membrane-cytoplasmic exchange. Biophysical journal 99 (8): 2443–2452.
156. Kumar M, Mommer MS, Sourjik V (2010) Mobility of cytoplasmic, membrane, and DNA-binding proteins in Escherichia coli. Biophysical journal 98 (4): 552–559.
157. Saffman PG, Delbrück M (1975) Brownian motion in biological membranes. Proceedings of the National Academy of Sciences of the United States of America 72 (8): 3111–3113.
158. Tepass U, Tanentzapf G, Ward R, Fehon R (2001) Epithelial cell polarity and cell junctions in Drosophila. Annual review of genetics 35: 747–784.
159. Schell C, Rogg M, Suhm M, Helmstädter M, Sellung D et al. (2017) The FERM protein EPB41L5 regulates actomyosin contractility and focal adhesion formation to maintain the kidney filtration barrier. Proceedings of the National Academy of Sciences of the United States of America 114 (23): E4621-E4630.
160. Maier JI, Rogg M, Helmstädter M, Sammarco A, Schilling O et al. (2021) EPB41L5 controls podocyte extracellular matrix assembly by adhesome-dependent force transmission. Cell reports 34 (12): 108883.
161. Li Y, Wei Z, Yan Y, Wan Q, Du Q et al. (2014) Structure of Crumbs tail in complex with the PALS1 PDZ-SH3-GK tandem reveals a highly specific assembly mechanism for the apical Crumbs complex. Proceedings of the National Academy of Sciences of the United States of America 111 (49): 17444–17449.
162. Hafezi Y, Bosch JA, Hariharan IK (2012) Differences in levels of the transmembrane protein Crumbs can influence cell survival at clonal boundaries. Developmental biology 368 (2): 358–369.
163. Chozinski TJ, Halpern AR, Okawa H, Kim H-J, Tremel GJ et al. (2016) Expansion microscopy with conventional antibodies and fluorescent proteins. Nature Methods 13 (6): 485–488.
164. Asano SM, Gao R, Wassie AT, Tillberg PW, Chen F et al. (2018) Expansion Microscopy: Protocols for Imaging Proteins and RNA in Cells and Tissues. Current protocols in cell biology 80 (1): e56.

165. Bürgers J, Pavlova I, Rodriguez-Gatica JE, Henneberger C, Oeller M et al. (2019) Light-sheet fluorescence expansion microscopy: fast mapping of neural circuits at super resolution. Neurophotonics 6 (1): 15005.
166. Stockhausen A, Bürgers J, Rodriguez-Gatica JE, Schweihoff J, Merkel R et al. (2020) Hard-wired lattice light-sheet microscopy for imaging of expanded samples. Optics express 28 (10): 15587–15600.
167. Bagçi H, Kohen F, Kusçuoglu U, Bayer EA, Wilchek M (1993) Monoclonal anti-biotin antibodies simulate avidin in the recognition of biotin. FEBS letters 322 (1): 47–50.
168. Beer MA de, Giepmans BNG (2020) Nanobody-Based Probes for Subcellular Protein Identification and Visualization. Frontiers in cellular neuroscience 14: 573278.
169. Pereira PM, Albrecht D, Culley S, Jacobs C, Marsh M et al. (2019) Fix Your Membrane Receptor Imaging: Actin Cytoskeleton and CD4 Membrane Organization Disruption by Chemical Fixation. Frontiers in immunology 10: 675.
170. Ichikawa T, Wang D, Miyazawa K, Miyata K, Oshima M et al. (2022) Chemical fixation creates nanoscale clusters on the cell surface by aggregating membrane proteins. Communications biology 5 (1): 487.
171. Loie E, Charrier LE, Sollier K, Masson J-Y, Laprise P (2015) CRB3A Controls the Morphology and Cohesion of Cancer Cells through Ehm2/p114RhoGEF-Dependent Signaling. Molecular and cellular biology 35 (19): 3423–3435.
172. Kubitscheck U (2013) Fluorescence microscopy. From principles to biological applications. Weinheim: Wiley-Blackwell. 410 p.

Abbreviations

°C	Degree Celsius
µg	Micro gram
µL	Microliter
µM	Micro molar
µm	Micrometer
µs	Microsecond
2-D	Two-dimensional
3-D	Three-dimensional
aa	amino acid
Actinin	α-actinin-4
AFP	alpha-fetoproteins
Ala	Alanine (A)
Amp	Ampicillin sodium salt
ANOVA	Analysis of variance
aPKC	atypical protein kinase C
APS	Ammonium persulphate
Arg	Arginine (R)
Asn	Asparagine (N)
Asp	Aspartic acid (D)
AU	Airy unit
BSA	Bovine serum albumin
C	C-terminal of protein
CANX	Calnexin
CASP	Critical Assessment of Structure Prediction
CD	Collecting duct
CD2AP	CD2-adaptor protein
cDNA	Complementary DNA
CKD	Chronic kidney disease
cm^2	Centimeter squared
CO_2	Carbon dioxide
CRB	Crumbs
CRB1	Crumbs homolog 1

CRB2	Crumbs homolog 2
CRB3	Crumbs homolog 3
Cys	Cyseine (C)
Da.	Dalton
DAG	Diacylglycerol
DLG	Discs large
Dm	*Drosophila melanogaster*
DMEM	Dulbecco's Modified Eagle's Medium
DMSO	Dimethyl sulphoxide
DNA	Deoxyribonucleic acid
Dr	*Danio rerio*
DT	Distal convoluted tubule
E. coli	*Escherichia coli*
ECDs	Extracellular domains
ECM	Extracellular matrix
EDTA	Ethylenediamine tetra acetic acid
EGF	Epidermal growth factor
eGFP	Enhanced green fluorescent protein
ER	Endoplasmic reticulum
FA	Focal adhesion
FBM	FERM-binding motif
FBS/FCS	Fetal bovine/Calf serum
FERM	4.1/Ezrin/Radixin/Moesin
Flt1	VEGFR1
Flt1/Kdr	VEGFR2
FPs	Foot processes or pedicels
FRET	Fluorescence Resonance Energy Transfer
G	Globular
g	Grams
GaAsP-PMT	Gallium arsenide phosphamide-photomultiplier tube
GBM	Glomerular basement membrane
GECs	Glomerular endothelial cells
GFB	Glomerular filtration barrier
GFR	Glomerular filtration rate
Gln	Glutamine (Q)

Glu	Glumatic acid (E)
Gly	Glycine (G)
GW	Gateway
h.	Hours
HBSS	Hanks buffered salt solution
HEK GP2 293	Human Embryonic kidney
HEPES	2-(4-(2-hydroxyethyl)-1-piperazine)-ethanesulfonic acid
Hs:	*Homo sapiens*
HSPGs	Heparin sulfate proteoglycans
Hz.	Hertz
ICD	Intracellular domain
ILK	Integrin-linked kinase
Integrin	α3β1 integrin
IP3	Inositol 1,4,5-triphosphate
JF	Janelia-Fluor HaloTag ligand
Kan	Kanamycin sulphate
KO	Knockout
L	Litres
Lam G	Laminin globular-like domains
LB	Luria/Miller broth
LCA	Lebers congenital amaurosis
Lgl	Lethal giant larvae
LOH	Loop of Henle
LUT	Look-up-table
m^2	Meter squared
MA-NHS	Methacrylic acid N-Hydroxy succimide ester
MCs	Mesangial cells
MDCK	Mardin-Darby canine kidney
mg	Milligram
min.	Minutes
MIPs	Maximum intensity projections
ml	Milliliter
mm	Millimeters
Mm	*Mus musculus*

mmHg	Millimeters of Mercury
ms	Milliseconds
n	Number of cells measured per plate replicate
N:	N-terminal of protein
N’	Number of plate replicates per cell line
NA	Numerical aperture
nm	Nanometer
O/N	Overnight
OI	Oil immersion
OM	Overlapping cell membrane duplets
Par 3	Partitioning defective 3
Par6	Partitioning defective 6
PATJ	PALS1-associated tight junction homologue
PBM	PDZ-binding motif
PBS	Phosphate buffered saline
PCR	Polymerase chain reaction
PDZ	PSD-95/Discs-large/ZO-1
PECs	Parietal epithelial cells
PLC	Phospholipase C
pLDDT	Per-residue confidence score
PM	Free plasma membrane
Pro-ExM	Protein-retention expansion microscopy
PT	Proximal tubule
Puro	Puromycin
ROBO2:	Roundabout homologue 2
ROI	Regions of interest
RP	Retinitis pigmentosa
RT	Room temperature
s	Seconds
S2	Safety-level 2
Scrib	Scribble
SD	Slit diaphragm
Sdt	Stardust
Ser	Serine (S)
SP	Signal peptide

SR	Super-resolution
SRNS	Steroid-resistant nephrotic syndrome
syn	Synaptopodin
T1	Time constant for population A1 (Tau 1)
T2	Time constant for population A2 (Tau 2)
TEMED	N,N,N′,N′-Tetramethylethylenediamine
Trp	Tryptophan (W)
TRPC	Transient receptor potential-like channel
u	Units
v/v	Volume by volume
VEGFA	Vascular Endothelial Growth Factor A
w/v	Weight by volume
WI	Water immersion
WT	Wild type
ZO-1	Zonula Occludens-1

Index of Figures

Index of Tables

Acknowledgements

I would like to sincerely thank my supervisor and mentor, Prof. Dr. Ulrich Kubitscheck, for providing me with the opportunity and freedom to work on this thesis. It has been a pure delight to work and learn under his guidance and I thank him with all my heart.

A special thanks to our collaboration partners in Münster, Prof. Dr. Thomas Weide, without whom this project would never have been possible. His knowledge on the topic of podocyte biology has been immensely helpful to bring this thesis to fruition.

I would like to thank our collaboration partners in Jülich, Prof. Dr. Rudolf Merkel, whose expertise in traction force microscopy provided us with the much needed information that helped complete the CRB2 puzzle. I would like to thank him for also being my second supervisor and for the co-presentation. I would also like to thank Prof. Dr. Arne Lützen and Prof. Dr. Oliver Gruss for participating in the examination committee.

I would like to give a super special thank you to Dr. Jan-Peter Siebrasse, who has always been there to help me with all my problems. His biological acumen and coding skills have been invaluable. With his support, I never feared trying out something new and I could always blindly rely on his experience to guide the way.

This thesis wouldn’t be possible without Dr. Annika Möller-Kerrut who was deeply involved throughout the course of this thesis. She was instrumental in establishing the podocyte cell lines expressing different CRBs constructs and performing kidney expansion. I also thank Rebecca Rixen, a master student under the supervision of Dr. Annika Möller-Kerrut, who made the ECD/ICD plasmid constructs and cell lines.

I would also like to thank Ms. Sabine Wirths for her cloning expertise and constant help throughout this thesis. A big thank you to both our workshops for their constant cooperation. I also like to thank everyone who agreed to proofread this work.

My thanks also go to the coolest office with my partners in crime, Dr. Juan Edo Rodriguez Gatica and Annika Marie Krüger. You guys have been amazing throughout this journey and I couldn’t have done it without you. I also thank the whole working group for the pleasant working atmosphere, technical discussions and the many fun times together. You’ve been like my family away from home.

Finally, I would like to thank my parents for always being there for me and for their unconditional love and support. This one’s for you!

Eidesstattliche Erklärung

Name	**Bhatia**
Vorname	**Rohan**
Titel der Dissertation	**Relevance of Crumbs homolog 2 in the Glomerular filtration barrier**

Hiermit erkläre ich durch meine Unterschrift an Eides statt:

1. Die von mir eingereichte Dissertation habe ich selbstständig und ohne unzulässige fremde Hilfe verfasst. Hierbei habe ich weder Textstellen von Dritten oder aus eigenen Prüfungsarbeiten noch Grafiken oder sonstige Materialien ohne Kennzeichnung übernommen.
2. Es sind ausschließlich die von mir angegebenen Quellen und Hilfsmittel verwendet worden.
3. Sämtliche wörtliche und nicht wörtliche Zitate aus anderen Werken sind gemäß den wissenschaftlichen Zitierregeln kenntlich gemacht.
4. Die von mir vorgelegte Arbeit ist bisher noch nicht oder an der nachstehend aufgeführten Stelle vollständig/auszugsweise veröffentlicht. (s. Anlage)
5. Die von mir vorgelegte Arbeit ist bisher noch in keiner Form als Bestandteil einer Prüfungs-/Qualifikationsleistung vorgelegt worden.
6. Ich bin nicht zweimal in einem Promotionsverfahren an einer deutschen Hochschule aufgrund einer Ablehnung der Dissertation oder nicht bestandener Prüfungsleistungen gescheitert.
7. Die von mir eingereichte Dissertation habe ich unter Beachtung der Grundsätze zur Sicherung guter wissenschaftlicher Praxis erstellt.
8. Über die Bedeutung und die strafrechtlichen Folgen einer falschen eidesstattlichen Erklärung gemäß § 156 StGB bin ich mir bewusst.
9. Meine Angaben entsprechen der Wahrheit und ich habe diese nach bestem Wissen und Gewissen gemacht.

_____ _____

Ort, Datum Unterschrift der **Doktorand**

List of publications

2024 Bhatia, R., Möller-Kerutt, A., Gerlach, S., Herfs, Y., Rixen, R., Pavenstädt, H., Hoffmann, B., Merkel, R., Kubitscheck, U., Weide, T. and Siebrasse, J.P.; Crumbs2 acts as a dynamic cellular sensor triggering stable podocyte cell-matrix anchorage. Submitted to **Science Advances, 2024.**

2021 Möller-Kerutt, A., Rodriguez-Gatica, JE., Wacker K, Bhatia, R., Siebrasse, JP., Boon, N., Van Marck, V., Boor, P., Kubitscheck, U., Wijnholds, J., Pavenstädt, H., Weide, T.; Crumbs2 Is an Essential Slit Diaphragm Protein of the Renal Filtration Barrier. **J Am Soc Nephrol. 2021** May 3;32(5):1053-1070. doi: 10.1681/ASN.2020040501. Epub 2021 Mar 9. PMID: 33687977; PMCID: PMC8259666

2021 Ruland, J.A., Krüger, A.M., Dörner, K. Bhatia, R., Wirths, S., Poetes, D., Kutay, U., Siebrasse, J.P., Kubitscheck, U; Nuclear export of the pre-60S ribosomal subunit through single nuclear pores observed in real time**. Nat Commun 12, 6211 (2021).** DOI: https://doi.org/10.1038/s41467-021-26323-7

2015 Suhag, D., Bhatia, R., Das, S., Shakeel, A., Ghosh, A., Singh, A., Sinha, O.P., Chakrabarti, S. and Mukherjee, M.; Physically cross-linked pH-responsive hydrogels with tunable formulations for controlled drug delivery; ***RSC Advances*****, 2015**, DOI: 10.1039/C5RA07424J